

Contributions to the Performance Optimization of the Monopole Four Square Array Antenna

**Von der Fakultät für Ingenieurwissenschaften der Abteilung EIT der Universität
Duisburg-Essen
zur Erlangung des akademischen Grades eines**

Doktors der Ingenieurwissenschaften (Dr.-Ing.)

genehmigte Dissertation

Von
Pedram Yazdanbakhsh

aus
Mashhad / Iran

- 1. Gutachter: Prof. Dr.-Ing. Klaus Solbach**
- 2. Gutachter: Prof. Dr.-Ing. Dirk Manteuffel**

Tag der mündlichen Prüfung: 14. Oktober 2011

Abstract

Multi-beam antennas can be used for the sectorization of 360° azimuthal coverage. One of the suitable realizations, where four monopole antennas are placed at the corners of a square, is known as the “Monopole Four-Square Array Antenna”. This thesis presents the optimization problem for this array antenna.

First, it is considered that this array is mounted on an infinite ground plane. With view to practical applications, optimization criteria are defined and a genetic algorithm is used to find the optimized values for the array variables.

Next, the “Monopole Four-Square Array Antenna” is considered to be mounted on a finite ground plane (chassis). It is seen that all performance parameters of this array are changed and deteriorated due to the excitation of chassis modes, which couple to and between the monopole antennas and which radiate and produce diffraction at the edges of the ground plane. It is found, that the performance is strongly affected by the size of each antenna, the position of each antenna on the chassis as well as the size and shape of the chassis.

A new optimization problem considering both the parameters of array and chassis dimensions is defined and the optimal values are found using the method of genetic algorithm. To model the chassis effects, in this step, the Theory of Characteristic Modes for the chassis is introduced and the effect of chassis modes on the radiation patterns and S-parameters are discussed. In order to allow the efficient use of the calculation-extensive chassis modes in our optimization, an Artificial Neural Network (ANN) is set-up to represent the effects of the chassis modes and the ANN is trained using results from an EM-field simulator. In a further step, the remaining mutual coupling between the elements of the monopole array is tackled. Using another ANN, a Decoupling and Matching Network (DMN) is designed for the “Monopole Four-Square Array Antenna” which considerably improves the radiation pattern.

The final “full-degree” optimization problem considers all parameters of the monopole array on a small chassis as well as the variables in the DMN. It is shown that by changing the values of the weighting coefficients in the optimization problem, the resulting antenna design can be matched to priorities set by practical applications.

Acknowledgments

I would like to express my special thanks to my supervisor Prof. Dr.-Ing. Klaus Solbach for his expert guidance. He has taught me to do my research in an organized and meticulous way.

I am also grateful to my second advisor Prof. Dr.-Ing. Dirk Manteuffel for his help and valuable suggestions for this thesis and doctoral defense.

The members of the HFT (Hochfrequenztechnik) group at Duisburg-Essen University have contributed immensely to my personal and professional time in Germany. The group has been a source of friendships as well as good advice and collaboration.

My parents and all my family stood behind me for which I am thankful for them forever.

Finally, I would like to thank my wife, Bahareh Elahi, for being extremely supportive and patient throughout my graduate work.

Contents

Abstract	iii
Acknowledgments	iv
List of Tables	viii
List of Figures	x
1 Introduction and Overview	1
2 Monopole Antenna and its Applications	3
2.1 Introduction.....	3
2.2 Monopole Antenna.....	3
2.2.1 Radiation Mechanism.....	4
2.2.2 Radiation Efficiency.....	5
2.2.3 Self impedance.....	8
2.3 Planar Array Antenna.....	11
2.3.1 Mutual Impedance.....	12
2.4 Monopole Four Square Array Antenna (MFSAA).....	14
2.4.1 Radiation Mechanism.....	15
2.4.2 Directivity.....	17
2.4.3 Envelope Correlation of Beams.....	18
2.4.4 Front-to-Back (F/B) ratio.....	19
2.4.5 Beam Crossover (BC) Level.....	20
2.4.6 Fitting to the ideal secant squared elevation pattern.....	21
2.4.7 Maximum Absolute Gain of the MFSAA.....	22
3 Optimization Methods and Neural Networks	24
3.1 Optimization Overview.....	24

3.1.1 Gradient-Based Optimization.....	25
3.1.2 Direct Search Method.....	25
3.1.3 Genetic Algorithm (GA).....	26
3.2 Artificial Neural Networks (ANN) for system modelling.....	31
3.2.1 How Neural Network works.....	31
3.2.2 Multilayer Perceptron (MLP).....	32
4 Performance optimization of the MFSAA	35
4.1 Optimization Problem	35
4.1.1 Minimum Envelope Correlation of Beams	35
4.1.2 Best fit to the ideal secant-squared elevation pattern	35
4.1.3 Suitable Beam Crossover Level	36
4.1.4 Maximum Front-to-Back (F/B) Ratio.....	36
4.1.5 Maximum Directivity.....	36
4.1.6 Maximum Radiation Efficiency.....	37
4.2 First order approximation model	37
4.3 Second order approximation model	39
4.4 Third order approximation model	42
5 MFSAA on a finite ground plane (Chassis)	46
5.1 Theory of Characteristic Modes (TCM).....	46
5.1.1 Mathematical formulation of characteristic modes.....	46
5.1.2 A Neural Network model to calculate the chassis mode eigenvalues.....	50
5.2 Effects of the finite ground plane (chassis).....	53
5.2.1 Single monopole antenna on a chassis	53
5.2.2 Two monopole antennas on the chassis.....	59

5.2.3 MFSAA on the chassis.....	61
5.3 Performance optimization of the MFSAA on chassis	64
5.3.1 Minimize the reflection and coupling scattering coefficients of the antennas.....	64
5.3.2 Optimum Tolerance Region.....	67
5.5.3 Realization of the MFSAA	69
5.3.4 Realization of the feed network.....	70
5.3.5 Design of a Decoupling and Matching Network (DMN)-idealized.....	75
5.3.6 Design of a DMN-realistic effects.....	77
5.3.7 Full degree optimization.....	82
5.3.7.1 Neural Network model for antenna plus DMN.....	82
5.3.7.2 Optimization Problem.....	84
5.3.7.3 Optimization Problem and symmetric radiation pattern.....	86
5.3.7.4 Optimum Tolerance Region.....	88
5.3.8 Realization of the optimized MFSAA decoupled and matched.....	90
5.3.9 Changing the weighting coefficients of the optimization problem.....	93
6 Conclusions and Future Works	95
References	97
Appendix Computation of Eigenvectors and Eigenvalues	102

List of Tables

2.1	Azimuth beam patterns (Co-Polarization) and three-dimensional patterns of the MFSAA with a uniform length of $L = 0.25\lambda$, diameter of $D = 0.006\lambda$ and different separations d (mutual coupling not considered).....	16
2.2	Front-to-back ratios of the MFSAA with different separations d , considering the radiation patterns in Table 2.1.....	19
3.1	Comparison between Standard Algorithms and Genetic Algorithm (After [25]).....	26
4.1	Values of J_2^n , ρ , D_0 , (BC) and (F/B) for the MFSAA with $d = d^{op} = 0.319\dots$	39
4.2	Optimized variables, obtained by Genetic Algorithm optimizer.....	40
4.3	Values of the MFSAA in the second order approximation model.....	42
4.4	Optimized variables obtained by Genetic Algorithm optimizer with 13 variables.....	43
4.5	Values of the MFSAA in third order approximation model.....	45
5.1	The first 3 characteristic mode resonances and their corresponding radiation quality factors for 100mm×100mm chassis.....	48
5.2	The first 3 characteristic mode resonances and their corresponding radiation quality factors for a 100mm×36mm chassis, obtained by Neural Network model.....	58
5.3	The first 3 characteristic mode resonances and their corresponding radiation quality factors for a 100mm×16mm chassis, obtained by Neural Network model.....	58
5.4	Optimized variables, obtained by optimizing the cost function (5.11) at 2.27GHz.....	65
5.5	Parameters close to the optimized values in Table 5.4 chosen to fabricate the MFSAA on a chassis.....	67
5.6	Options for choosing B_1 , B_2 and conditions to optimize the cost function (5.17).....	77
5.7	Optimized variables as well as the mutual coupling admittances of the MFSAA with DMN- idealized.....	77

5.8	Optimized variables as of the MFSAA, depicted in Fig 5.40.....	81
5.9	Reflection S-parameters for the MFSAA, depicted in Fig 5.40 for each option.....	81
5.10	Transmission S-parameters for the MFSAA, depicted in Fig 5.40 for each option.....	81
5.11	Optimized variables for the MFSAA on a chassis with integrated DMN at 2.27 GHz.....	85
5.12	Values of the antenna system using the optimized parameters in Table 5.11.....	86
5.13	Optimized variables results for the decoupled and matched MFSAA on a chassis with symmetric radiation pattern.....	87
5.14	Values of the antenna system using the optimized parameters in Table 5.13.....	88
5.15	Parameters close to the optimized values in Table 5.13 chosen to fabricate the MFSAA with DMN on a chassis.....	90
5.16	Optimized variables for the decoupled and matched MFSAA on a chassis with high value of weighting coefficient for “F/B ratio” criterion.	93
5.17	Values of the antenna system using the optimized parameters in Table 5.16.....	94

List of Figures

2.1	A monopole antenna in its simplest form, mounted on an infinite ground plane.....	4
2.2	Approximated current distribution on a thin monopole antenna of different lengths between 0.1λ and 1λ	4
2.3	Radiation intensity of a $\lambda/4$ monopole antenna on an infinite ground plane.....	5
2.4	Radiation resistance of a monopole antenna with different lengths vs. frequency.....	6
2.5	Ohmic dissipation resistance of a monopole antenna with $L = 27\text{mm}$ and different diameters vs. frequency.....	7
2.6	Radiation efficiency of a monopole antenna (a): with $D = 1\text{mm}$ and varied lengths vs. frequency, (b): with $L = 27\text{mm}$ and varied diameters vs. frequency.....	8
2.7	Self impedance of a monopole antenna with $D = 0.006\lambda$ and varied lengths.....	10
2.8	Self reactance of a monopole antenna with three different diameters and varied lengths.....	10
2.9	Planar Array geometry.....	11
2.10	Mutual impedance between two monopole antennas of a length of $L = 0.25\lambda$ and varied separation d	14
2.11	Monopole Four- Square Array Antenna, (a): layout, and (b): excitation by voltage sources.....	14
2.12	Maximum directivity of the MFSAA with a uniform length of $L=0.25\lambda$, diameter of $D = 0.006\lambda$ and different separation d	18
2.13	Envelope Correlation between two neighboring Beams of a Monopole Four- Square Array Antenna with a length of $L = 0.25\lambda$ and diameter of $D = 0.006\lambda$ as a function of d/λ	19
2.14	Two azimuth beam patterns of the MFSAA with a length of $L = 0.25\lambda$, diameter of $D = 0.006\lambda$ and separation $d = 0.271\lambda$ rotated by 90° (shifted beam) to measure the beam crossover level ($b = 2.86\text{dB}$).....	20

2.15	Beam Crossover Level for the MFSAA of a length of $L = 0.25\lambda$, diameter of $D = 0.006\lambda$ and different separation d	20
2.16	MFSAA in a base station at the fixed height h , above the ground as a transmit antenna.....	21
3.1	A cost function with local maxima of 0.2 and global maximum of 1.....	24
3.2	A cost function with many local minima and a global minimum at [0,0]...	28
3.3	Contour plot of the cost function in Fig 3.2, with (a): its local minima and maxima, (b): Initial population.....	28
3.4	The populations at iterations 65, 80, 95, and 100.....	29
3.5	The schematic of neuron and synapse (after [40]).....	31
3.6	The schematic of an artificial neural network.....	32
3.7	Multilayer Perceptron with 3 layers (after [38]).....	33
4.1	Optimization results for the first order approximation model.....	38
4.2	Azimuth radiation pattern of the first-order approximation MFSAA.....	39
4.3	Azimuth radiation pattern of second-order approximation MFSAA.....	41
4.4	Azimuth radiation pattern of third-order approximation MFSAA.....	45
5.1	Frequency dependence of the first 9 eigenvalues for a 100mm×100mm chassis, taken from [62].....	48
5.2	Surface current densities and the radiation patterns for characteristic modes of a 10cm×10cm chassis, after [63] (a): First, (b): second and (c): third chassis modes.....	49
5.3	Required 14200 data sets taken from [62, 63] to learn the neural network model.....	50
5.4	Surface of the Neural Network model to calculate the chassis modes.....	51
5.5	Different structures of the Neural Network model to calculate the chassis modes.....	51
5.6	Model accuracy comparison (average error on test data) between MLPs with different number of hidden neurons.....	52

5.7	Eigenvalues of the first (a) and second (b) modes, calculated by the neural network in comparison to the original data sets.....	53
5.8	Single monopole antenna mounted on a chassis.....	54
5.9	Differences between $S_{11}(\text{inf})$ and $S_{11}(S \text{ cm})$ in linear format. a) $S = 5\text{cm}$, b) $S = 3.6\text{cm}$, c) $S = 2.2\text{cm}$ and d) $S = 0.8\text{cm}$	55
5.10	Monopole antenna on a chassis with two coaxial ports to simulate the coupling between antenna and chassis.....	56
5.11	Transmission S-parameters between monopole antenna and $100\text{mm} \times 100\text{mm}$ chassis.....	56
5.12	Elevation radiation pattern of a monopole antenna mounted on a $100\text{mm} \times 100\text{mm}$ chassis ($\phi = 90^\circ$) at the chassis resonance frequencies for $S = 0.8\text{cm}$ and $S = 5\text{cm}$	57
5.13	Scattering reflection coefficient of a Monopole antenna mounted on a chassis ($S = 0.8$ in Fig. 5.8).....	58
5.14	Two monopole antennas mounted on a chassis.....	59
5.15	Transmission S-parameters of two monopole antennas mounted on a chassis in different positions and spaced by $d = 3\text{cm}$	60
5.16	Coupling of two monopole antennas mounted on a chassis edge ($S = 0.8 \text{ cm}$).....	60
5.17	MFSAA mounted on a chassis with phases of source voltages indicated...	61
5.18	(a): Elevation radiation pattern ($\phi = 0^\circ$), (b): elevation radiation pattern ($\phi = 90^\circ$) and (c): azimuthal radiation pattern ($\theta = 90^\circ$) at 2.27GHz of the MFSAA in Fig 5.17 with $x_2 = 10\text{cm}$ (total fields, patterns normalized to peak gain).....	62
5.19	(a): Elevation radiation pattern ($\phi = 0^\circ$), (b): elevation radiation pattern ($\phi = 90^\circ$) and (c): azimuthal radiation pattern ($\theta = 90^\circ$) at 2.27GHz of the MFSAA in Fig 5.17 with $x_1 = 10\text{cm}$ (total fields, patterns normalized to peak gain).....	62
5.20	Elevation radiation pattern ($\phi = 0^\circ$) at 2.27 GHz of the MFSAA in Fig 5.17.....	64
5.21	S-parameter S_{11} of the MFSAA mounted on a chassis, using the optimal parameters in Table 5.4.....	66

5.22	Transmission S-parameters of the MFSAA mounted on a chassis, using the optimal parameters in Table 5.4.....	66
5.23	Azimuth radiation pattern ($\theta = 90^\circ$) for the MFSAA on a chassis, using the optimal parameters in Table 5.4 and simulated at 2.27GHz.....	66
5.24	Optimum tolerance ranges of x , H , L , D and d	68
5.25	Realization of the MFSAA on a chassis using the parameters in Table 5.5.....	69
5.26	Simulated and Measured S-parameters for the MFSAA on a chassis with parameters in Table 5.5.....	69
5.27	Feed network for the MFSAA.....	70
5.28	Schematic design of Hybrid coupler in ADS simulator.....	71
5.29	Simulated S-parameters of the hybrid coupler.....	71
5.30	Realization of the feed network.....	72
5.31	Measured S_{11} (dB) and S_{21} (dB) for the network, shown in Fig 5.30.....	72
5.32	Measured transmission S-parameters (amplitude) for the matrix network, shown in Fig 5.30.....	73
5.33	Measured transmission S-parameters (degree) for the matrix network, shown in Fig. 5.30.....	73
5.34	Output ports of the network connected to the MFSAA to measure the far-field radiation pattern.....	74
5.35	Azimuth radiation pattern ($\theta = 90^\circ$) for the MFSAA, shown in Fig 5.25 at 2.27 GHz with parameters in Table 5.5. (a): measured results, (b): simulated result.....	74
5.36	DMN using a cross-coupler for the MFSAA.....	76
5.37	The cross-coupler or 0dB coupler [73].....	78
5.38	The cross-coupler in ADS simulator (schematic) optimized for $f_c = 2.27$ GHz.....	79
5.39	Simulated S-parameters of the cross-coupler, shown in Fig. 5.37.....	79
5.40	MFSAA with DMN using a cross-coupler for the MFSAA mounted on a chassis (model in EMPIRE simulator).....	80

5.41	Neural Network structure for antenna with integrated DMN.....	83
5.42	Neural network model accuracy.....	83
5.43	Azimuth radiation pattern ($\theta = 58^\circ$) of the antenna system using the optimized parameters in Table 5.11 and simulated at 2.27GHz.....	86
5.44	Azimuth radiation pattern ($\theta = 58^\circ$) of the antenna system using the optimized parameters in Table 5.15 and simulated at 2.27GHz.....	88
5.45	Optimum tolerance ranges of L, D, x, H, C_1 and C_2	89
5.46	Realization of the MFSAA with DMN using a cross-coupler, with the parameters in Table 5.15.....	90
5.47	Simulated (Empire simulator) and measured reflection coefficients S_{11}, S_{22}, S_{33} and S_{44} of the MFSAA in Fig 5.46.....	91
5.48	Simulated (Empire simulator) and measured transmission S-parameters of the MFSAA in Fig 5.46.....	91
5.49	Azimuth radiation pattern ($\theta = 90^\circ$) for the MFSAA with DMN, shown in Fig 5.46 at 2.27GHz with parameters in Table 5.15. (a): measured results, (b): simulated result.....	92
5.50	Azimuth radiation pattern ($\theta = 63^\circ$) of the antenna system using the optimized parameters in Table 5.16 and simulated at 2.27GHz.....	93
A.1	Two ground planes with different number of edge elements.....	105
A.2	Edge element.....	105
A.3	4cm×6cm chassis with 62 edge elements.....	106
A.4	Eigenvalues of the first six chassis modes of the 4cm×6cm chassis with 62 edge elements.....	107
A.5	10cm×10cm chassis with 280 edge elements.....	108
A.6	Eigenvalues of the first eight chassis modes of the 10cm×10cm chassis with 280 edge elements.....	108

CHAPTER 1 Introduction and Overview

Background

Nowadays, Phased Array antennas are becoming increasingly popular for applications that require radiation pattern control. This popularity exists because the radiation pattern of a phased array can be shaped and steered electronically by proper element excitations. The analysis and design of array antennas is complicated due to the fact that array elements are not independent of each other. Instead, the elements interact electromagnetically through what is called mutual coupling. Using a matrix network instead of phase shifters to excite the elements leads to Multi-beam antennas which can be used for the sectorization of 360° azimuthal coverage. One of the suitable realizations, where four monopole antennas are placed at the corners of a square, is known as the “Monopole Four-Square Array Antenna”. This thesis presents the optimization problem for this kind of array antenna. In order to optimize the over-all array geometry, the effects of the ground plane (chassis) have to be also considered.

Structure of the thesis

The second and third chapters of this thesis review the foundations related to the research presented in this work. The second chapter presents a review of the monopole antenna and its fundamental parameters, including radiation mechanism, radiation efficiency and self impedance, which are investigated in our optimization problem. After that, the Monopole Four Square Array Antenna (MFSAA), as a planar array antenna, is introduced and the desired fundamental parameters of this array are introduced to be utilized in the next chapters.

In chapter 3, the optimization methods and neural networks are introduced to be used in next chapters. In this way, a Genetic Algorithm (GA) method as a global optimizer is introduced and the advantageous characteristics of GA are discussed. After that, the Artificial Neural Networks (ANNs) are introduced to be used in modeling procedures in this thesis. An artificial neural network (ANN), usually called Neural Network (NN), is a mathematical model or computational model that is inspired by the structure and/or functional aspects of biological neural networks. Finally the Multilayer Perceptron (MLP) network is introduced for later application in the modeling of a finite ground plane (chassis) in chapter 5.

In chapter 4, an optimization problem for the MFSAA on an infinite ground plane is defined and an optimization procedure is performed in three different phases. In the first phase, five performance criteria, namely the minimum envelope correlation of beams, maximum front-to-back ratio, best fit to the ideal secant-squared elevation pattern, suitable beam crossover levels and maximum directivity, as introduced in chapter 2, are applied for a simple antenna model (first order approximation model). For this simple antenna model only the distance between the elements is optimized.

In the second phase, the second order approximation antenna model is defined and the efficiency of each antenna as well as the previous criteria are considered in our optimization problem. For this model, the values of element spacing, antenna length, antenna diameter and feed network source impedance are optimized using the Genetic Algorithm (GA).

Finally, for the third order approximation model, the source voltages of the feed network are also varied over a certain range and the values of source voltages as well as the variables in the previous model are optimized, using a GA. In this model, a criterion for both self impedance (to be matched to the source impedance) and mutual impedances (to be minimized) are also added to previous criteria.

In chapter 5, the finite ground plane (chassis) is introduced and the effects of using a chassis instead of an infinite ground plane for the MFSAA are discussed. As shown in [1], the ground plane can heavily influence the mutual coupling of the antenna elements placed on it, in principle due to the excitation of chassis current modes on its surface, which can lead to strong deterioration of the performance of the MFSAA.

In the first part of this chapter, the Theory of Characteristic Modes (TCM) is introduced. Characteristic modes are real current modes that can be computed numerically for conducting bodies of arbitrary shape. Since characteristic modes form a set of orthogonal functions, they can be used to expand the total current on the surface of the body [2-4]. The limitations to find the characteristic modes are discussed and a Neural Network model is designed to calculate the chassis mode eigenvalues.

The effects of a chassis on a single monopole antenna, two monopole antennas and the MFSAA are also shown in this chapter by observing variations on element patterns, reflection coefficients and mutual couplings between monopole antennas due to different chassis sizes.

Finally, the performance optimization of the MFSAA on a chassis is considered. For this purpose, the EMPIRETM (IMST GmbH, Germany) simulator is used to model the structure and to optimize the antenna and chassis parameters and the simulations are checked by comparison with experimental results. It can be seen in this step, that it is necessary to design a Decoupling and Matching Network (DMN) to compensate the mutual coupling between antennas. A design for a DMN is introduced using the ADS (Advanced Design System, Agilent Corporation, USA) network simulator and EMPIRE which leads to additional lumped elements (Capacitors/Inductors) between both adjacent and opposite antennas. Networks for both the MFSAA on an infinite ground plane and for an MFSAA on a chassis are investigated and after optimizing the cost function using a GA optimizer, the optimal value of each capacitor/inductor as well as the length and diameter of each monopole antenna and array distance are found. A verification of this last optimization step of the MFSAA on a chassis with integrated DMN is presented by an experimental MFSAA and a comparison of simulated and measured antenna patterns and S-parameters. Finally, it is shown that by changing the weighting coefficients in our cost function, the results can be matched to our priorities.

In Chapter 6, the most important conclusions of this thesis are summarized and some proposals are presented for future works.

CHAPTER 2 Monopole Antenna and its Applications

2.1 Introduction

The official IEEE definition of an antenna is given by Stutzman and Thiele [7], as: “Antenna is a part of a transmitting or receiving system that is designed to radiate or receive electromagnetic waves”. There are many different antenna types, where the Monopole antenna is one of the most common antennas used for wireless communication systems. Its popular applications in wireless systems such as broadcasting, car radios, and also more recently for cellular telephones, are mainly due to its broadband characteristics and ease of construction. Monopole antennas are commonly used in airborne and ground-based communication systems at a wide range of frequencies [8]. In this chapter, the monopole antenna and its fundamental parameters are introduced and the fundamentals of planar array antennas as well as of the Monopole Four Square Array Antenna (MFSAA) are reviewed to be utilized in next chapters. The material in this chapter relies mainly on Balanis’ textbook [9].

2.2 Monopole Antenna

A monopole antenna in its simplest form, mounted on an infinite ground plane is shown in Fig 2.1, which can be considered as one-half of the corresponding double-length centre-fed linear dipole [9]. In this figure, L is the length of the monopole antenna, V_0 is the known feed point voltage and I_0 is the known feed point current. The sinusoidal current distribution on this vertical monopole antenna is approximated as:

$$I(z) = I_m \sin k(L - z) \quad \text{for} \quad 0 \leq z \leq L \quad (2.1)$$

I_m is the maximum current, where the feed point current I_0 can also be described as:

$$I_0 = I_m \sin(kL) \quad (2.2)$$

In both equations above, k is the wave number, related to the wavelength (λ):

$$k = \frac{2\pi}{\lambda} \quad (\lambda \text{ is the wavelength}) \quad (2.3)$$

Fig 2.2 shows the approximated current distribution on a thin monopole antenna of different lengths between 0.1λ and 1λ . It can be seen from this figure, that outside the 0.5λ region, the currents are in the opposite phase in comparison to the neighboring 0.5λ region.

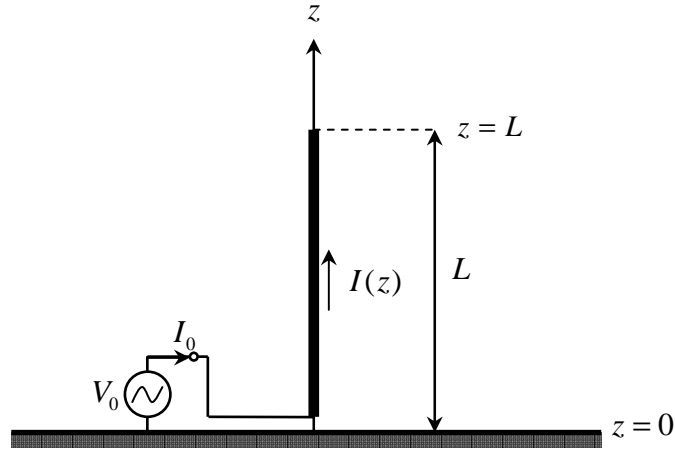


Fig. 2.1 A monopole antenna in its simplest form, mounted on an infinite ground plane

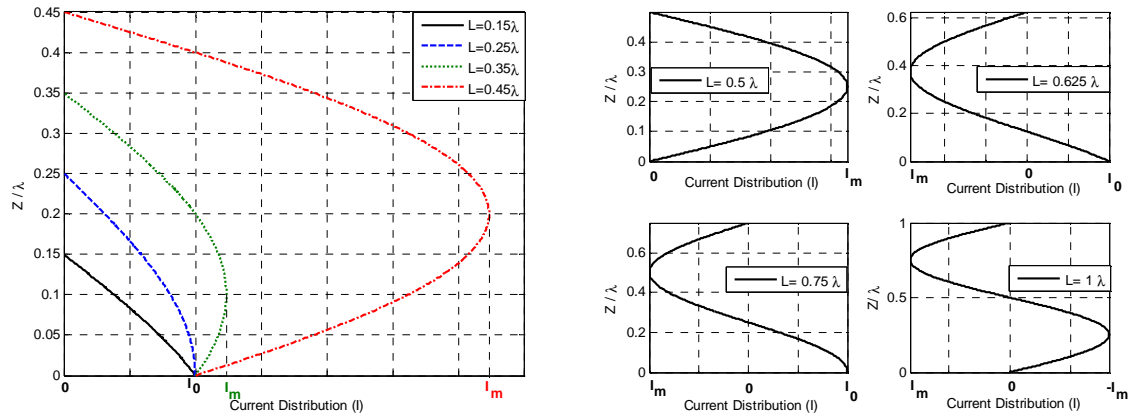


Fig. 2.2 Approximated current distribution on a thin monopole antenna of different lengths between 0.1λ and 1λ

2.2.1 Radiation Mechanism

Like a dipole antenna, a monopole antenna has an omnidirectional radiation pattern. In general, the radiation intensity of a thin monopole antenna mounted on an infinite ground plane can be approximated as the following equation:

$$F_{mon}(\theta) = c \left[\frac{\cos(kL \cos \theta) - \cos(kL)}{\sin \theta} \right]^2 \quad 0 \leq \theta \leq 90^\circ \quad (2.4)$$

In this equation, c is a constant, k is the wave number in equation (2.3) and L is the length of the monopole antenna.

The constant c can also be expressed as:

$$c = \eta_0 \frac{|I_m|^2}{8\pi^2} \quad (2.5)$$

where η_0 is the intrinsic impedance of the free space medium ($\eta_0 = 120\pi \Omega$) and I_m is the maximum current in Fig 2.1.

The radiation pattern of a thin monopole antenna with a length of 0.25λ mounted on a perfectly conducting infinite ground plane is depicted in Fig 2.3.

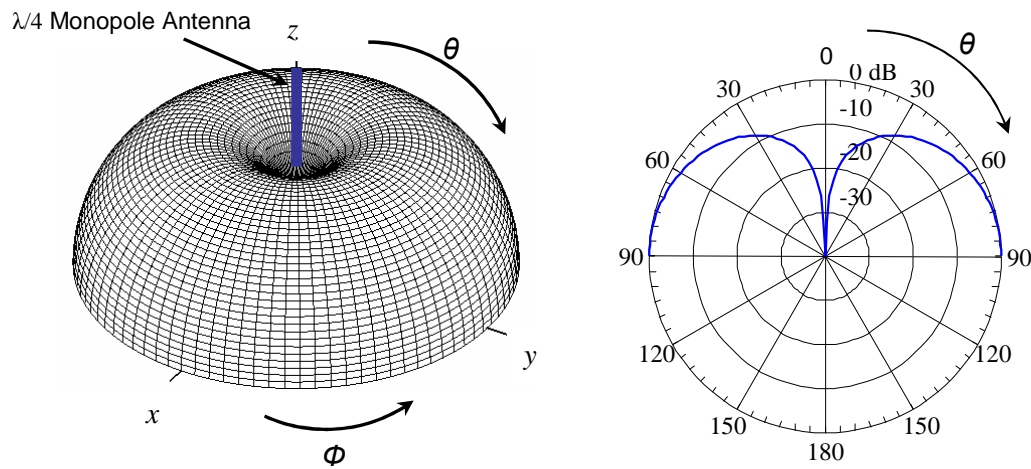


Fig. 2.3 Radiation intensity of a $\lambda/4$ monopole antenna on an infinite ground plane

As this figure shows, the maximum radiation can be seen in the horizontal direction, perpendicular to the monopole antenna ($\theta = 90^\circ$).

It can be seen from equation (2.4), that the radiation intensity of a thin monopole antenna, depends strongly on the length of it. As the length of the monopole antenna increases, the beam becomes narrower and if it increases beyond one wavelength, the number of lobes increases [9].

2.2.2 Radiation Efficiency

The Radiation efficiency η_r of a monopole antenna can be described by the following equation [9]:

$$\eta_r = \frac{P_r}{P_r + P_d} \quad (2.6)$$

where P_r and P_d are the radiated power of the antenna and the dissipated power respectively.

The radiated power P_r is given by:

$$P_r = |I_0|^2 \frac{R_r}{2} \quad (2.7)$$

where I_0 is the feed point current, shown in Fig 2.1 and R_r is the radiation resistance which can be approximated for a thin monopole antenna as [9, 10]:

$$R_r = \frac{30}{\sin^2(kL)} \int_0^\pi \frac{[\cos(kL \cos \theta) - \cos(kL)]^2}{\sin \theta} d\theta \quad \Omega \quad (2.8)$$

Fig 2.4 shows the simulated radiation resistance of a monopole antenna with four different lengths in a frequency range of 1 GHz to 10 GHz.

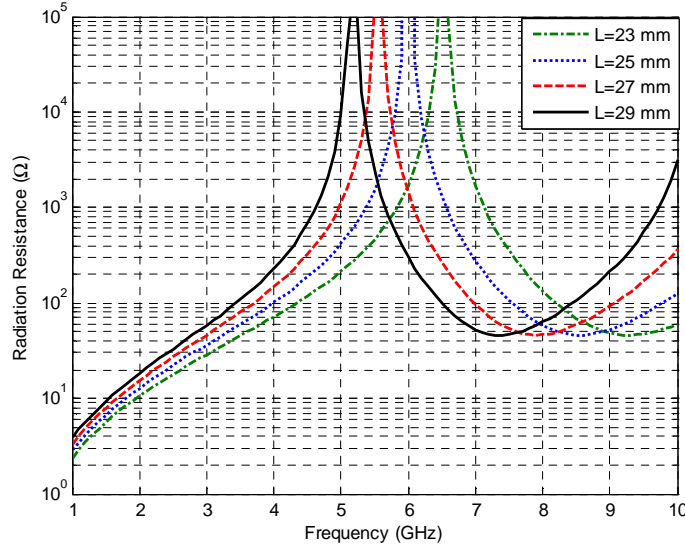


Fig. 2.4 Radiation resistance of a monopole antenna with different lengths vs. frequency

The pole in the radiation resistance refers to the half-wavelength resonance of the monopole.

It can be seen from this figure that the resonance frequency decreases by increasing the length of the monopole antenna. On the other hand, at high frequencies, the radiation resistance increases more quickly than at lower frequencies, with increasing the length of the monopole antenna.

In equation (2.6), the dissipated power P_d can also be obtained by integrating the dissipation along the monopole antenna as [10]:

$$P_d = \frac{1}{2} \int_0^L \frac{|I(z)|^2 \rho_s}{\pi D} dz = \frac{1}{2} |I_0|^2 R_d \quad (2.9)$$

where ρ_s is the sheet resistivity [8] and D is the diameter of the monopole antenna. R_d is the ohmic dissipation resistance and can be approximated:

$$R_d = \frac{\rho_s}{kD \sin^2(kL)} \left(\frac{kL}{2} - \frac{\sin(2kL)}{4} \right) \Omega \quad (2.10)$$

Fig 2.5 shows the variation of ohmic dissipation resistance for a monopole antenna with different diameters and a fixed length of $L = 27$ mm vs. frequency for $\rho_s = 1 \Omega/\text{sq}$.

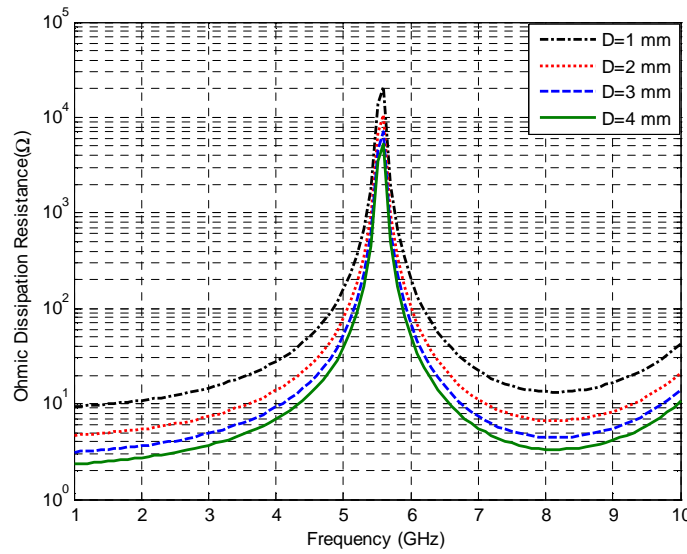


Fig. 2.5 Ohmic dissipation resistance of a monopole antenna with $L = 27$ mm and different diameters vs. frequency

From this figure, it can be easily understood that a thicker antenna has less ohmic dissipation resistance, if the length of the antenna is kept constant.

Using equations (2.7) and (2.9), the radiation efficiency of a monopole antenna in equation (2.6) can be expressed in terms of both the radiation resistance and the ohmic dissipation resistance of a monopole antenna as:

$$\eta_r = \frac{R_r}{R_r + R_d} \quad (2.11)$$

The simulated radiation efficiency of a monopole antenna with a diameter of $D = 1$ mm and varied lengths is shown in Fig 2.6 (a), where Fig 2.6 (b) shows the variation of the radiation efficiency when a monopole antenna has a fixed length of $L = 27$ mm and different diameters. An almost constant value of R_d and small value of R_r at low frequencies, result in a low efficiency at low frequencies, as can be seen in Fig 2.6 (a). As we can see from Fig 2.6 (a), for each antenna length at all frequencies below resonance frequencies, R_r increases more rapidly than R_d and this results in higher efficiency with increasing frequency.

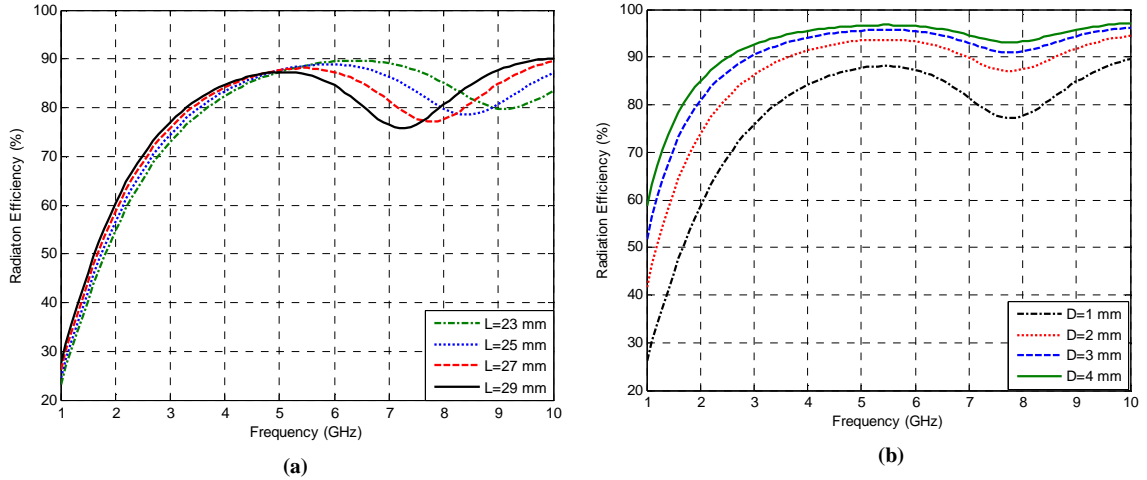


Fig. 2.6 Radiation efficiency of a monopole antenna (a): with $D=1$ mm and varied lengths vs. frequency, (b): with $L=27$ mm and varied diameters vs. frequency

On the other hand, it can be seen from Fig 2.6 (b), that by increasing the diameter of each monopole antenna, the efficiency is increased because of the reduction of R_d as seen in Fig 2.5.

Since, the radiation efficiency of a monopole antenna can be optimized by optimizing the length and diameter of antenna, the radiation efficiency of the monopole antenna is considered as one of the optimization criteria in our optimization problem in chapter 4.

2.2.3 Self Impedance

The self (input) impedance of the monopole antenna can be determined as:

$$Z_s = \frac{V_{in}}{I_{in}} \quad (2.12)$$

where V_{in} and I_{in} are the input voltage and input current of the antenna respectively. The self impedance of an antenna is an important parameter to determine the reflection coefficient of the antenna. To solve the integral equation for the current distribution, an induced EMF method [9] can be used and the self impedance of a monopole antenna can be found as a function of both the length L and diameter D of the monopole antenna (Self resistance is a function of L and self reactance is a function of both L and D).

The self resistance of a monopole antenna can be expressed as below.

$$R_s = \frac{R_m}{2 \sin^2(kL)} \quad (2.13)$$

In this equation, k is the wave number in equation (2.3) and R_m is the real part of the input impedance at the current maximum I_m (as resulting from equation (2.2)), expressed in the following equation (2.14).

$$R_m = \frac{\eta_0}{2\pi} \left\{ C + \ln(2kL) - C_i(2kL) + \frac{1}{2} \sin(2kL)[S_i(4kL) - 2S_i(2kL)] \right. \\ \left. + \frac{1}{2} \cos(2kL)[C + \ln(kL) + C_i(4kL) - 2C_i(2kL)] \right\} \quad (2.14)$$

In this equation, η_0 is the intrinsic impedance of the medium ($\eta_0 = 120\pi$), k is the wave number, C is Euler's constant ($C \approx 0.577$) and $S_i(x)$ and $C_i(x)$ are the sine and cosine integrals, explained in equations (2.15) and (2.16) respectively.

$$S_i(x) = \int_0^x \frac{\sin(\tau)}{\tau} d\tau \quad (2.15)$$

$$C_i(x) = \int_{\infty}^x \frac{\cos(\tau)}{\tau} d\tau \quad (2.16)$$

As can be seen, the self impedance of a monopole antenna is only a function of L (length of the antenna). The self reactance of a monopole antenna can also be described as:

$$X_s = \frac{X_m}{2 \sin^2(kL)} \quad (2.17)$$

where k is the wave number and X_m or the imaginary part of the input impedance at the current maximum I_m , written as:

$$X_m = \frac{\eta_0}{4\pi} \left\{ 2S_i(2kL) + \cos(2kL)[2S_i(2kL) - S_i(4kL)] \right. \\ \left. - \sin(2kL) \left[2C_i(2kL) - C_i(4kL) - C_i\left(\frac{kD^2}{4L}\right) \right] \right\} \quad (2.18)$$

In this equation, η_0 is the intrinsic impedance of medium, k is the wave number, C is Euler's constant and $S_i(x)$ and $C_i(x)$ are the sine and cosine integrals, given in equations (2.15) and (2.16). As can be seen, the self reactance of a monopole antenna can be expressed as a function of both D (Diameter of the antenna) and L (length of the antenna).

Fig 2.7 shows the self impedance of a thin monopole antenna ($D = 0.006\lambda$) with different lengths between 0 and 2λ . This figure shows that, both self resistance and self reactance become infinite for integer multiples of 0.5λ . In practice they are large.

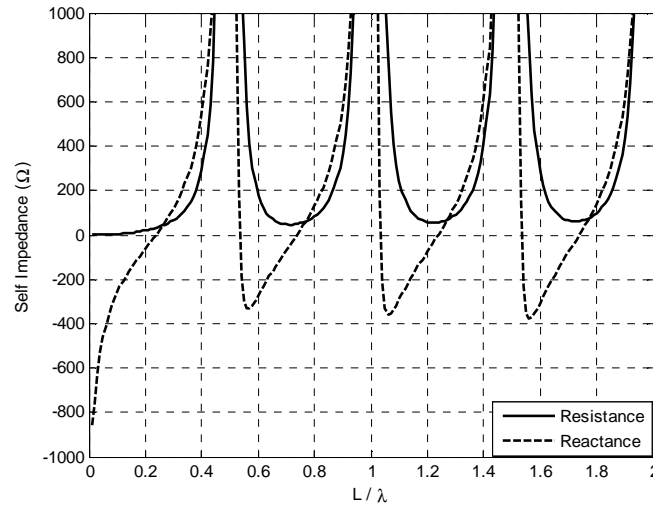


Fig. 2.7 Self impedance of a monopole antenna with $D = 0.006\lambda$ and varied lengths

For a quarter-wave monopole ($L/\lambda = 0.25$), the self impedance is half of that of a half-wave dipole: $Z_s = 36.5 + j 21.25 \Omega$. This is due to the requirement of only half the voltage to drive the monopole antenna to the same current as a dipole. Assume a dipole as having $+V_0$ and $-V_0$ applied to its end, whereas a monopole antenna only needs to apply $+V_0$ between the monopole antenna and ground plane to drive the same current (See Fig 2.1).

Ideally the diameter of the monopole antenna does not affect the input resistance, as expressed in equation (2.13). However in practice it has a small affect due to the limited range of diameter. The effect of changing the diameter of a monopole on the self reactance is shown in Fig 2.8.

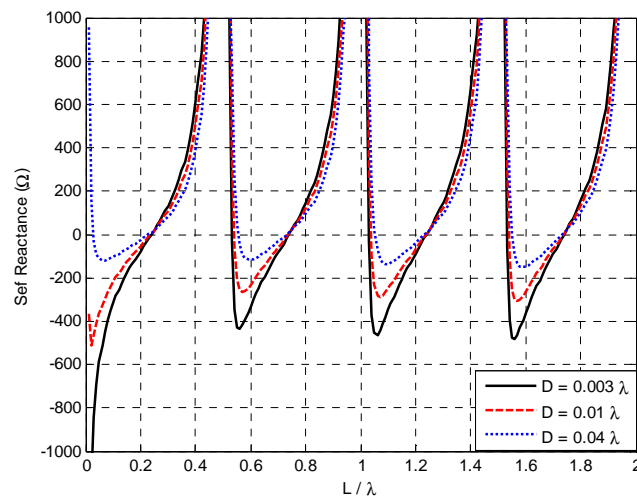


Fig. 2.8 Self reactance of a monopole antenna with three different diameters and varied lengths

It can be seen from this figure that the reactance can be reduced to zero provided the overall length is slightly less than $n\lambda/4$ ($n = 1, 3, \dots$) or slightly greater than $n\lambda/4$ ($n = 2, 4, \dots$).

This is commonly done in practice for $L \approx \lambda/4$ because the input resistance is close to 50Ω , an almost ideal match to 50Ω coaxial transmission lines. As can be seen from both Fig 2.7 and Fig 2.8 and as it has been indicated before, for a $\lambda/4$ monopole antenna with small diameter, the reactance is equal to 21.25Ω .

The self impedance of a monopole antenna is also considered as one of our optimization criteria in the next chapters.

2.3 Planar Array Antenna

Usually, the radiation pattern of a single antenna is relatively wide, with low value of gain. In many applications it is necessary to design antennas with more directive characteristics for longer distance communications. This can be achieved by utilizing an array of antennas [9]. One suitable array antenna realization is the planar (rectangular) array (Fig 2.9).

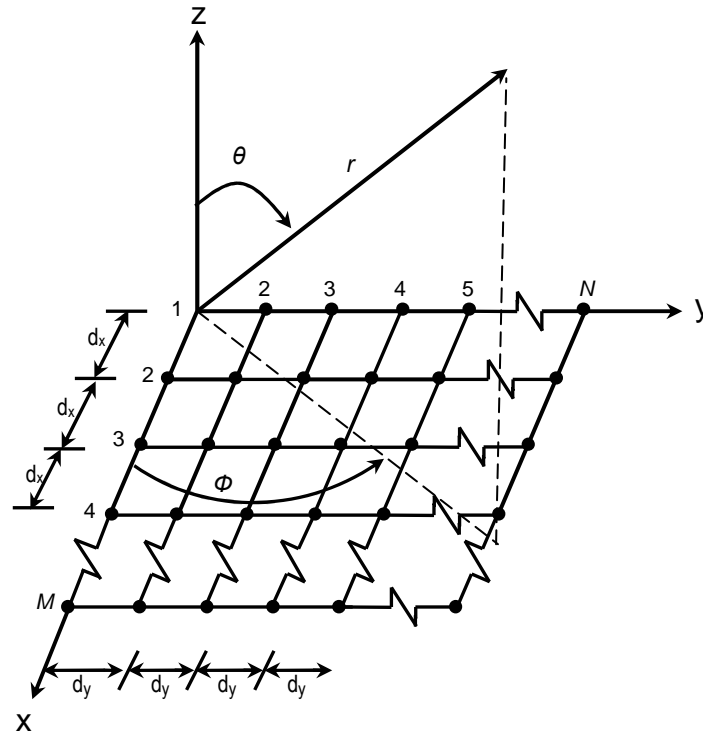


Fig. 2.9 Planar Array geometry

If $N \times M$ monopole antennas are mounted along a rectangular grid (see Fig. 2.9), the total radiation intensity can be expressed as:

$$F(\theta, \phi) = F_{\text{mon}}(\theta) |AF(\theta, \phi)|^2 \quad (2.19)$$

Where $F_{\text{mon}}(\theta)$ is the radiation intensity of a single monopole antenna, described in equation (2.4), $|AF(\theta, \phi)|$ is the array factor.

The Array Factor is a function of both the position and excitation of each antenna and can be expressed as the following equation for an array depicted in Fig 2.9 with a symmetric excitation and with its array factor maximum along θ_0, ϕ_0 :

$$AF(\theta, \phi) = 4 \sum_{m=1}^{\frac{M}{2}} \sum_{n=1}^{\frac{N}{2}} I_{mn} \cos[(2m-1)u] \cos[(2n-1)v] \quad (2.20)$$

where I_{mn} is the complex current of the $(m,n)^{\text{th}}$ monopole antenna and u and v can be described as below:

$$u = \frac{\pi d_x}{\lambda} (\sin \theta \cos \phi - \sin \theta_0 \cos \phi_0) \quad (2.21)$$

$$v = \frac{\pi d_y}{\lambda} (\sin \theta \sin \phi - \sin \theta_0 \sin \phi_0) \quad (2.22)$$

This thesis considers a planar array antenna in a special form where $M = N = 2$ and where the antenna currents are phase shifted (“phased array”).

2.3.1 Mutual Impedance

One of the most important characteristics of a planar array antenna is the mutual coupling between all antennas in this array as well as the mutual coupling between the ground plane (if the antennas are mounted on a finite ground plane) and each antenna. Note that the mutual coupling effect induces currents in antennas, thereby changing input impedance.

Considering $N \times M$ monopole antennas, mounted on an infinite ground plane in Fig 2.9, the excitations I_i ($i = 1, \dots, h = N \times M$) at the input terminals of monopole antennas can be related to the terminal voltages of the antennas (see Fig 2.1) by the impedance matrix \mathbf{Z} [9] as:

$$\mathbf{V} = \mathbf{Z}\mathbf{I} \quad (2.23)$$

where:

$$\mathbf{V} = [V_1 \dots V_h]^T \quad (2.24)$$

and:

$$\mathbf{Z} = \begin{bmatrix} Z_{11} & Z_{12} & \dots & Z_{1h} \\ Z_{21} & Z_{22} & \dots & Z_{2h} \\ \vdots & \vdots & \vdots & \vdots \\ Z_{h1} & Z_{h2} & \dots & Z_{hh} \end{bmatrix} \quad (2.25)$$

$$\mathbf{I} = [I_1 \dots I_h]^T \quad (2.26)$$

The superscript T in both equations (2.24) and (2.26) denotes the transpose of \mathbf{V} and \mathbf{I} . Through the equations (2.23) and (2.25), the terminal voltage of each element can be expressed in terms of the current flowing in all elements:

$$V_i = \sum_{j=1}^h Z_{ij} I_j \quad (i=1, \dots, h) \quad (2.27)$$

In this equation, Z_{ij} is the mutual impedance between the monopole antennas i, j and Z_{jj} is the self impedance of antenna j , described in 2.2.3.

The mutual impedance Z_{ij} between two monopole antennas with the same length L , distance d from each other and mounted on an infinite ground plane can be described based on the induced EMF method [9] as a function of L and d :

$$Z_{ij} = R_{ij} + jX_{ij} \quad (2.28)$$

where:

$$R_{ij} = \frac{R_{ij,m}}{2 \sin^2(kL)} \quad (2.29)$$

$$X_{ij} = \frac{X_{ij,m}}{2 \sin^2(kL)} \quad (2.30)$$

$R_{ij,m}$ and $X_{ij,m}$ are the real and imaginary parts of the mutual impedance at the current maximum I_m , see equation (2.2), and are expressed as:

$$R_{ij,m} = \frac{\eta_0}{4\pi} [2C_i(u_0) - C_i(u_1) - C_i(u_2)] \quad (2.31)$$

$$X_{ij} = -\frac{\eta_0}{4\pi} [2S_i(u_0) - S_i(u_1) - S_i(u_2)] \quad (2.32)$$

$$u_0 = kd \quad (2.33)$$

$$u_1 = k(\sqrt{d^2 + 4L^2} + 2L) \quad (2.34)$$

$$u_2 = k(\sqrt{d^2 + 4L^2} - 2L) \quad (2.35)$$

η_0 is the intrinsic impedance of medium ($\eta_0 = 120\pi$), $S_i(x)$ and $C_i(x)$ are the sine and cosine integrals, explained in equations (2.15) and (2.16) respectively and k is the wave number, described in equation (2.3).

Fig 2.10 shows the real and imaginary part of the mutual impedances of two side-by-side monopole antennas of a length of $L = 0.25\lambda$ and varied separation d .

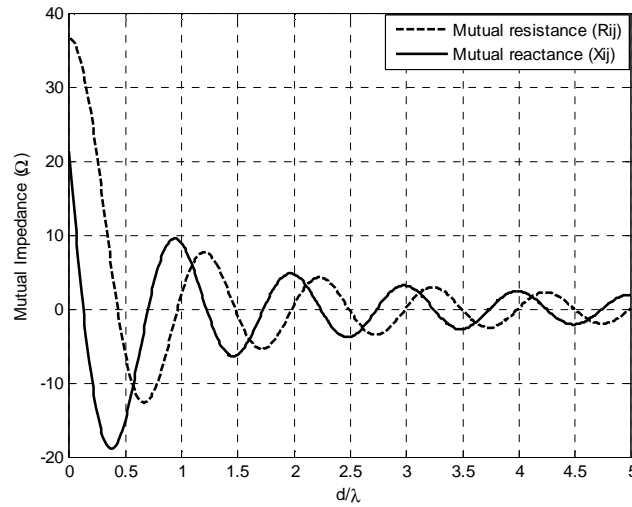


Fig. 2.10 Mutual impedance between two monopole antennas of a length of $L = 0.25\lambda$ and varied separation d

This figure shows that by increasing the distance between the antennas, the mutual coupling between them is decreased with oscillations of the impedance components. The magnitude of the mutual coupling impedance steadily reduces.

The mutual impedance between monopole antennas is also considered as one of our optimization criteria in next chapters.

2.4 Monopole Four- Square Array Antenna (MFSAA)

Considering $M = N = 2$ in Fig 2.9, one suitable array antenna can be realized based on the phased array principle, where four monopole antennas are placed at the edges of a square, in order to form four overlapping beams in azimuth and which is known as the “Monopole Four- Square Array Antenna (MFSAA)”[11]. Fig 2.11 shows the MFSAA with its excitation.

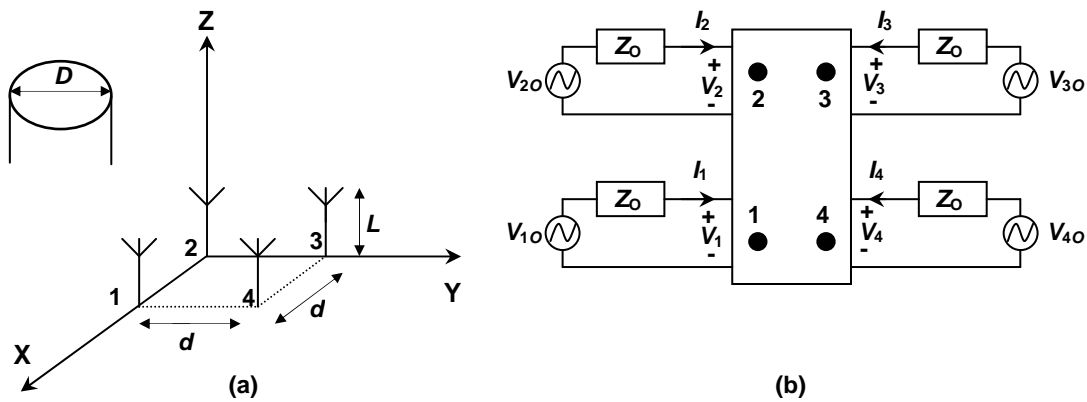


Fig. 2.11 Monopole Four- Square Array Antenna, (a): layout, and (b): excitation by voltage sources

In this figure, each monopole antenna has a length of L and a diameter of D . The distance between each neighboring antenna is d . The terminal voltage of each element is expressed as:

$$V_i = V_{i0} - I_i Z_0 \quad i = 1, \dots, 4 \quad (2.36)$$

where V_{i0} is the source open-circuit voltage of each element and Z_0 is the source impedance related to the feed network for each element. For the MFSAA, depicted in Fig 2.11, the equation (2.27) can be expressed as below ($h = 4$).

$$\begin{bmatrix} V_1 \\ V_2 \\ V_3 \\ V_4 \end{bmatrix} = \begin{bmatrix} Z_s & Z_{12} & Z_{13} & Z_{12} \\ Z_{12} & Z_s & Z_{12} & Z_{13} \\ Z_{13} & Z_{12} & Z_s & Z_{12} \\ Z_{12} & Z_{13} & Z_{12} & Z_s \end{bmatrix} \begin{bmatrix} I_1 \\ I_2 \\ I_3 \\ I_4 \end{bmatrix} \quad (2.37)$$

where Z_s is the self impedance of each antenna which can be expressed as a function of the length (L) and diameter (D) of each antenna, Z_{12} and Z_{13} are the mutual impedance between neighboring antennas and between diagonally opposite antennas respectively which can be expressed as a function of the length L and separation d .

Returning to the equations (2.36) and (2.37), the excitation of i^{th} element (phase and amplitude) can be expressed as a function of length and diameter of this element, the source voltage and source impedance of the element feed network and also of the element spacing.

2.4.1 Radiation Mechanism

As an example, radiation intensities of the MFSAA with a length of $L = 0.25\lambda$, diameter of $D = 0.006\lambda$ and varied separation d are simulated using equations (2.19), (2.36) and (2.37). The following excitation is considered for the source voltages of the first, second, third and fourth antenna respectively in Fig 2.11 (b) for a beam in $\phi = 45^\circ$ direction.

$$\begin{bmatrix} V_{10} \\ V_{20} \\ V_{30} \\ V_{40} \end{bmatrix} = \begin{bmatrix} e^{j\pi/2} \\ -1 \\ e^{j\pi/2} \\ 1 \end{bmatrix} \mathbf{V} \quad (2.38)$$

The source impedance related to the feed network for each element is assumed to be 50Ω . With the mutual coupling ignored, the beam shapes are shown for five different separations in Table 2.1. The special phased excitation as given above represents the normal operating mode as known from practical antenna systems with dedicated feed networks [11], for the generation of four equal but rotated (in ϕ -plane) patterns (multi-beam feed network). A special network for the generation of the excitation due to equation (2.38) will be presented in chapter 5.

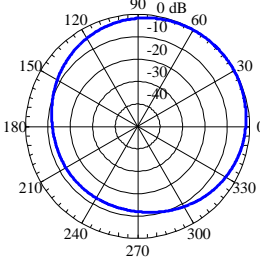
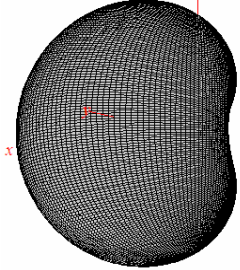
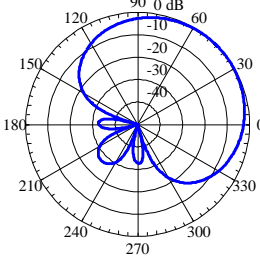
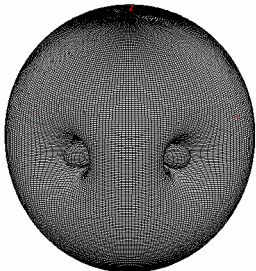
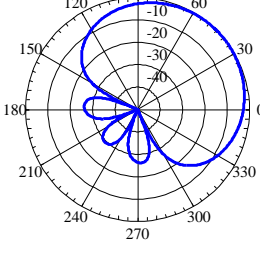
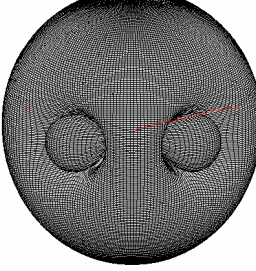
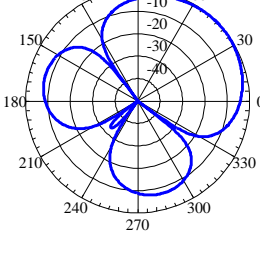
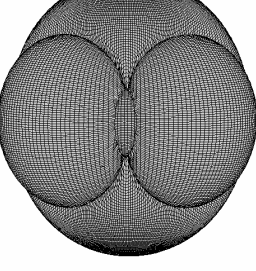
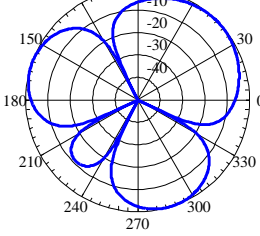
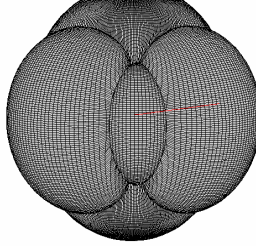
d/λ	Azimuth beam patterns ($\theta = 90^\circ$)	Three-dimensional beam patterns
0.155		
0.260		
0.271		
0.420		
0.573		

Table 2.1 Azimuth beam patterns (Co-Polarization) and three-dimensional patterns of the MFSAA with a uniform length of $L = 0.25\lambda$, diameter of $D = 0.006\lambda$ and different separations d (mutual coupling not considered)

As can be seen, by increasing the separation d , the number of side lobes as well as the amplitude of them will be increased. If the distance between the elements decreases, the beam shape converges to a nearly omni directional pattern as we expected this pattern from a single monopole antenna (see Fig 2.3).

This table shows that, to obtain a suitable and useful Radiation pattern of the MFSAA, the separation d has to be optimized, while other properties, like efficiency and impedance match require optimization of the other parameters of each monopole antenna as well, such as: length L and diameter D .

To define the suitable and useful radiation pattern, in the following, some important fundamental parameters are introduced to take into consideration, such as: directivity, envelope correlation of beams, front-to-back ratio, fitting to the ideal secant squared elevation pattern and beam crossover level. Note that so far the MFSAA is considered on an infinite ground plane.

2.4.2 Directivity

The Directivity D of an array antenna can be defined as the ratio of the radiation intensity in a given direction from the array to the average radiation intensity [9] and can be expressed as:

$$D(\theta, \phi) = 4\pi \frac{F(\theta, \phi)}{\int_0^{2\pi} \int_0^{\pi} F(\theta, \phi) \sin \theta d\theta d\phi} \quad (2.39)$$

where $F(\theta, \phi)$ is the total radiation intensity in equation (2.19). The maximum value of (2.37) or the maximum directivity D_0 is given by:

$$D_0 = 4\pi \frac{F(\theta, \phi)|_{\max}}{\int_0^{2\pi} \int_0^{\pi} F(\theta, \phi) \sin \theta d\theta d\phi} \quad (2.40)$$

The maximum directivity of the MFSAA with a uniform length of $L = 0.25\lambda$, diameter of $D = 0.006\lambda$, source voltages expressed in equation (2.38), source impedance of 50Ω and different separations d , is shown in Fig 2.12. D_0 is calculated using equation (2.40) for $0 \leq \theta \leq \pi/2$ and $0 \leq \phi \leq 2\pi$ (half space over infinite ground plane).

This figure shows that by changing the separation d , the maximum directivity of the MFSAA is changed dramatically.

For this MFSAA, the maximum value of D_0 can be seen both in the separations $d = 0.35\lambda$ and $d = 0.79\lambda$ ($D_{0,\max} = 7.84\text{dB}$), where the latter separation yields a pattern with more than one main beam.

Since in many cases, the antenna design requires the optimization of the directivity of the patterns [12-14], the maximum directivity of the MFSAA is defined as one of our optimization goals, which is considered in the optimization problem.

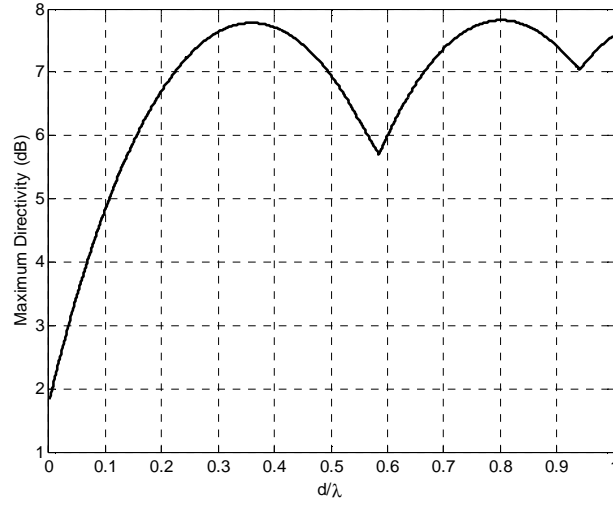


Fig. 2.12 Maximum directivity of the MFSAA with a uniform length of $L = 0.25\lambda$, diameter of $D = 0.006\lambda$ and different separation d

2.4.3 Envelope Correlation of Beams

In order to consider the diversity performance of an MFSAA, e.g., in a multi-beam configuration, which is useful for enhancing signal reception, i.e. in mobile communication systems, the envelope correlation of two different beams of this array can be derived. Following [15], the envelope correlation between two radiation patterns F_1 and F_2 is given by:

$$|\rho|^2 = \frac{\left| \oint_{\Omega} F_2 \cdot F_1^* d\Omega \right|^2}{\left(\oint_{\Omega} |F_1|^2 d\Omega \right) \left(\oint_{\Omega} |F_2|^2 d\Omega \right)} \quad (2.41)$$

where Ω is the Beam Solid Angle [9].

Fig 2.13 shows the variation of the envelope correlation of two neighboring beams of the MFSAA with source voltages expressed in equation (2.38), source impedance of 50Ω and with $\Delta\phi = 90^\circ$ difference between the maximum directions of beams. Each antenna has a length of $L = 0.25\lambda$ and diameter of $D = 0.006\lambda$ with varied separations d . This figure shows the distance between the monopole antennas is very critical for the envelope correlation. Since diversity performance depends strongly on the envelope correlation of the antenna beam patterns (e.g. [16, 17]), the envelope correlation of the MFSAA is also considered as one of our optimization criterion in the next chapters.

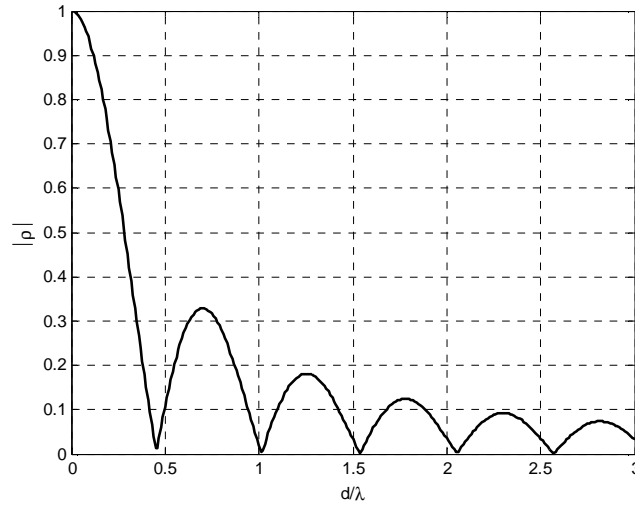


Fig. 2.13 Envelope Correlation between two neighboring Beams of a Monopole Four- Square Array Antenna with a length of $L = 0.25\lambda$ and diameter of $D = 0.006\lambda$ as a function of separation d

2.4.4 Front-to-Back (F/B) ratio

Front-to-Back (F/B) ratio is the ratio of the maximum directivity of an antenna over the maximum directivity of the side lobes in the backward direction (worst-case front-to-back ratio). The other definition of the (F/B) ratio or 180-degree (F/B) ratio is defined as the difference in directivity between the maximum forward gain bearing and another bearing 180 degrees opposite. Considering the azimuth beam patterns of the MFSAA in Table 2.1, the values of both worst-case (F/B) ratio and 180-degree (F/B) ratio is indicated in Table 2.2.

d/λ	0.155	0.260	0.271	0.420	0.573
180-degree (F/B) ratio (dB)	12.5	26.2	30.4	34.8	11.8
Worst-case (F/B) ratio (dB)	12.5	26.2	26.5	8.1	0.2

Table 2.2 Front-to-back ratios of the MFSAA with different separations d , considering the radiation patterns in Table 2.1

Note that, the worst-case (F/B) ratio is considered as a definition of the (F/B) ratio in the following.

(F/B) ratio improvement has been considered in many antenna designs using different methods such as the methods in [18-20]. Due to its importance for the operation of a multi-beam antenna system, the (F/B) ratio of the MFSAA is considered as one additional optimization criterion in the next chapters.

2.4.5 Beam Crossover (BC) level

In applications of the MFSAA as a switched beam antenna or as a multi-beam antenna, coverage of the full 360° azimuth range is limited by the beamwidth of each of the four beams.

Lowest gain is found for the directions where two neighboring beams cross-over.

A suitable beam crossover (BC) level is therefore important [21]. Two adjacent beams can intersect each other in the direction of (θ_B, ϕ_B) and at a (BC) level of b dB. Fig 2.14 shows two azimuth beam patterns of the MFSAA with the source voltages in equation (2.38) and the source impedance of 50Ω . Each antenna has a length of $L = 0.25\lambda$ and diameter of $D = 0.006\lambda$. The antenna separation of d is equal to 0.271λ .

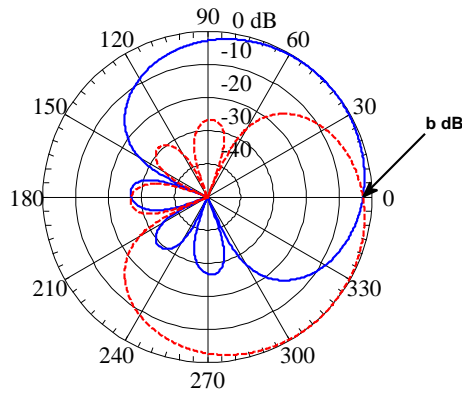


Fig. 2.14 Two azimuth beam patterns of the MFSAA with a length of $L = 0.25\lambda$, diameter of $D = 0.006\lambda$ and separation $d = 0.271\lambda$ rotated by 90° (shifted beam) to measure the beam crossover level ($b = 2.86$ dB)

In this case, the beam crossover level can be determined by measuring the level of b (the intersection point between the beam and the rotated beam).

The (BC) values for the MFSAA with a length of $L = 0.25\lambda$ and diameter of $D = 0.006\lambda$ are shown in Fig 2.15 as a function of d/λ .

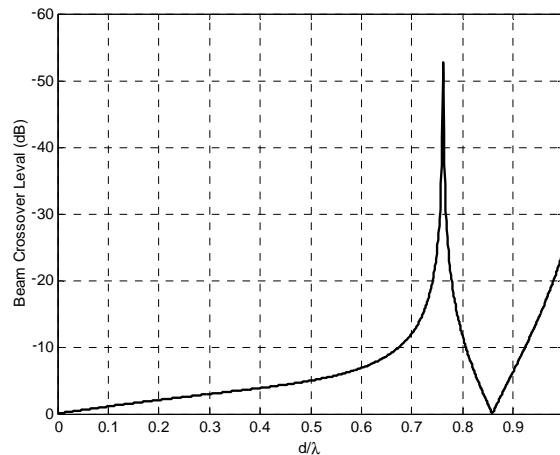


Fig. 2.15 Beam Crossover Level for the MFSAA of a length of $L = 0.25\lambda$, diameter of $D = 0.006\lambda$ and different separation d

The useful range of (BC) level in practical systems is between -3dB and -6dB. Therefore, a reasonable (BC) is also one of the goals of designing the MFSAA in this thesis and is also considered as one of the optimization criteria in the next chapters.

2.4.6 Fitting to the ideal secant squared elevation pattern

The ‘‘Friis’’ transmission equation expresses the power received to the power transmitted between two antennas [9]:

$$\frac{P_r}{P_t} = \frac{G_t G_r \lambda^2}{(4\pi R^2)} \quad (2.42)$$

where P_r and P_t are the received and transmit power respectively and G_r and G_t are the receive and transmit antenna gain (referred to a lossless isotropic source), expressed as:

$$G_t(\theta, \phi) = k_t D_t(\theta, \phi) \quad (2.43)$$

$$G_r(\theta, \phi) = k_r D_r(\theta, \phi) \quad (2.44)$$

k_t and k_r are also the transmit and receive efficiency factors respectively ($0 \leq k_t, k_r \leq 1$) [22] and the transmit and receive antennas are separated by the distance R .

If we use the MFSAA, i.e., in a base station, see Fig 2.16, at the fixed height h , above the ground elevation, elevation angle θ is related to h and R by:

$$h = R \cos \theta \quad (2.45)$$

Then the power received by the receiving antenna can be made to be independent of the distance R , by choosing the gain function $G_t(\theta, \phi)$ appropriately.

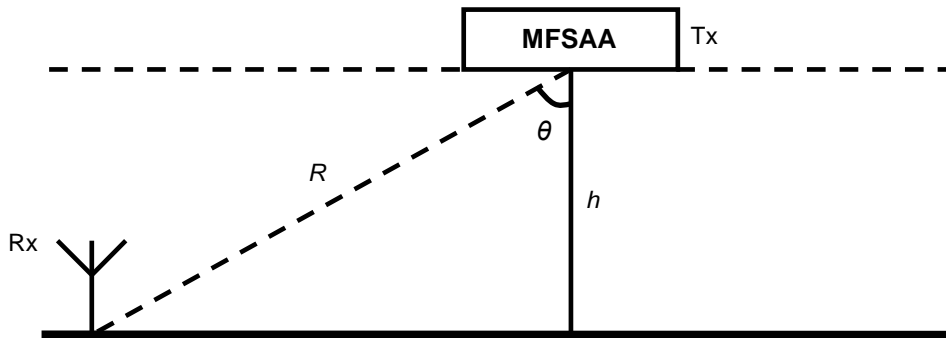


Fig. 2.16 MFSAA in a base station at the fixed height h , above the ground as a transmit antenna

If the transmit antenna gain function is designed to have the secant-squared shape $G_t(\theta, \phi) = k_c / \cos^2\theta$, then the equation (2.42) will become range independent if k_c is chosen as a constant:

$$k_c = \frac{(4\pi h)^2}{G_r(\theta, \phi)\lambda^2} \quad (2.46)$$

This assumes that the receiving antenna gain is isotropic ($G_r = 1$), which may be true approximately for small mobile terminals.

In the next chapters this method will be used to design the MFSAA to optimally match the directivity to the secant squared shape, i.e., fitting to the ideal secant squared elevation pattern will also be considered as one of our optimization criteria in next chapters.

2.4.7 Maximum Absolute Gain of the MFSAA

One reason for employing an array antenna is to provide increased gain. By the conventional definition, e.g. [9], antenna gain is degraded by internal losses only, which is reflected by the radiation efficiency. However, a practical definition of gain may also include the mismatch loss (or return loss) which shifts the reference power from the accepted power at the antenna terminals (conventional definition) to the incident (or available) power. In our case for the MFSAA, the antenna gain (the maximum absolute gain) G_{0abs} can be defined as [9]:

$$G_{0abs} = \eta_r \eta_M D_0 \quad (2.47)$$

where η_r is the radiation efficiency of the MFSAA with uniform length L and diameter D for each antenna in equation (2.11), D_0 is the maximum directivity of the MFSAA in equation (2.40) and η_M is the mismatch efficiency of the MFSAA, expressed as:

$$\eta_M = \frac{\sum_{i=1}^4 1 - |\Gamma_i|^2}{4} \quad (2.48)$$

In this equation, Γ_i is the (“active”) reflection coefficient of each antenna in the array with all other elements active and can be written as:

$$\Gamma_i = \frac{Z_i - Z_0}{Z_i + Z_0} \quad (2.49)$$

In equation (2.49), $Z_i = V_i / I_i$ is the impedance of each antenna, as calculated using e.g. equation (2.37), in combination with equations for the sources.

In the next chapters, the gain and the mismatch efficiency of the MFSAA will be calculated after each optimization procedure to show the performance of the optimized MFSAA.

CHAPTER 3 Optimization Methods and Neural Networks

3.1 Optimization Overview

Optimization is the mathematical discipline which is concerned with finding the maxima or minima of a cost function or functional $f: R^n \rightarrow R$, possibly subject to constraints or conditions g and h , where g and h as well as the optimization problem can be described as [23-25]:

$$\min f(x) \text{ subject to } g(x) = 0 \text{ and } h(x) \leq 0 \text{ where } \mathbf{x} = [x_1, x_2, \dots, x_n]$$

The goal of optimization is to minimize/maximize the cost function f to obtain the optimal values of parameters. It is also sufficient to consider only minimization, since maximum of f is the minimum of $-f$.

If we consider set $\mathbf{S} \subseteq \mathbf{R}^n$, it can be possible to find $\mathbf{x}^* \in \mathbf{S}$ such that $f(\mathbf{x}^*) \leq f(\mathbf{x})$ for all $\mathbf{x} \in \mathbf{S}$. Then \mathbf{x}^* is the optimal value of parameters \mathbf{x} .

Note that the maxima and minima of a cost function can either be “global” (the highest or lowest value over the whole region of interest) or “local” (the highest or lowest value over some small neighborhoods). Fig 3.1 shows a cost function with a global maximum of 1 and local maxima of 0.2.

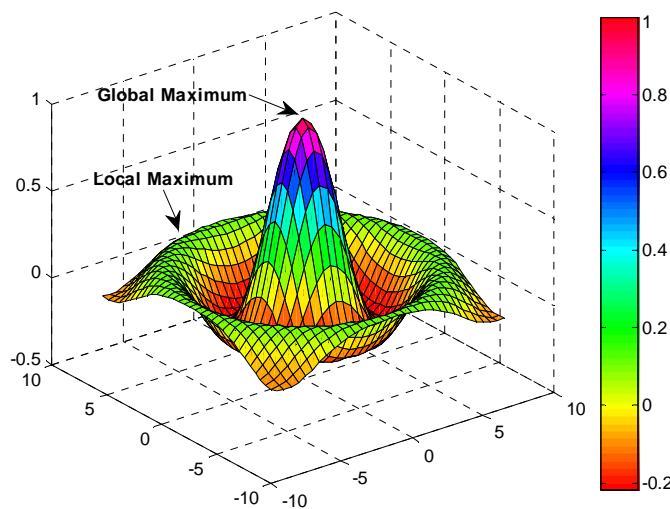


Fig. 3.1 A cost function with local maxima of 0.2 and global maximum of 1

It is usually most interesting to find the global optimum (such as the model parameters which give the best match to some image data) instead of local optimum, but this can be very difficult. In this chapter only two popular local optimization methods among too many methods [23] and the Genetic Algorithm (GA) method as a global optimization technique will be introduced and the application of this global optimizer will be discussed.

3.1.1 Gradient-Based Optimization

This method finds the critical point (or stationary point) between all $\mathbf{x} \in \mathbf{S}$ for a cost function f of n variables, i.e. the solution of the nonlinear system [23,25]:

$$\nabla f = 0 \quad (3.1)$$

where ∇f is the gradient vector of f , whose i^{th} component is $\partial f(x)/\partial x_i$.

In Gradient-Based methods it is useful to choose a starting point that minimizes the process time. Starting from initial guess x_0 , the successive approximate solutions can be found as:

$$x_{k+1} = x_k - \alpha_k \nabla f(x_k) \quad (3.2)$$

where α_k denotes the step width and is chosen depending on the used optimization. The performance of a gradient based method strongly depends on the initial values supplied. Several local optimization results can be found using different initial values. This method can be used for optimizing simple cost functions, which including only a few parameters.

3.1.2 Direct Search Method

Direct search [26, 27] is a method for solving optimization problems that do not require any information about the gradient of the cost function. The direct search algorithm searches a set of points around the initial point, looking for one where the value of the cost function is lower than the value at the initial point. After finding the new points, these points will be replaced by the previous (initial) points and this algorithm will be repeated until no further improvements are achieved. The special class of direct search algorithms called pattern search algorithm computes a sequence of points that get closer to the optimal point, as below [25]:

- 1) At each step, the algorithm searches a set of points, called a mesh, around the initial point.
- 2) The algorithm forms the mesh by adding the new point to a scalar multiple of a fixed set of vectors called a pattern.
- 3) If the algorithm finds a point in the mesh that improves the cost function at this point, the new point becomes the previous point at the next step of the algorithm.

This method is also a local optimization method and the accuracy of the results depends on the initial values.

3.1.3 Genetic Algorithm (GA)

The genetic algorithm [28] is a method for solving optimization problems that is based on natural selection, the process that drives biological evolution. The genetic algorithm repeatedly modifies a population of individual solutions.

At each step, the genetic algorithm selects individuals at random from the initial population to be parents and uses them to produce the children for the next generation. Over successive generations, the population evolves toward an optimal solution.

The genetic algorithm differs from a standard optimization algorithm in two main ways, as can be seen in table 3.1 [25].

Standard Algorithm	Genetic Algorithm
Generates a single point at each iteration and the sequence of points approaches an optimal solution	Generates a population of points at each iteration and the population approaches an optimal solution
Selects the next point in the sequence by a deterministic computation	Selects the next population by computations that involve random choices

Table 3.1 Comparison between Standard Algorithms and Genetic Algorithm [25]

The following parameters are the fundamental parameters in Genetic Algorithm method and have to be defined before describing this method [25, 29, 30]:

- **Fitness Function:** The fitness function is the cost function we want to minimize / maximize it.
- **Individuals:** An individual is any possible solution which can be considered for the fitness function.
- **Population:** Population is a group of individuals.
- **Generations:** At each iteration, GA performs a series of computations on the current population to produce a new population. Each successive population is called a new generation.
- **Diversity:** Diversity refers to the average distance between individuals in a population. A population has high diversity if the average distance is large; otherwise it has low diversity. Diversity is essential to the genetic algorithm because it enables the algorithm to search a larger region of the space.
- **Fitness Values:** The fitness value of an individual is the value of the fitness function for that individual. Since GA finds the minimum of the fitness function, the best fitness value for a population is the smallest fitness value for any individual in the population.

• **Parents and Children:** To create the next generation, GA selects certain individuals in the current population, called parents and uses them to create individuals in the next generation, called children. Typically, the algorithm tries to select parents that have better fitness values.

The following steps show how GA works:

- a) GA begins by creating a random initial population.
- b) GA creates a sequence of new populations, or generations using the individuals in the current generation to create the next generation. To create the new generation, the algorithm performs the following steps [25, 29, 30]:
 - 1) Scores each member of the current population by computing its fitness value
 - 2) Scales the raw fitness scores to convert them into a more usable range of values
 - 3) Selects parents based on their fitness
 - 4) Produces children from the parents. Children are produced either by making random changes to a single parent – mutation – or by combining the vector entries of a pair of parents – crossover
 - 5) Replaces the current population with the children to form the next generation
- c) GA stops when one of the stopping criteria is met.

As an example, Fig 3.2 shows a plot of the following cost function including two independent variables x_1 and x_2 [25, 30] :

$$Cost = 20 + x_1^2 + x_2^2 - 10(\cos 2\pi x_1 + \cos 2\pi x_2) \quad (3.3)$$

As can be seen from Fig 3.2, this cost function has many local minima. However, the cost function has just one global minimum, which occurs at the point $[0, 0]$ in the x_1 - x_2 plane, where the value of the cost function is 0. At any local minimum other than $[0, 0]$, the value of the cost function is greater than 0.

This function is often used to test the genetic algorithm optimizer, because of its many local minima. The contour plot of this function in Fig 3.3 shows the alternating maxima and minima. The algorithm begins by creating a random initial population, as shown in Fig 3.3 (b). In this example, the initial population contains 20 individuals, which is the default value of *Population size* in the *Population* options in MATLAB.

Note that all the individuals in the initial population lie in the upper-right quadrant of the picture, that is, their coordinates lie between 0 and 1, because the default value of *Initial range* in the *Population* options is defined at the point of [0 , 1] in MATLAB.

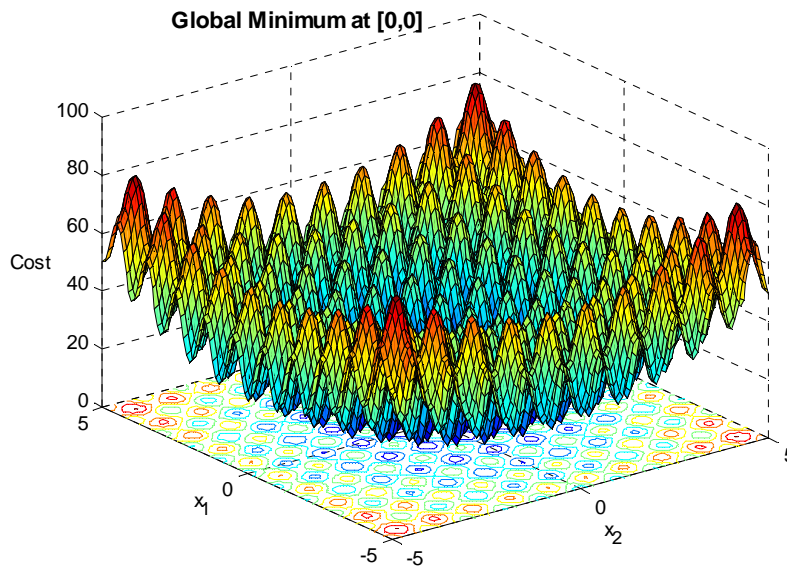


Fig. 3.2 A cost function with many local minima and a global minimum at [0 , 0]

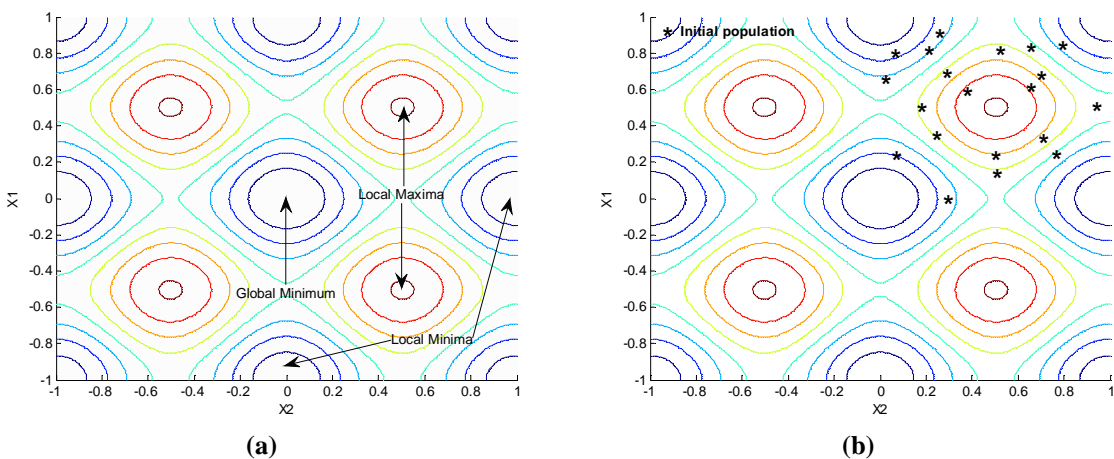


Fig. 3.3 Contour plot of the cost function in Fig 3.2, with (a): its local minima and maxima, (b): Initial population

At each step, the genetic algorithm uses the current population to create the children that make up the next generation. The algorithm selects *parents*, who contribute their *genes* (the entries of their vectors) to their children. The algorithm usually selects individuals that have better fitness values as parents. The genetic algorithm creates the following three types of children for the next generation [25, 30]:

- **Elite children:** The children (individuals) in the current generation with the best fitness values. These individuals automatically survive to the next generation.
- **Crossover children:** The children created by combining the vectors of a pair of parents. The algorithm creates crossover children by combining pairs of parents in the current population. At each coordinate of the child vector, the default crossover function randomly selects an entry, or *gene*, at the same coordinate from one of the two parents and assigns it to the child.
- **Mutation children:** created by introducing random changes, or mutations, to a single parent. The algorithm creates mutation children by randomly changing the genes of individual parents. By default, the algorithm adds a random vector from a Gaussian distribution to the parent.

Fig 3.4 shows the populations at iterations 65, 80, 95, and 100, where at iteration 100 the global minimum has been found by the GA optimizer.

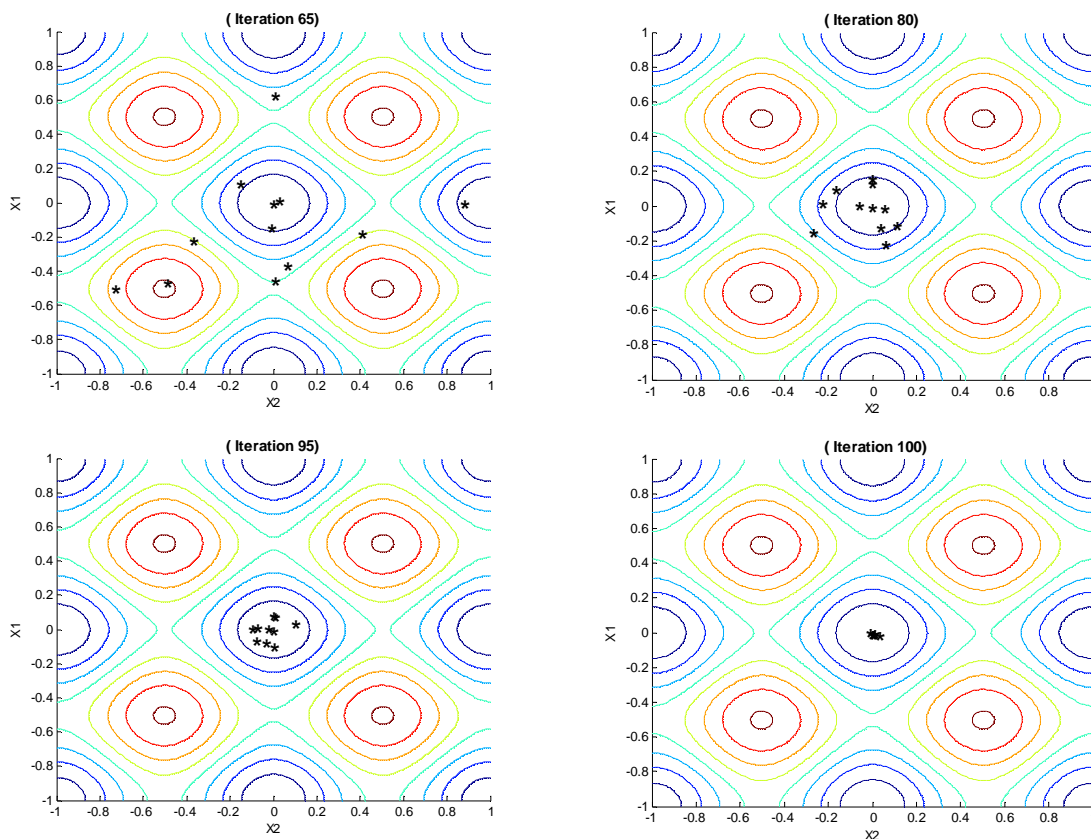


Fig. 3.4 The populations at iterations 65, 80, 95, and 100

Finally, the genetic algorithm uses the following five conditions to determine when to stop [25]:

- 1) Generations: The algorithm stops when the number of generations reaches the value of Generations
- 2) Time limit: The algorithm stops after running for an amount of time in seconds equal to Time limit
- 3) Fitness limit: The algorithm stops when the value of the fitness function for the best point in the current population is less than or equal to Fitness limit
- 4) Stall generations: The algorithm stops if there is no improvement in the objective function for a sequence of consecutive generations of length Stall generations
- 5) Stall time limit: The algorithm stops if there is no improvement in the objective function during an interval of time in seconds equal to stall time limit

The use of Genetic Algorithm in the design of antennas has become increasingly popular in recent years to reduce the difficulties in antenna synthesis. As examples, Lee et al [31] used GA in array antenna design optimization, Michielsson et al. [32] applied GA's to the synthesis of multilayered broad-band absorbers, Haupt [33, 34], used GA's to thin dense arrays of active elements for minimizing side lobe levels and Marcano et al [35] determined phase and amplitude settings for array beamforming with GA's.

In wire antenna design, Boag et al [36] designed electrically loaded wire antennas with GA's, and Linden et al [37] have used GA's to design arbitrarily shaped antennas that are circularly polarized.

In this thesis the method of Genetic Algorithm will be used in the optimization procedures to find the global minima of several complicated cost functions.

3.2 Artificial Neural Networks (ANN) for system modelling

A Neural Network or Artificial Neural Network (ANN) is an information processing paradigm that is inspired by the way biological nervous systems, such as the brain, process information [38]. In an ANN, a large number of processing elements (neurons) are working to solve specific problems by modeling the general input/output relationships. ANNs, like people, learn by example and after learning ANNs can be used to find the outputs for a set of inputs, which have not been used in the learning procedure. ANNs can be used for many complex tasks such as control engineering, telecommunications, biomedical and also Antenna design. The following abilities can be offered using ANNs [39]:

- **Adaptive learning:** An ability to learn how to do tasks based on the data given for training or initial experience.
- **Self-Organization:** An ANN can create its own organization or representation of the information it receives during learning time.
- **Real Time Operation:** ANN computations may be carried out in parallel, and special hardware devices are being designed and manufactured which take advantage of this capability.
- **Fault Tolerance via Redundant Information Coding:** Partial destruction of a network leads to the corresponding degradation of performance. However, some network capabilities may be retained even with major network damage.

3.2.1 How Neural Network works

In the human brain, a typical neuron collects signals from others through a host of fine structures called *dendrites*. The neuron sends out spikes of electrical activity through a long, thin strand known as an *axon*, which splits into thousands of branches. At the end of each branch, a structure called a *synapse* converts the activity from the axon into electrical effects [40]. See Fig 3.5.

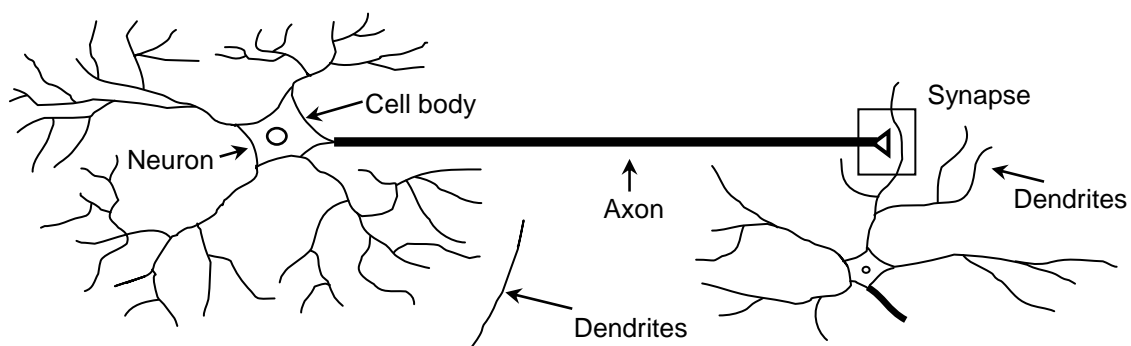


Fig. 3.5 The schematic of neuron and synapse (after [40])

Neurons combine the input signals from these connections or synapses to determine if and when it will transmit a signal to the other neurons through the connecting dendrites and synapses. The synapses modulate the input signals before they are combined, and the system is trained by changing the modulation at each synapse.

Now, the ANN can be modeled based on the training procedure of the human brain. Fig 3.6 shows the schematic of an artificial neural network, which consists of a set of inputs including n variables, m output data, input weighting coefficients and a neuron network.

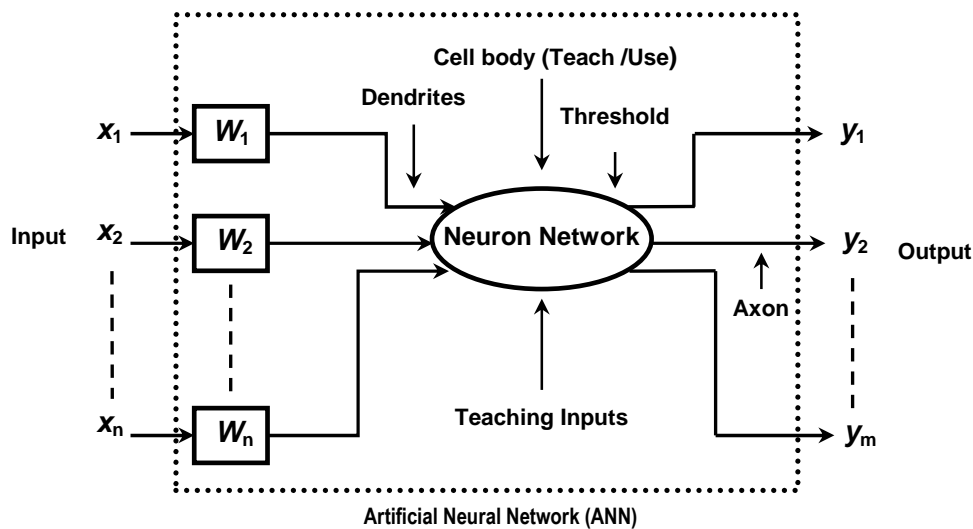


Fig. 3.6 The schematic of an artificial neural network

Neuron Network above, consists of the receptor, adder (to add $W_i x_i$ signals, $i = 1, \dots, n$) and activation function to find adaptive rules between input and output data sets.

As can be seen from this figure, an artificial neural network can be considered as a black box, which has several inputs and outputs. A suitable ANN can be found using an appropriate available set of input/output data in training mode and then, it can be tested for a new and again available set of input/output data, which have not been considered in the training procedure (using mode). Finally, if the neural network has been accepted as a suitable model, considering the acceptable error, the new set of inputs can be used and the unavailable outputs can be determined.

There are many types of Neural Networks [38] but the most popular and useful neural network model, which is also used in this thesis, is a Multilayer Perceptron (MLP), introduced below.

3.2.2 Multilayer Perceptron (MLP)

Multilayer Perceptron (MLP) consists of three different layers: input layer, hidden layer and output layer. Fig 3.7 shows a Multilayer Perceptron Neural Network for n input and m output variables.

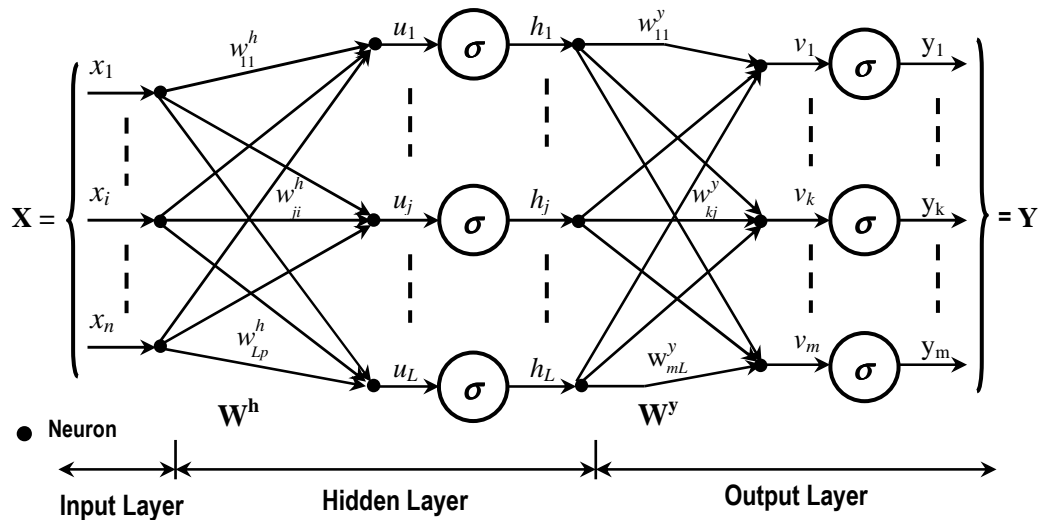


Fig. 3.7 Multilayer Perceptron with 3 layers (after [38])

- **Input Layer:** The input layer with n neurons (equal to the number of input variables) standardizes the input values, in a way that the range of each variable can be varied between -1 and 1. The input layer distributes the values to each of the neurons in the hidden layer

- **Hidden Layer:** Arriving at a neuron in the hidden layer, with L transfer functions, the value from each input neuron is multiplied by a weight (w_{ji}), and the resulting weighted values are added together producing a combined value u_j . Then u_j is fed into a transfer function σ , with the outputs of h_j .

The outputs from the hidden layer are then distributed to the output layer.

Note that it may be possible to choose more than one hidden layer for neural network structure. The question is: How to choose the number of hidden layers and nodes in a neural network?

To choose the optimal number of hidden layers, the performance difference of adding additional hidden layers is useful. If the situations in which performance improvements with a second (or third, etc.) hidden layer are very small, then increasing the number of hidden layers is not necessary. One hidden layer is sufficient for the large majority of problems.

To select the size of the hidden layer(s), there are some rules to find the optimal number of neurons [41], but the most commonly relied on, is: “the optimal size of the hidden layer is usually between the size of the input and size of the output layers”.

“Pruning” algorithm [42-44] describes also a set of techniques to trim network size (by nodes not layers) to improve computational performance and sometimes resolution performance. The goal of these techniques is removing nodes from the network during training by identifying those nodes which, if removed from the network, would not noticeably affect network performance (i.e., resolution of the data). Even without using a formal pruning technique, we can get a rough idea of which nodes are not important by looking at the weight coefficients after training.

By applying a pruning algorithm to the neural network during training, we can also find the optimal network configuration.

- **Output Layer:** Arriving at a neuron in the output layer with m neurons (equal to the number of output variables), the value from each hidden layer neuron is multiplied by a weight (w_{kj}), and the resulting weighted values are added together producing a combined value v_j . The weighted sum (v_j) is again fed into a transfer function σ , which outputs a value y_k . The y values are the outputs of the network.

In recent years neural network models are used extensively for wireless communication engineering, which eliminates the complex and time consuming mathematical procedures of designing antennas, like method of moments (MOM) [45-55]. Various ANN models are developed for determining resonant frequencies of antennas of various shapes [46, 47] and [52, 53]. In [51, 54], several designs have been presented using ANN models. A comprehensive review of applications of ANN in microwave engineering and different types of methods to develop the ANN models is discussed in [54, 55].

Multilayer Perceptron (MLP) neural network, with different number of hidden layer neurons as well as the weighting coefficients is used to model several problems in this thesis, using routines provided in MATLAB (Neural Network Toolbox).

CHAPTER 4 Performance Optimization of the MFSAA

In this chapter an optimization problem for the Monopole Four Square Array Antenna (MFSAA) mounted on an infinite ground plane is defined and the optimization is done using the optimization methods introduced in Chapter 3. For this purpose, three types of approximation models are considered for the MFSAA: First-order, second order and third order approximation model. Finally, the simulation results for radiation patterns demonstrate the possible performance improvement, if geometry and electrical parameters of the MFSAA as well as the feed network parameters can be optimized.

4.1 Optimization Problem

A typical optimization problem for the phased array implies high directivity, narrow beamwidth and low side lobes. A large number of theoretical approaches have been developed to solve this problem [56]. For the MFSAA, described in chapter 2 and mounted on an infinite ground plane with uniform element spacing d , length L , diameter D and the excitations I_i for each monopole antenna ($i = 1, \dots, 4$), the following criteria have been considered in the optimization problem to improve the performance of the MFSAA on an infinite ground plane [57].

4.1.1 Minimum Envelope Correlation of Beams

Following equation (2.41), the first criterion J_1 can be defined as the minimum envelope correlation between two neighboring beams of the MFSAA, with $\Delta\phi = 90^\circ$ difference between the maximum directions, as:

$$J_1(d, L, I_i) = |\rho| \quad (4.1)$$

J_1 is a function of element spacing d , length of each monopole L and excitations I_i . By minimizing this function the minimum envelope correlation of beams can be obtained.

4.1.2 Best fit to the ideal secant-squared elevation pattern

According to the equations (2.40) and (2.43), the second criterion is expressed as the following equation:

$$J_2(d, L, I_i) = \frac{1}{2} [K \sec^2(\theta) - D(\theta, \phi)]^2 \quad (4.2)$$

Factor $1/2$ is used for improvement of convergence in the optimization process.

J_2 is a function which by minimizing this function the best fit to the ideal secant-squared elevation pattern will be achieved. In this equation, D is the Directivity of the MFSAA and K is a constant, chosen in order to simplify the relationship, described in equation (4.3).

$$K = \frac{k_c}{k_t} \quad (4.3)$$

In equation above, k_c is another constant, expressed in equation (2.46) and k_t is the transmit antenna efficiency factor in equation (2.43). Note that the secant behavior is not required over all angles, but only over a certain range, such as $0 \leq \theta \leq \theta_{\max}$.

θ_{\max} corresponds to the maximum distance to the received antenna $R_{\max} = h \cos(\theta_{\max})$.

In this criterion, it has been considered that $\theta_{\max} = 90^\circ$. If the function J_2 can be minimized in a best way, then the transmit power P_t will be equal to the received power P_r in ‘‘Friis’’ equation (2.42).

4.1.3 Suitable Beam Crossover (BC) level

To obtain the suitable beam crossover level, described in section 2.4.5, the third criterion can be written as below.

$$J_3(d, L, I_i) = \frac{1}{2}(\beta - BC)^2 \quad (4.4)$$

Minimizing J_3 obtains the suitable crossover level of beams. In this equation, β is a constant and can be defined with respect to the considered suitable range for BC level (see section 2.4.5). For this criterion, the suitable BC range is considered to be between 0.5 (-3dB) and 0.25 (-6dB), and therefore $\beta = 0.354$ (-4.5dB) is defined for equation (4.4) as an optimum to give function J_3 its minimum value.

4.1.4 Maximum Front-to-Back (F/B) ratio

Following the definition of Front-to-Back ratio in section 2.4.4, the fourth criterion J_4 is defined as worst-case front-to-back ratio, as:

$$J_4(d, L, I_i) = (F/B) \quad (4.5)$$

J_4 is also a function of element spacing d , length of each monopole L and excitations I_i of four monopoles. In Table 2.2, it can be seen that the maximum value of F/B ratio of 446.6 (26.5dB) can be found for a separation $d = 0.271\lambda$. Using equation (4.5) it is possible to find this maximum by varying the element spacing d , as well as the length L and excitations I_i . Finally, by maximizing this function the maximum worst-case front-to-back ratio of the MFSAA can be achieved.

4.1.5 Maximum Directivity

According to the definition of Directivity in section 2.4.2, the fifth criterion can be considered as:

$$J_5(d, L, I_i) = D(\theta, \phi) \quad (4.6)$$

$D(\theta, \phi)$ is the directivity of the MFSAA in equation (2.39). Maximizing J_5 , the maximum Directivity of the MFSAA can be achieved.

4.1.6 Maximum Radiation Efficiency

Equation (2.11) describes the Radiation Efficiency of a monopole antenna as a function of length L and diameter D of each monopole antenna.

The sixth criterion can be defined as the following equation:

$$J_6(D, L) = \eta_r \quad (4.7)$$

where η_r is the radiation efficiency of each monopole antenna, which can vary between 0 and 1. By maximizing this function the maximum Efficiency of the array can be achieved.

4.2 First order approximation model

In this step, the first five performance criteria: 4.1.1 - 4.1.5 are applied for a simple antenna model (first order approximation model) which excludes the effects of antenna mutual coupling. For this simple model, four identical quarter-wave monopole antennas ($L = \lambda/4$) are used to create the MFSAA on an infinite ground plane, shown in Fig 2.11. It is assumed that the amplitude excitation of each monopole antenna is uniform $I_i = I_0$ ($i = 1, \dots, 4$) and the phases are fixed to 90° , 180° , 90° and 0° for the first, second, third and fourth antenna respectively (see Fig 2.11).

For this model, only the distance d between the elements is varied whereas all other parameters are fixed. $0 \leq \theta \leq 180^\circ$ and $0 \leq \phi \leq 360^\circ$ are also the ranges of both θ and ϕ in optimization procedure.

First, each criterion is optimized separately. Results for each criterion are shown separately in Fig 4.1, where three different ranges have been defined as optimal range (red), useful range (green) and unacceptable range (grey). It has been realized that the five criteria do not coincide at the same optimum element spacing, but the following corridor seems a good compromise:

$$0.252 \leq d/\lambda \leq 0.350 \quad (4.8)$$

A more precise determination of the optimum element spacing is obtained after defining a cost function with the appropriate weight factors as well as the condition in equation (4.8). In this way the main goal is to find the optimal distance d between the elements (in wavelength) based on the cost function in equation (4.9). The individual performance criteria have been grouped into criteria 4.1.1 to 4.1.3 which should be as small as possible and criteria 4.1.4 and 4.1.5 which should be as large as possible. The quotient of the two groups should be minimized to give an optimum result.

$$J(d) = \frac{\sum_{i=1}^3 W_i J_i^n}{\sum_{i=4}^5 W_i J_i^n} \quad (4.9)$$

In this equation, $J_i^n (i = 1, \dots, 5)$ is the normalized value of each criterion, obtained by dividing the equations (4.1), (4.2), (4.4), (4.5) and (4.6) by the maximum value of each J_i . For this purpose, each criterion has been analyzed separately and the maximum of each criterion has been found. E.g., Fig 2.12 shows that the maximum value of the fifth criterion in equation (4.6), considering the conditions indicated in section 2.4.2, which is 6.09 (7.84dB) and thus $J_5^n = J_5/6.09$. The range of each normalized criterion is thus balanced between 0 and 1.

To optimize the cost function (4.9), the direct search method in 3.1.2 is selected because of only one optimized parameter (d). After defining the weighting coefficients to be uniform ($W_i = 1$) and considering the equation (4.8) as the only constraint, the optimal distance d^{op} between the elements (in wavelength) has been found as $d^{op} = 0.319\lambda$. (see precise optimization result in Fig 4.1).

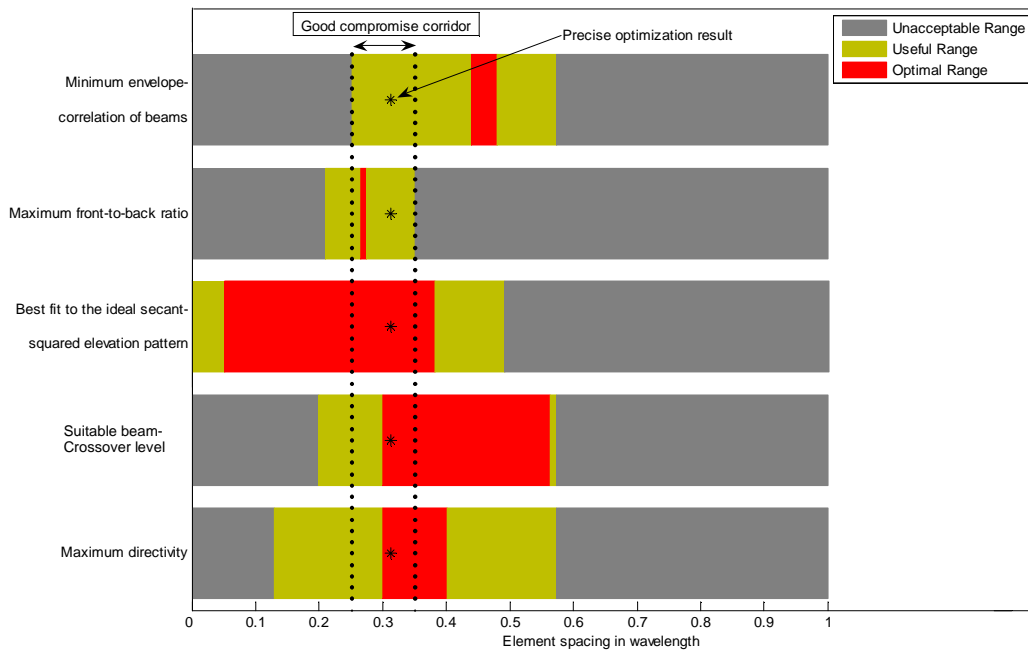


Fig. 4.1 Optimization results for the first order approximation model

Table 4.1 shows the values of the envelope correlation (ρ), normalized second criterion J_2^n (fit to the secant-squared elevation pattern), beam crossover (BC) level, (F/B) ratio and maximum directivity (D_0), when $d = d^{op} = 0.319\lambda$.

Parameter	ρ	J_2^n	BC	F/B	D_0
Value	0.16	0.34	3.2 dB	15 dB	7.8 dB

Table 4.1 Values of J_2^n , ρ , D_0 , (BC) and (F/B) for the MFSAA with $d = d^{op} = 0.319\lambda$.

Fig 4.2 shows the azimuth radiation pattern at the elevation beam peak $\theta = 90^\circ$ of the quarter-wave MFSAA for the optimal separation $d = d^{op} = 0.319\lambda$.

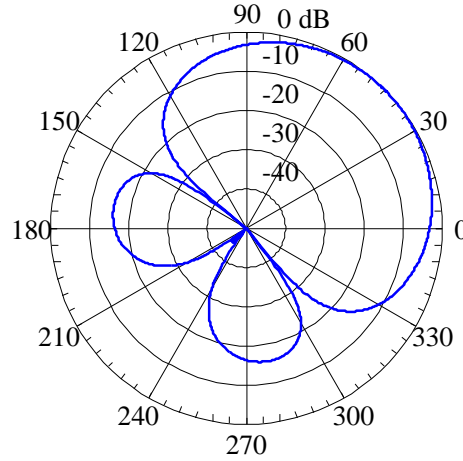


Fig. 4.2 Azimuth radiation pattern of the first-order approximation MFSAA

For uniform amplitude and symmetrical phase excitation I_i , the array pattern becomes symmetrical, as can be seen from this figure.

4.3 Second order approximation model

The next, more sophisticated optimization employs a second order approximation antenna model which considers the role of mutual coupling between the monopole antennas. In this step, we consider four identical realistic monopole antennas in the MFSAA, shown in Fig 2.11, of uniform variable length L and diameter D . The source impedance of the feed network Z_0 can be also varied arbitrarily but the source voltages of the feed network are chosen as equation (2.38).

In this step, the 6th criterion (Maximum radiation efficiency) in equation (4.7) is also considered to create the following cost function for the optimization procedure:

$$J(d, L, D, Z'_0, Z''_0) = \frac{\sum_{i=1}^3 W_i J_i^n}{\sum_{i=4}^6 W_i J_i^n} \quad (4.10)$$

In this equation, Z'_0 is the real part and Z''_0 the imaginary part of the source impedance Z_0 (equal for all monopole antennas).

J_i^n ($i=1\dots6$) is the normalized value of each criterion, as explained before and taken from equations (4.1), (4.2), (4.4), (4.5), (4.6) and (4.7) and can vary between 0 and 1.

W_i ($i=1\dots6$) are also the weighting coefficients which are limited to $\sum W_i = 6$.

Note that from the equations (2.36) and (2.37), it can be concluded that the excitations I_i can be expressed as a function of the impedance Source Z_0 , the source voltages V_{io} , L , D and d , but because the source voltages are fixed by equation (2.38), the cost function (4.10) can be expressed in terms of the variables d , L , D , Z'_0 and Z''_0 only.

Equations (2.38), (4.8) and the following conditions are considered as our constraints and weights in order to optimize the cost function (4.10).

$$0.15 \leq L/\lambda \leq 0.35 \quad (4.11)$$

$$0.004 \leq D/\lambda \leq 0.055 \quad (4.12)$$

$$35\Omega \leq Z'_0 \leq 150\Omega \quad (4.13)$$

$$-50\Omega \leq Z''_0 \leq 50\Omega \quad (4.14)$$

$$W_1 = W_4 = W_6 = 1.5 \quad (4.15)$$

$$W_2 = W_3 = W_5 = 0.5 \quad (4.16)$$

The range of L and D in equations (4.11) and (4.12) has been chosen due to the practical applications and limitations. Note that due to each application, the ranges of L and D can be changed optionally. The range of the source impedance in equations (4.13) and (4.14) is also due to the popular 50Ω source impedance with a limited range of transformation for the real part and $\pm j50\Omega$ for the imaginary part of the source impedance Z_0 .

For the purpose of optimizing the cost function, a Genetic Algorithm (GA) optimizer, described in section 3.1.3, with generations of 35 individuals each, crossover rate = 0.8 and mutation rate = 0.04 is used. Table 4.2 shows the optimal values of the parameters after optimization.

Parameter	d^{op}	L^{op}	D^{op}	$Z'_0{}^{op}$	$Z''_0{}^{op}$
Value	0.274λ	0.203λ	0.0072λ	147Ω	-35Ω

Table 4.2 Optimized variables, obtained by Genetic Algorithm optimizer

Using the optimal parameters in Table 4.2, the impedance matrix \mathbf{Z} of this MFSAA is expressed in equation (4.17).

$$\mathbf{Z} = \begin{bmatrix} 20.23 - 59.2j & 19.95 - 15.32j & 5.63 - 19.28j & 19.95 - 15.32j \\ 19.95 - 15.32j & 20.23 - 59.2j & 19.95 - 15.32j & 5.63 - 19.28j \\ 5.63 - 19.28j & 19.95 - 15.32j & 20.23 - 59.2j & 19.95 - 15.32j \\ 19.95 - 15.32j & 5.63 - 19.28j & 19.95 - 15.32j & 20.23 - 59.2j \end{bmatrix} \quad \Omega \quad (4.17)$$

As we can see from this matrix, the diagonally opposite antennas have smaller mutual impedances in magnitude in comparison to the neighboring antennas, due to the larger separation. Note that reducing the mutual impedances between antennas is another criterion, which will be considered in next chapters after considering the effect of the finite ground plane on the antennas additionally.

Very poor matching can also be seen by comparing the source impedance Z_0 in Table 4.2 with the diagonal elements of matrix (4.17). To improve the impedance matching of the MFSAA, an extended cost function will be considered in the third order approximation model.

The excitations I_i can also be found using equations (2.36) and (2.37) for this MFSAA:

$$\begin{bmatrix} I_1 \\ I_2 \\ I_3 \\ I_4 \end{bmatrix} = \begin{bmatrix} 0.88 \angle 90^\circ \\ 0.97 \angle 185^\circ \\ 0.88 \angle 90^\circ \\ 1 \angle 340^\circ \end{bmatrix} \quad \text{A} \quad (4.18)$$

As expected, the 1st and 3rd elements have the same excitation. The 2nd antenna has 5° differences in phase in comparison to the 2nd antenna in the first approximation model, while the 4th antenna has 20° differences in phase with respect to the 4th element in the first approximation model. Fig 4.3 shows the azimuth radiation pattern at the elevation beam peak $\theta = 90^\circ$ of the MFSAA corresponding to the optimized parameters in Table 4.2.

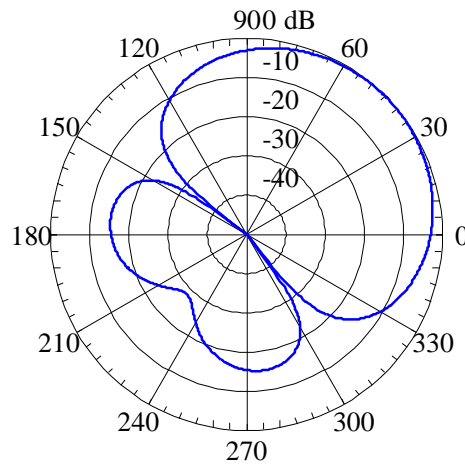


Fig. 4.3 Azimuth radiation pattern of second-order approximation MFSAA

As expected, a symmetric radiation pattern can be seen in this figure, due to the same excitation of the first and third elements. Table 4.3 shows the values of the envelope correlation (ρ), normalized second criterion J_2^n , beam crossover (BC) level, (F/B) ratio, maximum directivity (D_0), radiation efficiency η_r , mismatch efficiency η_M (calculated from equation (2.48)) and maximum absolute gain G_{0abs} (calculated from equation (2.47)), using the optimized variables of Table 4.2.

Parameter	ρ	J_2^n	BC	F/B	D_0	η_r	η_M	G_{0abs}
Value	0.32	0.31	3.35 dB	14.9 dB	8dB	71%	54%	3.84 dB

Table 4.3 Values of the MFSAA in the second order approximation model

The values of envelope correlation, beam crossover level and directivity are increased in this step in comparison to the first order approximation model (see Table 4.1), while the front-to-back ratio remains almost constant. The improvement of front-to-back ratio was to be expected due to reduced element spacing d . However, the element current excitation, equation (4.18), shows unequal amplitudes which degrades the F/B ratio from a 16.5dB result, possible for equal amplitudes with phases as given in equation (4.18); note that with equal amplitudes and 90° , 180° , 90° and 0° phases (as in equation (2.38)), the F/B ratio would even reach 23.8dB.

The poor value of the mismatch efficiency as well as the absolute gain of the MFSAA in this table is due to the MFSAA impedance mismatch. This is seen as a result of the particular choice of the criteria, where the directivity was included for optimization but neither the impedance mismatch nor the mismatch efficiency or absolute gain.

Note that, by changing the values of the weighting coefficients in equations (4.15) and (4.16), we can change our priorities and then the optimal values in both Tables 4.2 and Table 4.3 are changed.

4.4 Third order approximation model

Finally, in the third order approximation model, it is assumed that the source voltages of the feed network can be also changed over the following limited ranges:

$$\begin{pmatrix} 0.5 \\ 0.5 \\ 0.5 \\ 0.5 \end{pmatrix} \mathbf{V} \leq \begin{pmatrix} |V_{1o}| \\ |V_{2o}| \\ |V_{3o}| \\ |V_{4o}| \end{pmatrix} \leq \begin{pmatrix} 1.5 \\ 1.5 \\ 1.5 \\ 1.5 \end{pmatrix} \mathbf{V} \quad (4.19)$$

$$\begin{pmatrix} 70^\circ \\ 160^\circ \\ 70^\circ \\ -20^\circ \end{pmatrix} \leq \begin{pmatrix} \angle V_{1o} \\ \angle V_{2o} \\ \angle V_{3o} \\ \angle V_{4o} \end{pmatrix} \leq \begin{pmatrix} 110^\circ \\ 200^\circ \\ 110^\circ \\ 20^\circ \end{pmatrix} \quad (4.20)$$

where $|V_{io}|$ is the amplitude and $\angle V_{io}$ is the phase of the source voltage V_{io} ($i=1,\dots,4$). In this step the number of optimized parameters is increased from 5 to 13 parameters.

Another criterion is also considered in the new cost function for this approximation model: To match the self impedance of each antenna to the characteristic impedance and also minimize the mutual impedance between antennas, the following criterion is defined in this step.

$$J_7(d, L, D, Z'_0, Z''_0) = \text{magnitude}(Z_0 - Z_{11}^*) + \text{magnitude}(Z_{21}) + \text{magnitude}(Z_{31}) \quad (4.21)$$

where $Z_0 = Z'_0 + jZ''_0$ is the source impedance, Z_{11}^* is the complex conjugate of the self impedance Z_{11} , Z_{21} is the mutual impedance between neighboring antennas and Z_{31} is the mutual impedance between diagonally opposite antennas.

The following cost function is considered for this approximation model:

$$J(d, L, D, Z'_0, Z''_0, |V_{1o}|, |V_{2o}|, |V_{3o}|, |V_{4o}|, \angle V_{1o}, \angle V_{2o}, \angle V_{3o}, \angle V_{4o}) = \frac{\sum_{i=1}^3 W_i J_i^n + W_7 J_7^n}{\sum_{i=4}^6 W_i J_i^n} \quad (4.22)$$

In this step the cost function above with conditions, indicated in equations (4.8), (4.11)-(4.14), (4.19)-(4.20) and the following weighting coefficients ($\sum W_i = 6$) are considered in our global optimization problem.

$$W_1 = W_4 = W_6 = W_7 = 0.75 \quad (4.23)$$

$$W_2 = W_3 = W_5 = 1 \quad (4.24)$$

A Genetic Algorithm (GA) optimizer, with generations of 35 individuals each, *crossover rate* = 0.8 and *mutation rate* = 0.04 is designed to optimize the cost function (4.22).

The following table shows the optimal values of the parameters after optimization.

Parameter	d^{op}	L^{op}	D^{op}	$Z_0'^{op} + jZ_0''^{op}$
Value	0.34λ	0.23λ	0.039λ	$31 + j6\Omega$
Parameter	$ V_{1o} / V$	$\angle V_{1o}$	$ V_{2o} / V$	$\angle V_{2o}$
Value	0.9	76°	0.85	188°
Parameter	$ V_{3o} / V$	$\angle V_{3o}$	$ V_{4o} / V$	$\angle V_{4o}$
Value	0.88	82°	1.15	3.5°

Table 4.4 Optimized variables obtained by Genetic Algorithm optimizer with 13 variables

Moderate modifications of source voltages and much lower source impedance can be seen in this table.

Considering the optimal values of d^{op} , L^{op} and D^{op} , the impedance matrix \mathbf{Z} of this MFSAA, can be expressed in equation (4.25).

$$\mathbf{Z} = \begin{bmatrix} 28.8-1.2j & 10.21-18.6j & -4.5-16.2j & 10.21-18.6j \\ 10.21-18.6j & 28.8-1.2j & 10.21-18.6j & -4.5-16.2j \\ -4.5-16.2j & 10.21-18.6j & 28.8-1.2j & 10.21-18.6j \\ 10.21-18.6j & -4.5-16.2j & 10.21-18.6j & 28.8-1.2j \end{bmatrix} \Omega \quad (4.25)$$

As this matrix shows, the self impedance has been better matched to the source impedance of the network, but the relative magnitude of the mutual impedances didn't change much in comparison to the previous results without considering a mutual coupling as a criterion.

This means that a decoupling and matching network for MFSAA is necessary to obtain considerably less mutual coupling between antennas. In the next chapter, a procedure will be introduced in order to design a decoupling and matching network (DMN), considering the mutual coupling between antennas and also between each antenna and finite ground plane (chassis).

Using the optimized variables in Table 4.4, the excitation I_i can be found using equations (2.36) and (2.37):

$$\begin{bmatrix} I_1 \\ I_2 \\ I_3 \\ I_4 \end{bmatrix} = \begin{bmatrix} 0.64 \angle 90^\circ \\ 1 \angle 203^\circ \\ 0.62 \angle 95^\circ \\ 0.58 \angle 344^\circ \end{bmatrix} \text{ A} \quad (4.26)$$

We still see variations in the element current amplitudes versus the originally uniform excitation, however, more deviation than in result (4.18) from the second order approximation model. The 2nd and the 4th antennas have +23° and -16° differences in phase with respect to the antennas in the first approximation model respectively. We also note that the currents I_1 and I_3 are similar but not equal, which yields a slightly asymmetric pattern. This has to be expected since pattern symmetry was not a criterion and other criteria exhibit little dependence on symmetry. In section 5.3.7.3, new constraints will be considered for the optimization problem to obtain a symmetric radiation pattern.

Fig 4.4 shows the azimuth radiation pattern at the elevation beam peak $\theta = 90^\circ$ of the MFSAA in this step.

As we can see from this figure, the mutual coupling of radiators still causes pattern degradation, compared with the pattern in Fig 4.2 which ignores mutual coupling. In particular, we see slight asymmetry in the lobes shape and in the level of the back lobes.

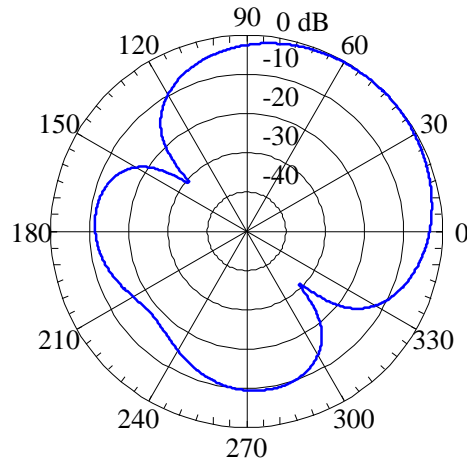


Fig. 4.4 Azimuth radiation pattern of third-order approximation MFSAA

In comparison to the results obtained from the second order approximation model, the front-to-back ratio has decreased due to both the large separation d and the particular excitation I_i in equation (4.26).

Table 4.5 shows the values of the envelope correlation (ρ), normalized second criterion J_2^n (fit to the secant-squared elevation pattern), beam crossover (BC) level, (F/B) ratio, maximum directivity (D_0), radiation efficiency η_r , mismatch efficiency η_M and maximum absolute gain G_{0abs} , using the optimized variables of Table 4.4.

Parameter	ρ	J_2^n	BC	F/B	D_0	η_r	η_M	G_{0abs}
Value	0.37	0.28	2.96 dB	9.8 dB	7.72 dB	76%	98%	6.45 dB

Table 4.5 Values of the MFSAA in third order approximation model

Comparing the values in this Table to the Table 4.3, it can be seen that the values of the mismatch efficiency and gain are increased due to the impedance matching of the MFSAA.

Again, note that, by changing the values of the weighting coefficients in equations (4.23) and (4.24), the results in Table 4.5 can be matched to the priorities, defined in the optimization problem.

In this chapter the optimization problem for a “Monopole Four-Square Array Antenna” mounted on an infinite ground plane has been considered and optimization results have been found using the optimization methods, introduced in chapter 3. In the next chapter, a finite ground plane (chassis) will be introduced and optimization will be done considering the effect of chassis.

On the other hand, as can be seen from the results of the \mathbf{Z} matrices both in second and third order approximation models, a decoupling and matching network (DMN) for the MFSAA is also required, which will be designed and applied in the next chapter.

CHAPTER 5 MFSAA on a finite ground plane (Chassis)

Feed point impedance and mutual coupling of monopole array elements on a finite ground plane (chassis) have been found to depend critically on the ground plane size and the position of each antenna [1]. This is due to the excitation of the modes of the chassis, which acts as an additional radiator element parasitically coupled to the array elements [1]. In this chapter, first, the theory of characteristic modes will be introduced and the effect of the excitation of chassis modes will be discussed. A neural network is also designed in this chapter to calculate the chassis modes excitation. After that, the performance optimization of the MFSAA on a chassis is defined and optimization is performed in this chapter. For this purpose, as well as all optimized parameters found in chapter 4, the size of the chassis is also optimized in order to minimize the new cost function, considered for the optimization problem. After that, a decoupling and matching network (DMN) for the MFSAA mounted on a chassis will be defined and realized to minimize the combined coupling between the antennas and also between chassis and antennas.

Finally, a full degree optimization problem is defined and a Neural Network model as well as the Genetic algorithm optimizer is used in the optimization procedure.

5.1 Theory of Characteristic Modes (TCM)

The theory of characteristic modes was first developed by Garbacz [3] and was later refined by Harrington and Mautz [2, 58]. By definition, characteristic modes are current modes obtained numerically for arbitrarily shaped conducting bodies.

Since characteristic modes are independent of any kind of excitation, they only depend on the shape and size of the conducting object.

C. Fabr es [59] has used the characteristic modes in an antenna design procedure, performed in two steps: First, the shape and size of the radiating elements are optimized. If the size of the element is scaled, the resonant frequency of the modes will only be scaled, whereas if the shape of the element is varied, not only the resonant frequency but also the radiating properties of the modes will change. Next, the optimum feeding configuration is chosen so that the desired modes may be excited. Few modes are needed for modeling electrically small conducting bodies. Thus, small and intermediate-size antennas can be fully characterized in a wide operating band by just considering two to four characteristic modes.

As the theory of characteristic modes is extensively described in [2, 58] only a review of the mathematical formulation of this theory is considered below (see Appendix for more details).

5.1.1 Mathematical formulation of characteristic modes

As explained in [2], characteristics modes of a conducting body can be obtained from the eigenfunctions of the following particular eigenvalues equation:

$$X(\mathbf{J}_n) = \lambda_n R(\mathbf{J}_n) \quad (5.1)$$

where the λ_n are the eigenvalues, the \mathbf{J}_n are the eigenfunctions or eigencurrents and R and X are the real and imaginary parts of the impedance operator:

$$Z = R + jX \quad (5.2)$$

The impedance operator Z is obtained after formulating an integro-differential equation [2]. It is known from the reciprocity theorem that if Z is a linear symmetric operator, then, its Hermitian parts, R and X , will be real and symmetric operators (see Appendix). From this, it follows that all eigenvalues λ_n in equation (5.1) are real, and all the eigenfunctions \mathbf{J}_n , can be chosen real over the surface on which they are defined [2].

In practice, to compute characteristic modes of a particular conducting body, Equation (5.1) needs to be reduced to a matrix form, as explained in [58], using a Galerkin formulation [60]:

$$\mathbf{X} \mathbf{J}_n = \lambda_n \mathbf{R} \mathbf{J}_n \quad (5.3)$$

Now the eigenvectors \mathbf{J}_n and eigenvalues λ_n , of the object are obtained by solving the generalized eigenproblem of equation (5.3) with standard algorithms [61] for each frequency. Note that the number of characteristic modes for a structure depends on its dimensions in terms of wavelength and is directly related to the size of $\mathbf{Z} = \mathbf{R} + j \mathbf{X}$ matrix, if the Method of Moments (MoM) [59] is used to simulate the structure.

The following steps have to be used to find the eigenvalues and the resonance modes of each structure: (see the Appendix)

- Select the first frequency f_1
- Calculate the \mathbf{Z} matrix ($n \times n$) of the structure, e.g. using the Method of Moments [56]
- Solve the equation (5.3) to find the eigenvectors $\mathbf{J} = [\mathbf{J}_1 \mathbf{J}_2 \dots \mathbf{J}_n]_{n \times n}$ and eigenvalues $\boldsymbol{\lambda} = [\lambda_1 \lambda_2 \dots \lambda_n]_{1 \times n}$
- Choose the next frequency and repeat the steps as indicated above

Finally, it is possible to find the variation of eigenvalues with frequency and find the eigen (resonance) frequency of the n^{th} mode, when $\lambda_n = 0$.

The quality factor Q_n of the n^{th} mode can be calculated by taking the derivative of the eigenvalues with respect to the frequency:

$$Q_n = \omega_n \left| \frac{d\lambda_n}{d\omega} \right|_{\omega=\omega_n} \quad (5.4)$$

The quality factor of a resonant mode measures how sharp its resonance is.

As an example, Fig 5.1 shows the frequency dependence of the eigenvalues in the frequency range from 820MHz to 4820MHz for a 10cm×10cm chassis [62].

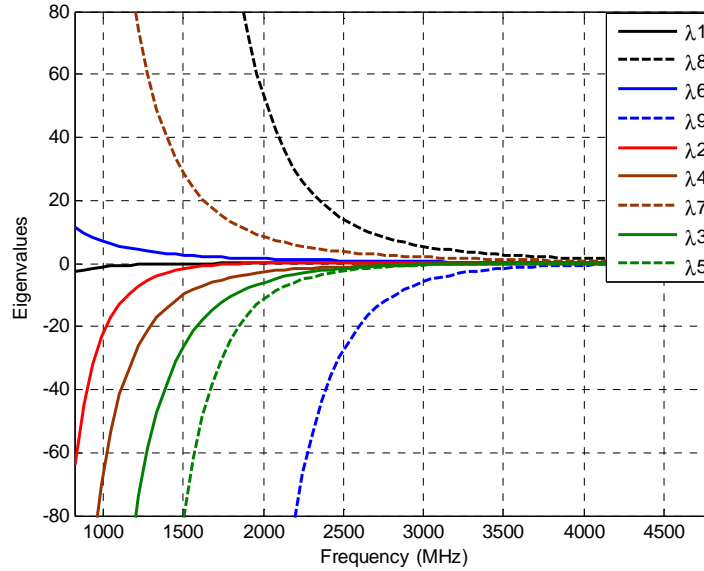


Fig. 5.1 Frequency dependence of the first 9 eigenvalues for a 100mm×100mm chassis, taken from [62]

From this figure, three resonances ($\lambda_n(\omega) = 0$) can be observed in the given frequency range (λ_1 , λ_2 and λ_3) and the other modes have no resonances in this frequency range. Table 5.1 shows also the resonance frequencies and radiation quality factors at the resonances.

	f_0 (GHZ)	Q_n
1st mode (λ_1)	1.33	0.44
2nd mode (λ_2)	2.45	2.86
3rd mode (λ_3)	3.35	2.19

Table 5.1 The first 3 characteristic mode resonances and their corresponding radiation quality factors for 100mm×100mm chassis

Note that calculations may provide a large number of characteristic modes from a chassis. In this situation, a systematic procedure has to be used to identify the important modes of the chassis [59]. The information provided by chassis modes is very helpful to design the antenna systems, which will be mounted on the chassis. For clarification, the eigencurrents distribution as well as the radiation patterns corresponding to the first, second and third resonance modes of a 100mm×100mm chassis are shown in Fig 5.2.

The figure shows the three current modes with x-directed polarization. On a quadratic chassis the y-directed current modes exist as degenerate eigenmodes. The first and third chassis mode, Fig 5.2 (a) and (c), show even symmetry of currents along the y-axis and produce radiation normal to the chassis (x-z-plane). The second chassis mode exhibits odd symmetry which produces a radiation null in the x-z-plane and two lobes with phase opposition.

The antennas (e.g. the MFSAA) attached to the chassis produce surface current distributions which can couple to these current modes to a degree depending on the correlation of current distributions (antenna and chassis mode) and on the frequency deviation from the chassis mode eigenfrequency (resonance) and on the chassis mode Q-factor. The excitation of a chassis mode by the antenna leads to additional radiation from the chassis mode which is superimposed to the original pattern of the antenna.

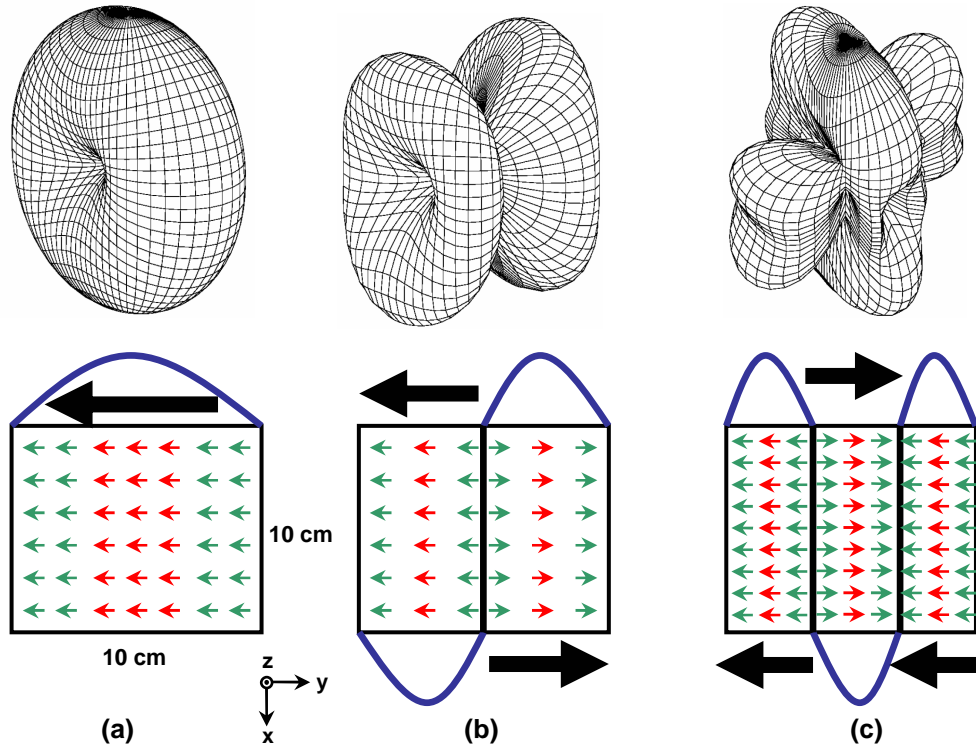


Fig. 5.2 Surface current densities and the radiation patterns for characteristic modes of a 10cm×10cm chassis, after [63] (a): First, (b): second and (c): third chassis modes

Knowing the resonance frequencies of the chassis modes can be used to design the antenna system that utilizes the chassis as main radiator or on the other hand, to avoid the chassis radiation. As an example, in [1] a two-element monopole array has been evaluated on a chassis, considering the chassis modes excitation.

In [1], it has been found that the excitation of the lowest order chassis mode strongly influences the feed point impedance and mutual coupling of monopole array elements as a function of the chassis size. The reason is that this fundamental mode (seen in Fig 5.2 (a)), acts as an additional radiator element parasitically coupled to the array elements.

As indicated in the Appendix, calculating the chassis modes as well as selecting the suitable modes is difficult and needs high execution time for running the programs (e.g. in MATLAB). To find a model for calculating the eigenvalues $\lambda = [\lambda_1 \lambda_2 \dots \lambda_n]_{1 \times n}$ of the chassis modes, a Neural Network model is designed and implemented below.

5.1.2 A Neural Network model to calculate the chassis mode eigenvalues

In this part, a new method using a neural network, as explained in chapter 3, is used to calculate the eigenvalues of a chassis with arbitrary dimensions.

The goal is to design a neural network model for the calculation of the first 20 eigenvalues of a chassis with dimensions of $x_1(\text{mm}) \times x_2(\text{mm})$, for 71 frequencies in the range of 820 MHz to 4820 MHz.

The input and output variables are defined as:

$$\mathbf{I} = [x_1(\text{mm}) \quad x_2(\text{mm}) \quad f(\text{MHz})] \quad (5.5)$$

$$\mathbf{O} = [\lambda_1 \quad \lambda_2 \quad \dots \quad \lambda_{20}] \quad (5.6)$$

where λ_n is the eigenvalue of the n^{th} chassis mode at frequency f (MHz). The required 14200 data sets for input/output (71 frequency sets \times 20 eigenvalues \times 10 different chassis sizes) were taken from [62, 63], as shown below.

Chassis Size #1			
Frequency	λ_1	-----	λ_{20}
$f_1 = 820 \text{ MHz}$	λ_{11}	-----	$\lambda_{20,1}$
f_2	λ_{12}	-----	$\lambda_{20,2}$
⋮	⋮	⋮	⋮
$f_{71} = 4820 \text{ MHz}$	$\lambda_{1,71}$	-----	$\lambda_{20,71}$
	⋮		
Chassis Size #10			
Frequency	λ_1	-----	λ_{20}
$f_1 = 820 \text{ MHz}$	λ_{11}	-----	$\lambda_{20,1}$
f_2	λ_{12}	-----	$\lambda_{20,2}$
⋮	⋮	⋮	⋮
$f_{71} = 4820 \text{ MHz}$	$\lambda_{1,71}$	-----	$\lambda_{20,71}$

Fig. 5.3 Required 14200 data sets taken from [62, 63] to learn the neural network model

To design a neural network model, 12780 data for 9 different chassis sizes from the available data sets are used in the training phase to learn the network and 1420 data for one chassis size are used in the testing phase only.

In training phase, four different Multilayer Perceptron (MLP) structures with different number of layers, as explained in chapter 3, are considered in MATLAB to find the suitable structure and minimum error in testing phase.

Fig 5.4 shows the ANN surface for this problem.

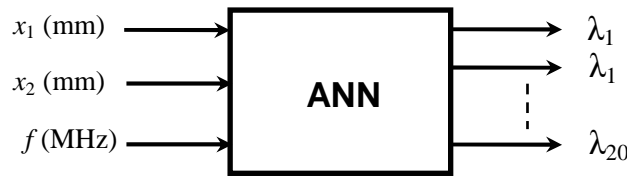


Fig. 5.4 Surface of the Neural Network model to calculate the chassis modes

The first MLP structure is designed to have 3 input cells, 3 input neurons for input layer, 4 hidden neurons for hidden layer, 20 output neurons for output layer and 20 output cells. The number of neurons in hidden layer is increased to 8, 12 and 16 neurons for the second, third and fourth MLP structure to find the suitable model regarding the minimum error in testing phase. These different types of MLP are named as MLP (3-3-4-20-20), MLP (3-3-8-20-20), MLP (3-3-12-20-20) and MLP (3-3-16-20-20). Fig 5.5 shows different types of the Neural Network model to calculate the chassis modes.

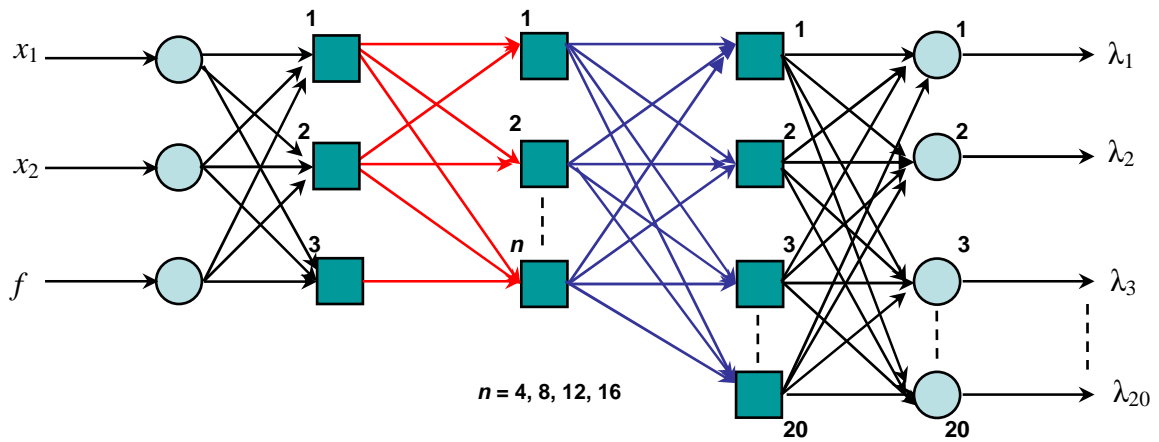


Fig. 5.5 Different structures of the Neural Network model to calculate the chassis modes

12780 data are used for each MLP structure to learn the network. After that the value of average testing error, defined in equation (5.7), is calculated using 1420 data sets reserved for testing.

$$e = \sqrt{\frac{\sum_{j=1}^{71} \sum_{i=1}^{20} (\lambda_{i,j}^{Test} - \lambda_{i,j}^{NN})^2}{1420}} \quad (5.7)$$

where $\lambda_{i,j}^{Test}$ is the eigenvalue of i^{th} mode at j^{th} frequency of testing set, which has not been used in training phase. $\lambda_{i,j}^{NN}$ is the eigenvalue of i^{th} mode at j^{th} frequency of the trained Neural Network using the input data sets of testing phase. The value of error e in equation (5.7) is found for each structure of MLP in MATLAB. Fig 5.6 shows the model accuracy comparison (average error e for testing data) between MLPs with different hidden neurons.

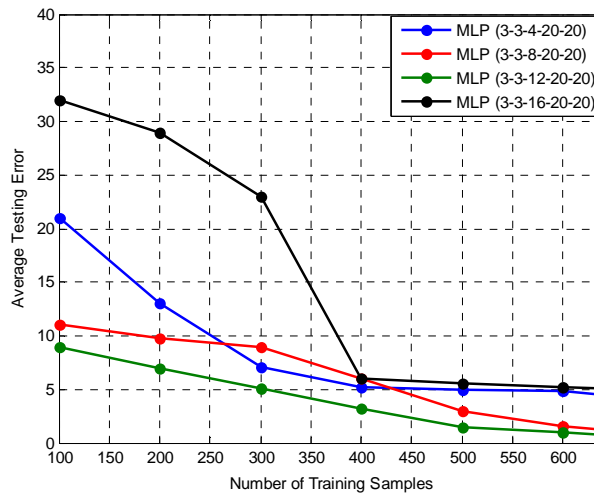


Fig. 5.6 Model accuracy comparison (average error on test data) between MLPs with different number of hidden neurons

As Fig 5.6 shows, MLP (3-3-12-20-20) model is best suited and has been chosen for the structure of Neural Network model in further steps.

Next, this MLP structure is used to find the variation of the eigenvalues of each mode with frequency. The available data for the chassis with dimensions of $x_1 = 100$ mm and length of $x_2 = 30$ mm is used for testing the neural network structure. Note that these data have not been used in the training procedure.

Fig 5.7 shows the eigenvalues of the first and second modes, calculated by the neural network in comparison to the original data sets.

This figure shows a good agreement between the results obtained from a neural network structure and the original data which have not been used during the design process of neural network.

Other results for other modes show also a good accuracy of the neural network; however a slight degradation in the accuracy of this model can be seen in higher modes, which have extreme eigenvalues.

The conclusion is that, this model can be used to determine the chassis modes with arbitrary dimensions of the chassis within the limits of the employed data set.

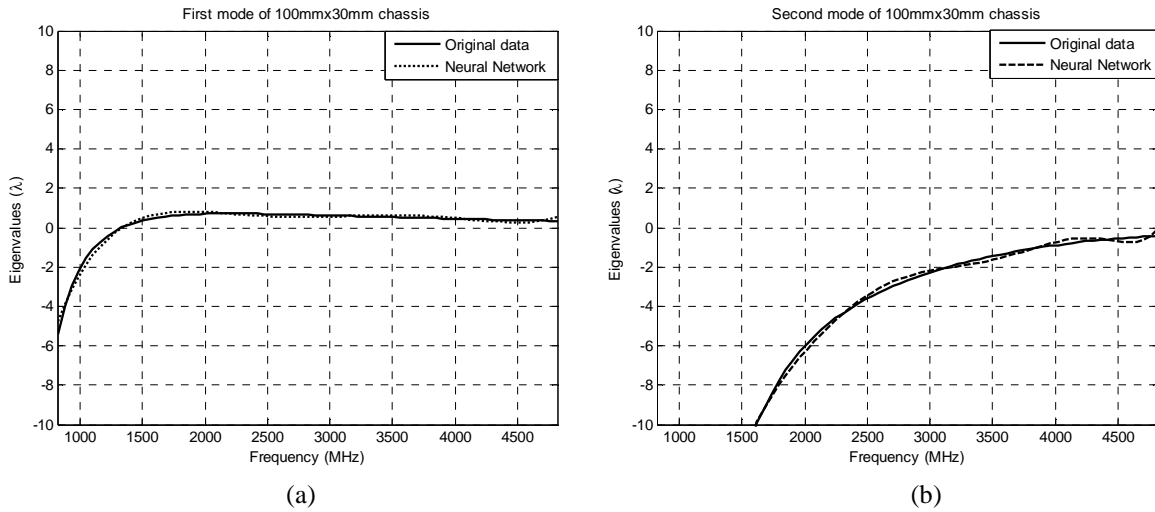


Fig. 5.7 Eigenvalues of the first (a) and second (b) modes, calculated by the neural network in comparison to the original data sets

5.2 Effects of the finite ground plane (chassis)

The self and mutual impedances of a monopole array antenna, mounted on a finite ground plane (chassis) have been found to depend strongly on the chassis dimensions due to the excitation of characteristic modes [1]. A number of studies have also been done to understand the effects of the length of the metal chassis of a handheld device on the impedance bandwidth, e.g., [64, 65]. These indicate that if the chassis resonates at the operating frequency of the antenna element, the bandwidth of the antenna-chassis combination increases strongly. Ali, et al in [66] have also shown that the optimum antenna near field performance can be achieved when the antenna resonance frequency is aligned with the chassis resonance frequency. In the following, the foundations regarding the effects of the chassis on the monopole antenna performances are described, in order to be used in our optimization procedure. Effects of the chassis on the monopole antennas are found by EM-field simulations for a number of configurations of monopoles and chassis. Note that in any case the calculated impedances and radiation patterns include basic monopole properties as also seen on an infinite ground plane and that direct results of chassis mode excitation is not easily isolated.

5.2.1 Single monopole antenna on a chassis

Consider a single monopole antenna mounted on a chassis, as shown in Fig 5.8. The chassis and monopole antenna dimensions are considered to have fix values as: $x_1 = x_2 = 100\text{mm}$, $H = 1\text{mm}$, $L = 31\text{mm}$, $D = 1\text{mm}$. Consider that the single monopole antenna can move from the centre of the chassis to the chassis edge and the variable S (distance between the monopole antenna and the chassis edge) can be changed arbitrary.

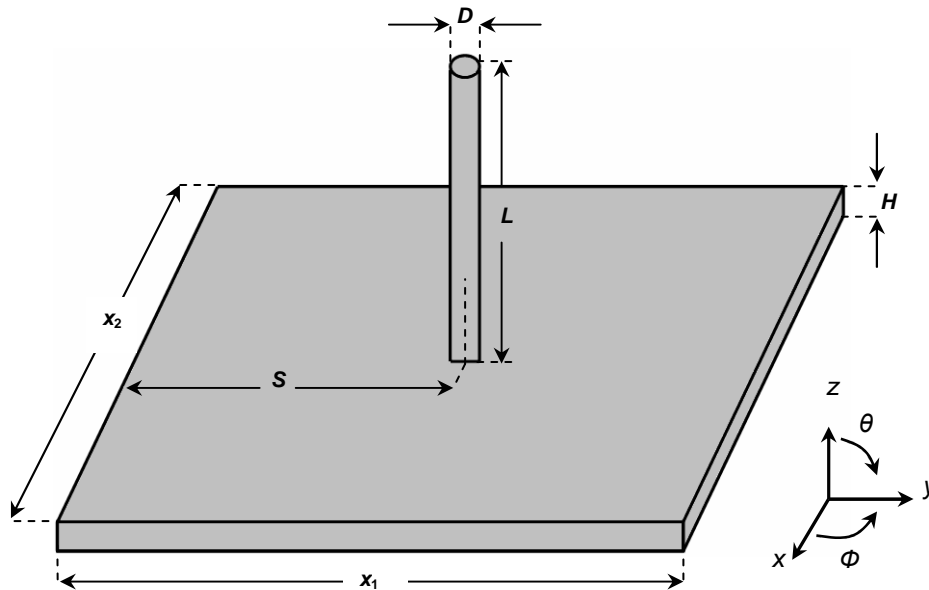


Fig. 5.8 Single monopole antenna mounted on a chassis

The reflection coefficient of this monopole antenna, when mounted on an infinite ground plane can be named as $S_{11}(\text{inf})$ and the reflection coefficient of the antenna mounted on $100\text{mm} \times 100\text{mm}$ chassis in a distance of S from the chassis edge is simulated at four different distances: $S_{11}(S = 5\text{cm})$, $S_{11}(S = 3.6\text{cm})$, $S_{11}(S = 2.2\text{cm})$ and $S_{11}(S = 0.8\text{cm})$; calculations of EM-fields and network parameters have been performed using the EMPIRE simulator.

Fig 5.9 shows the differences between $S_{11}(\text{inf})$ and $S_{11}(S \text{ cm})$ in linear format at each frequency. The resonance frequency of the monopole antenna is at 2.27 GHz.

When the monopole antenna is mounted in the centre of the chassis (see Fig 5.9 (a)), the second chassis mode at the frequency of 2.45 GHz can be seen clearly. This mode can be excited if the monopole antenna is mounted in the centre because of its anti-symmetric current distribution which coincides with an anti-symmetric current distribution of the monopole (along the y -axis). On the other hand, the first and third chassis modes can not couple due to cancellation of symmetric chassis mode current and anti-symmetric monopole current contributions (see Fig 5.2).

The first and third chassis resonance frequencies at 1.33 GHz and 3.35 GHz respectively can best be seen in Fig 5.9 (d), where the monopole antenna is near to the chassis edge.

If the monopole antenna is close to the chassis edge, its currents are forced to flow very asymmetric on the chassis along the y -axis. Since all three chassis modes show a current distribution decaying towards the chassis edge with uniform current direction, the coupling of the y -directed currents of monopole and chassis modes is dominated by the imbalance of the monopole current in y - and anti- y -directions, so that all three modes appear excited.

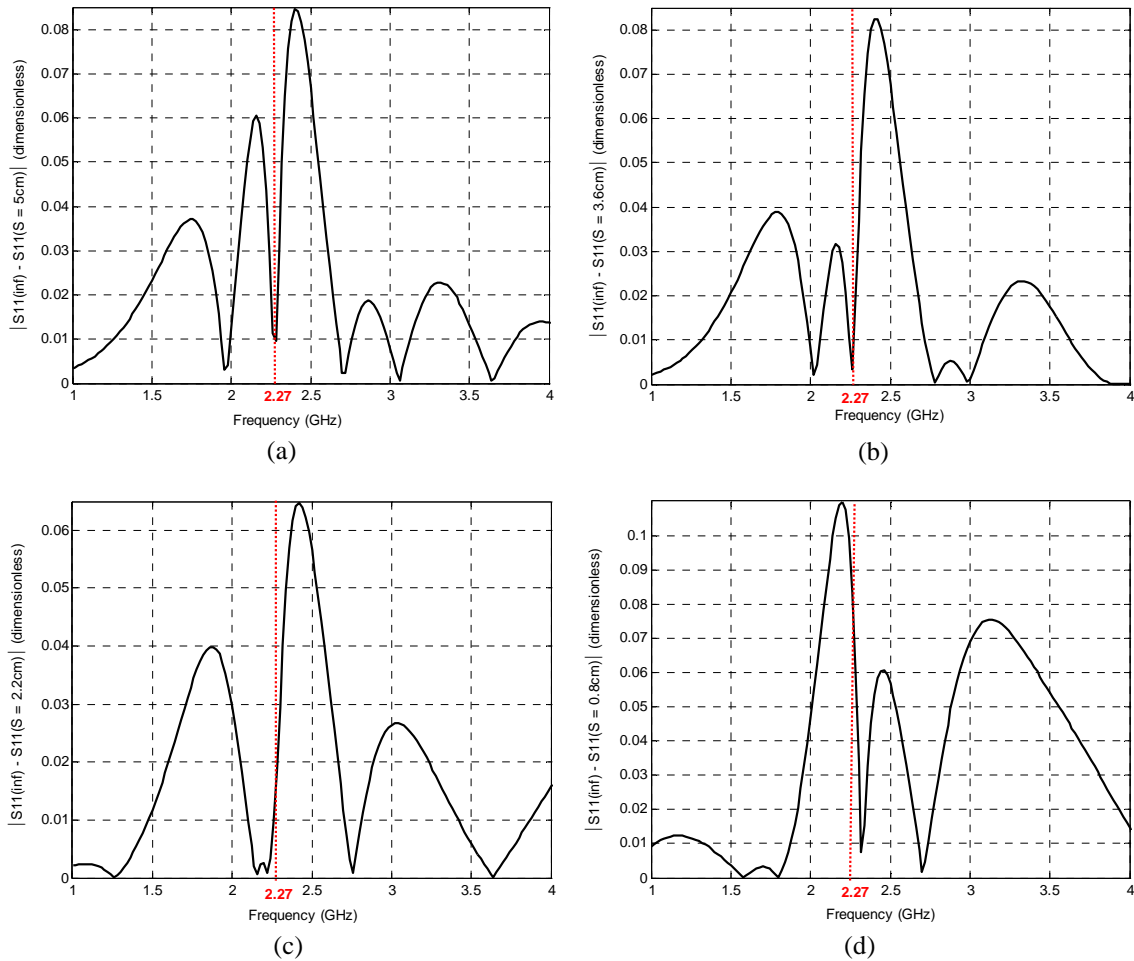


Fig. 5.9 Differences between $S_{11}(\text{inf})$ and $S_{11}(S \text{ cm})$ in linear format. a) $S=5\text{cm}$, b) $S=3.6\text{cm}$, c) $S=2.2\text{cm}$ and d) $S=0.8\text{cm}$

Considering the monopole antenna in a distance of $S = 0.8 \text{ cm}$ from the chassis edge ($10\text{cm} \times 10\text{cm}$ chassis), it is interesting to simulate the transmission S-parameters (coupling) between the chassis and the monopole antenna. For this purpose, a model in the EMPIRE simulator has been set-up with two coaxial ports with a same ground as PEC (Perfect Electric Conductor) as seen Fig 5.10.

Fig 5.11 shows the transmission S-parameters, simulated for the configuration.

The first and third chassis mode can be easily detected in Fig 5.11 because of the position of the monopole antenna on the chassis (near to edge).

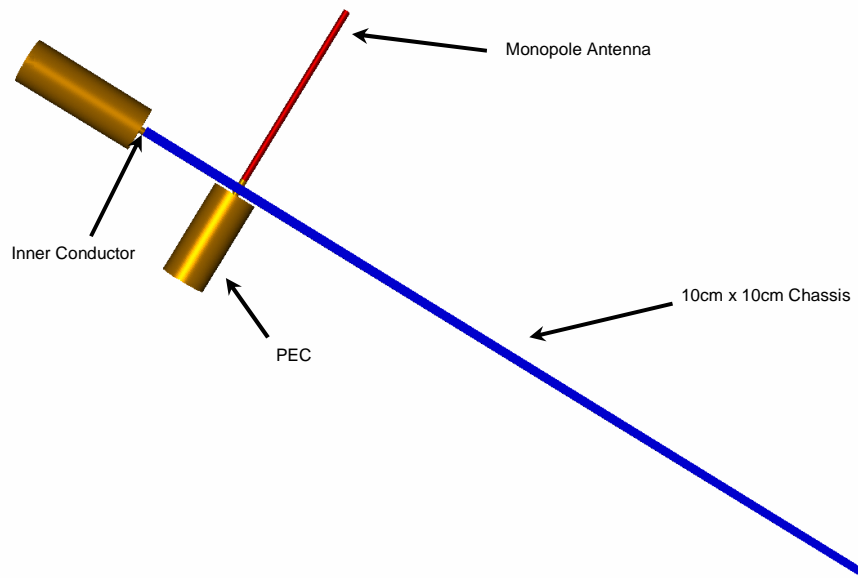


Fig. 5.10 Monopole antenna on a chassis with two coaxial ports to simulate the coupling between antenna and chassis

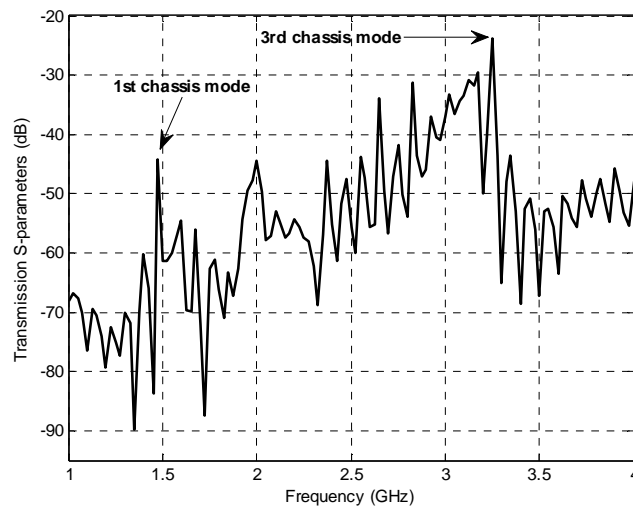


Fig. 5.11 Transmission S-parameters between monopole antenna and 100mm×100mm chassis

The effect of the chassis modes can be also found in the far-field radiation pattern of the monopole antenna, mounted on a chassis. The results in Fig 5.12 can be found for the elevation far-field radiation pattern of the monopole antenna calculated at the chassis resonance frequencies for $S = 0.8\text{cm}$ and $S = 5\text{cm}$.

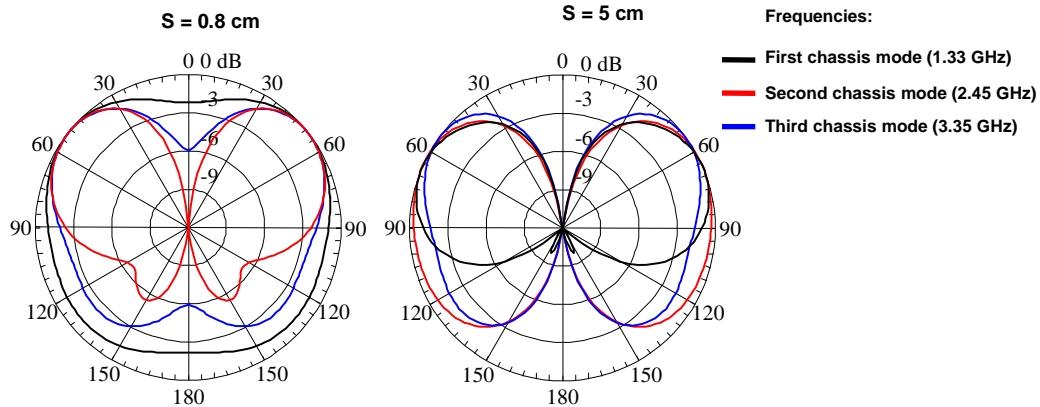


Fig. 5.12 Elevation radiation pattern of a monopole antenna mounted on a 100mm×100mm chassis ($\phi=90^\circ$) at the chassis resonance frequencies for $S = 0.8\text{cm}$ and $S = 5\text{cm}$.

The radiation pattern of the monopole antenna changes in a typical manner after mounting on a finite ground plane, as can be seen from Fig 5.12, compared to Fig 2.3. The pattern shown in Fig 5.12 for $S = 5\text{cm}$ and $f = 1.33\text{GHz}$ is closest to the pattern of a monopole on an infinite ground plane; we just see some diffraction around the corners, producing some radiation into the back hemisphere and an uptilt of the beam.

At higher frequencies (patterns at 2.45GHz and 3.35GHz) we find the back lobes increased to even symmetrical pattern (at the resonance frequency of the second chassis mode) which indicates a strong excitation of the anti-symmetric second chassis mode.

In any case, patterns keep the deep null along the z-axis, which shows that the chassis-mode currents excited by the monopole at the chassis center are purely of the anti-symmetric type of the second chassis mode.

The symmetric chassis modes are seen to be excited by the monopole at the offset position close to the edge of the chassis at $S = 0.8\text{cm}$: The pattern at 1.33 GHz shows a very strong filling of the null, the pattern at 3.35GHz less and at 2.45GHz no filling is seen. The filling can be understood as the radiation contribution from the symmetric chassis mode currents which produce lobes along the z-axis. At 2.45GHz, the excitation of the first and third chassis mode seems to be very low (no filling is seen within the dynamic range of the pattern plots) but some increase in the back directed lobes indicates a limited excitation of the anti-symmetric second chassis mode currents.

In both monopole positions we observe radiation patterns that extend over both the upper and the lower (back) hemisphere with even nearly equal magnitudes. This is a clear indicator that this radiation is due to currents flowing on the chassis in x-y plane, while the currents of the monopole over a ground plane clearly produce radiation concentrated on the upper hemisphere.

For another demonstration of the effects of chassis modes, consider the monopole antenna on a chassis, depicted in Fig 5.8 with $x_2=100\text{mm}$, $H = 1\text{mm}$, $L = 31\text{mm}$, $D = 1\text{mm}$ and $S = 0.8\text{cm}$. The reflection coefficients of the single monopole antenna are simulated for four different chassis lengths ($x_1=76\text{mm}$, $x_1=56\text{mm}$, $x_1=36\text{mm}$ and $x_1=16\text{mm}$) as shown in Fig 5.13.

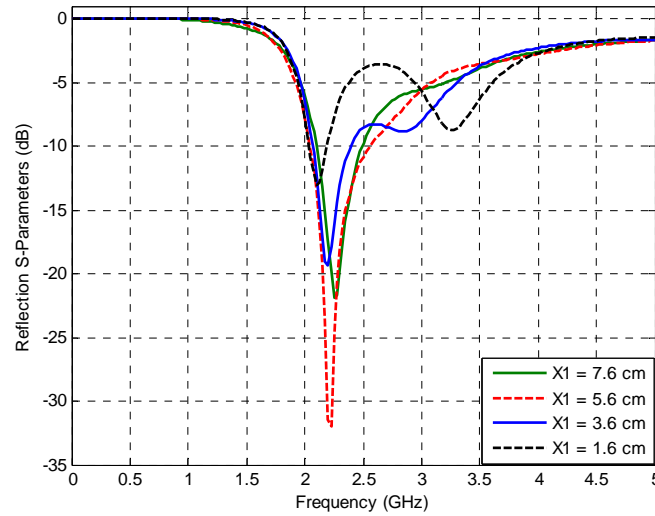


Fig. 5.13 Scattering reflection coefficient of a Monopole antenna mounted on a chassis ($S=0.8$ in Fig. 5.8)

Again, from this figure it can be seen that by changing the chassis size, the feed point impedance of the monopole antenna can be changed. Note that by changing the chassis size, the chassis resonance frequencies as well as the surface current densities and the radiation patterns for characteristic mode resonances will be changed.

Considering the size of $100\text{mm}\times 36\text{mm}$ of the chassis, a dip in the reflection S-parameters in the range of the frequencies from 2.7GHz to 2.9GHz can be seen. Using the Neural Network model in section 5.1.2 we calculate the following resonance frequencies as well as the quality factors for the first three modes of this chassis:

	f_0 (GHZ)	Q_n
1st mode (λ_1)	1.330	2.7
2nd mode (λ_2)	2.894	3.8
3rd mode (λ_3)	4.589	2.1

Table 5.2 The first 3 characteristic mode resonances and their corresponding radiation quality factors for a $100\text{mm}\times 36\text{mm}$ chassis, obtained by Neural Network model

As can be seen from Table 5.2, the dip in S_{11} is due to the second chassis mode which has a resonance at 2984MHz with a high quality factor of $Q_n=3.8$.

Table 5.3 shows the resonance frequencies as well as the quality factors of the resonance frequencies of the $100\text{mm}\times 16\text{mm}$ chassis, using the Neural Network model.

	f_0 (GHZ)	Q_n
1st mode (λ_1)	1.215	3.9
2nd mode (λ_2)	3.214	5.3
3rd mode (λ_3)	4.010	4.2

Table 5.3 The first 3 characteristic mode resonances and their corresponding radiation quality factors for a $100\text{mm}\times 16\text{mm}$ chassis, obtained by Neural Network model

Looking at Table 5.3, the second dip in S_{11} at 3.2GHz for the monopole antenna on a 100mm×16mm chassis shown in Fig 5.13 is identified as due to the excitation of the second chassis mode.

5.2.2 Two monopole antennas on the chassis

The chassis length has also an effect on the mutual coupling between antennas, mounted on it. This influence on the integration of a simple two-antenna array on the chassis has been considered in [67, 68].

In this section, we investigate the mutual coupling of two monopole antennas on a chassis, as shown in Fig 5.14.

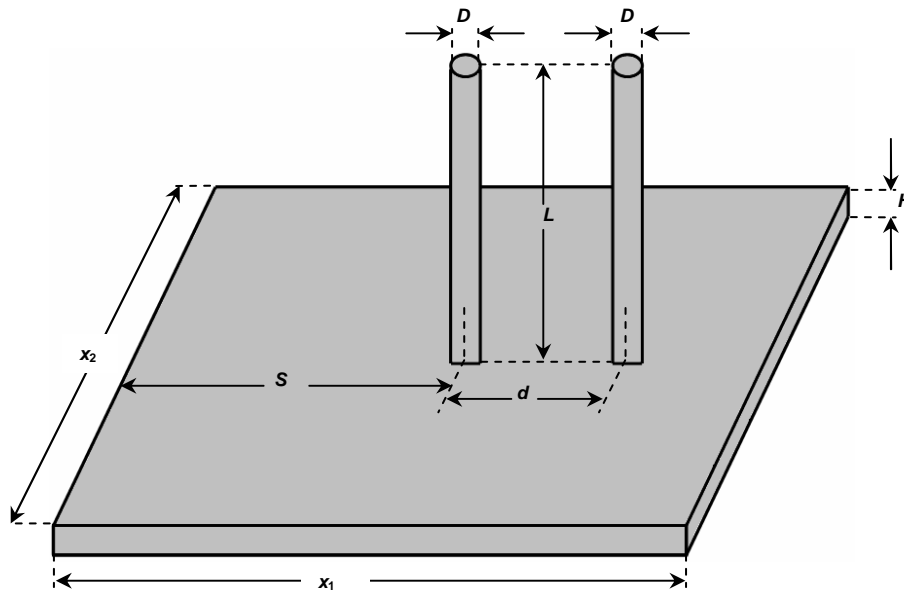


Fig. 5.14 Two monopole antennas mounted on a chassis

First, the chassis and monopole antenna dimensions are considered to have the fix values as: $x_1 = x_2 = 100\text{mm}$, $H = 1\text{mm}$, $L = 31\text{mm}$ and $D = 1\text{mm}$ for both antennas and $d = 3\text{cm}$.

Assume that the array is moved from the centre of the chassis ($S = 3.5\text{cm}$) to the left chassis edge and the variable S (distance between left monopole antenna and chassis edge) is varied. From calculations using the EMPIRE simulator, the transmission S-parameters of the array then can be found as shown in Fig 5.15.

This figure shows that by changing the position of the antennas, the mutual coupling can be changed. The minimum coupling at $f = 2.27\text{GHz}$ (the resonance frequency of the monopole) is obtained by mounting the first antenna in a distance of $S = 0.8\text{cm}$ from the chassis edge.

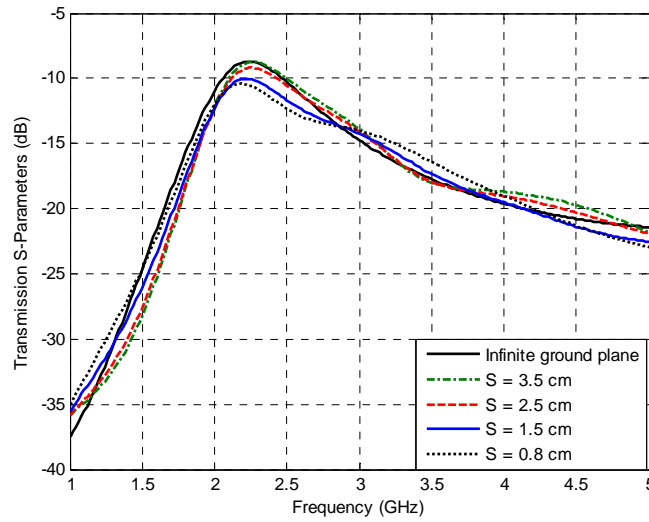


Fig. 5.15 Transmission S-parameters of two monopole antennas mounted on a chassis in different positions and spaced by $d=3\text{cm}$

Now again, the array antenna in Fig 5.14 is fixed at $S = 0.8\text{cm}$ and the chassis length x_2 is considered to be fixed at $x_2 = 100\text{mm}$. The length x_1 is then varied in a wide range (between 5cm and 50cm). If the transmission Scattering parameters of the antennas are simulated at $f = 2.27\text{GHz}$, the variations depicted in Fig 5.16 can be found.

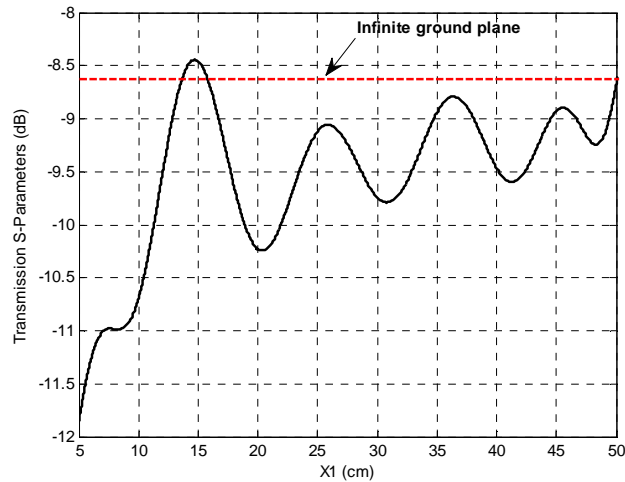


Fig. 5.16 Coupling of two monopole antennas mounted on a chassis edge ($S = 0.8\text{ cm}$)

It can be seen that the mutual coupling between the antennas, varies in a periodic manner, as indicated in [1], because of the excitation of different modes with varying coupling in each length and varying phase relations.

This indicates that the size of the chassis influences the performance of array antennas which therefore should be also considered in the optimization procedure.

5.2.3 MFSAA on the chassis

Finally, to consider the effect of a finite ground plane on the MFSAA fundamental parameters and the necessity of optimizing the ground plane dimensions in our optimization procedure, the MFSAA is considered on a chassis, as shown in Fig 5.17.

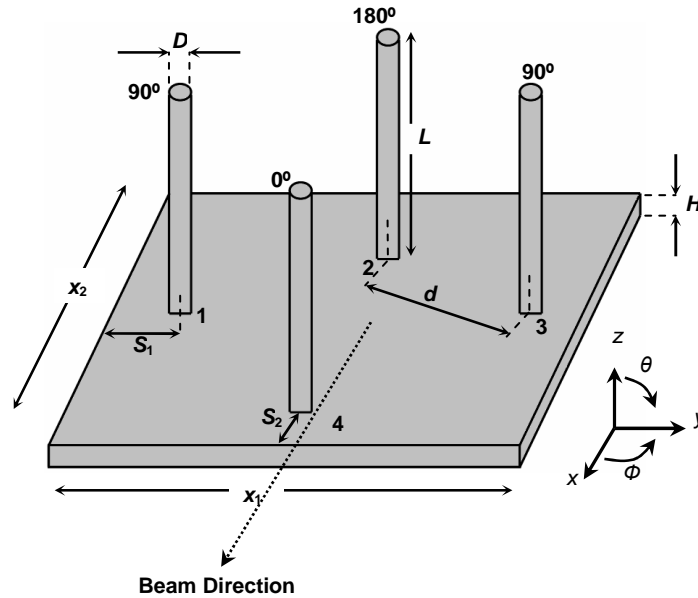


Fig. 5.17 MFSAA mounted on a chassis with phases of source voltages indicated

The MFSAA is fixed at $H = 1\text{mm}$, $L = 31\text{mm}$ and $D = 1\text{mm}$ for all antennas and $d = 5.93\text{cm}$. The source voltages of the feed network are assumed as the voltages in equation (2.38) which allows the monopole currents I_i to vary according to the effects of mutual coupling, as seen in section 2.4. S_1 is the distance between the first monopole antenna and the left chassis edge and between the third monopole antenna and the right chassis edge, while S_2 is the distance both between the fourth monopole antenna and the bottom chassis edge and between the second monopole antenna and the top chassis edge.

First, by fixing both x_2 at $x_2 = 10\text{cm}$ and S_2 at $S_2 = 0.8\text{cm}$, the radiation patterns are simulated for three different chassis length x_1 : $x_1 = 10\text{cm}$ ($S_1 = 0.8\text{cm}$), $x_1 = 12\text{cm}$ ($S_1 = 1.8\text{cm}$) and $x_1 = 14\text{cm}$ ($S_1 = 2.8\text{cm}$). See Fig 5.18.

Then, by fixing both x_1 at $x_1 = 10\text{cm}$ and S_1 at $S_1 = 0.8\text{cm}$, the radiation patterns are found for three different chassis length x_2 : $x_2 = 10\text{cm}$ ($S_2 = 0.8\text{cm}$), $x_2 = 12\text{cm}$ ($S_2 = 1.8\text{cm}$) and $x_2 = 14\text{cm}$ ($S_2 = 2.8\text{cm}$). See Fig 5.19.

The two sets of patterns show major variations due to changes in the dimensions of the chassis. However, identification of the individual chassis modes which are responsible for particular pattern effects is difficult because the patterns represent total field intensities without discrimination of polarization components.

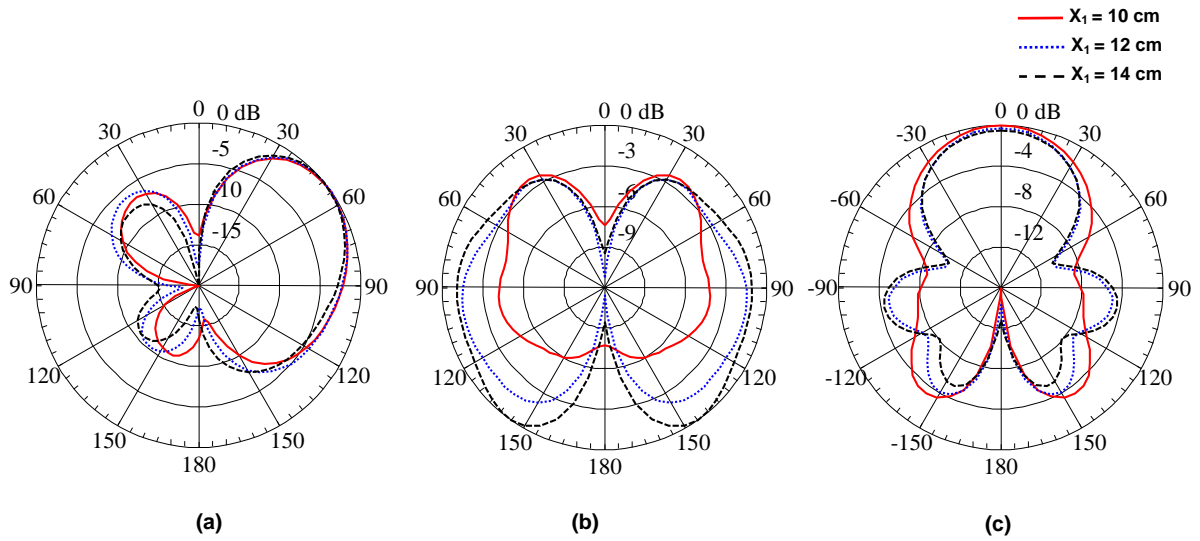


Fig. 5.18 (a): Elevation radiation pattern ($\phi = 0^\circ$), (b): elevation radiation pattern ($\phi = 90^\circ$) and (c): azimuthal radiation pattern ($\theta = 90^\circ$) at 2.27GHz of the MFSAA in Fig 5.17 with $x_2 = 10\text{cm}$ (total fields, patterns normalized to peak gain)

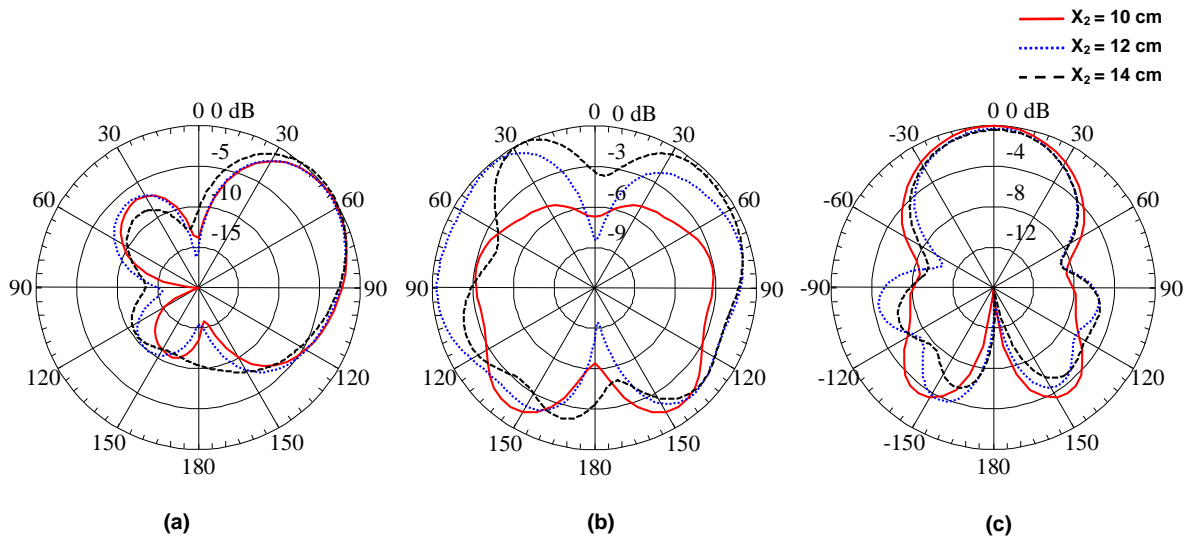


Fig. 5.19 (a): Elevation radiation pattern ($\phi = 0^\circ$), (b): elevation radiation pattern ($\phi = 90^\circ$) and (c): azimuthal radiation pattern ($\theta = 90^\circ$) at 2.27GHz of the MFSAA in Fig 5.17 with $x_1 = 10\text{cm}$ (total fields, patterns normalized to peak gain)

The patterns also represent the result of currents on the monopoles and on the chassis at the same time, and pattern changes may be the result of changes in the monopole currents (due to changing mutual coupling) and/or due to changes in the phase and amplitude of the chassis modes excited.

In order to understand the pattern effects demonstrated in Fig 5.18 and Fig 5.19, it is helpful to realize the coupling of monopole currents and chassis mode currents: The two equal phase currents I_1 and I_3 can couple to the anti-symmetric currents of the 2nd chassis mode, both the x-polarization and the y-polarization current modes; coupling to the symmetric current distributions of 1st and 3rd chassis modes is suppressed due to symmetry relations.

The anti-phase currents I_2 and I_4 couple to the symmetric current distributions of 1st and 3rd chassis modes with x-polarization, while the y-polarized modes are suppressed due to symmetry relations. A higher-order current mode with y-polarization maybe coupled, but this is out of the scope of the present investigation.

The superposition of field from the MFSAA monopole currents and the chassis mode currents can best be analyzed using the elevation patterns. While the pattern cuts with $\phi=0^\circ$ (x-z-plane) show the effects of the x-polarized symmetric and anti-symmetric chassis modes, the pattern cuts with $\phi=90^\circ$ (y-z-plane) show the effects of the symmetric x-polarized and of the anti-symmetric y-polarized chassis mode currents.

In particular, Fig 5.18(a) exhibits a decrease of the first chassis mode (x-polarized) with increasing width x_1 . This mode is characterized by a filling of the null in the x-z-plane and an omni-directional pattern in the y-z-plane.

Fig 5.18(b) gives a y-z-cut which should exhibit symmetric pattern and a null at 0° and 180° (z-axis) for the MFSAA on an infinite ground plane. Instead, for $x_1=10\text{cm}$, we see the null slightly filled due to radiation from the even current distributions of the 1st chassis mode with x-polarization. For $x_1 > 10\text{cm}$, this contribution seems to fade out and the radiation from the anti-symmetric current distribution of the 2nd chassis mode with y-polarization remains which is compliant with the symmetry of the resultant patterns and the deep minima. However, the y-polarized 2nd chassis mode should exhibit a null along the y-axis, which we miss in Fig 5.18 (b) and Fig 5.18 (c). This is a hint to a contribution from the symmetric current distribution of the 3rd chassis mode (y-polarized) which produces radiation in the x-z-plane with anti-phase relative to the radiation from the 1st chassis mode. Fig 5.18 (c) shows the azimuth pattern (x-y-plane) where we observe a strong variation around $\phi = \pm 90^\circ$ (especially for $x_1 > 10\text{cm}$ patterns in comparison to $x_1=10\text{cm}$ pattern) which can be attributed to the variation in the magnitude of the 1st and 3rd chassis modes with y-polarization.

The variation in x_2 , Fig 5.19(a), for large x_2 , shows a major increase in the filling of the pattern null in the upper and lower hemisphere (to about 10dB below peak gain) due to strong excitation of the symmetric current distribution (x-polarization), probably of the 3rd chassis mode.

The asymmetric elevation pattern, Fig 5.19(b) indicates that symmetric and anti-symmetric chassis modes of x- and y-polarization are excited with phase and amplitude depending on the chassis length, i.e., the first, second and third modes. This asymmetric pattern degradation is also seen in the back-lobes in azimuth plane, Fig 5.19 (c).

A comparison of x-z- plane cuts for infinite ground plane, quadratic chassis of $10\text{cm} \times 10\text{cm}$ and rectangular chassis configurations in Fig 5.20 demonstrates the extent of pattern degradation by null-filling due to the chassis mode excitation.

The major variation of radiation in the back-lobe direction ($\theta = 90^\circ$, left) have to be attributed to changes in the monopole currents and the third chassis mode because the other chassis modes exhibit nulls into this direction, see Fig 5.2.

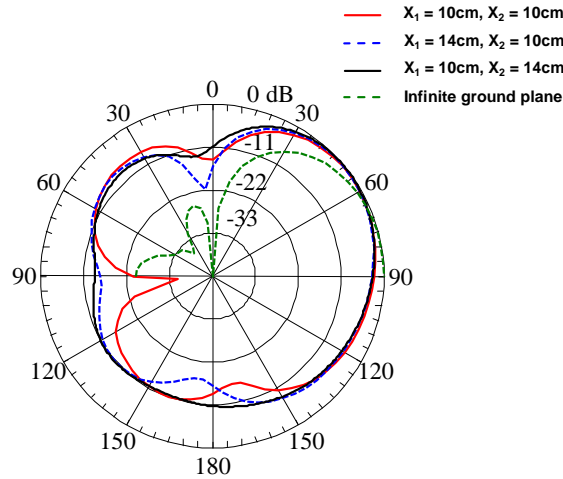


Fig. 5.20 Elevation radiation pattern ($\phi = 0^\circ$) at 2.27GHz of the MFSAA in Fig 5.17.

These results represent another support of the idea of including the dimensions of the chassis as additional parameters in the optimization problem of the MFSAA; as will be presented in the following.

5.3 Performance optimization of the MFSAA on chassis

In this section the chassis dimensions x_1 , x_2 and H as well as the antenna parameters L , D , d and S in Fig 5.17 are considered in the optimization problem and new optimized parameters are found to realize the MFSAA on a chassis. A quadratic chassis is assumed in the following in agreement with the concept of the MFSAA used as a multi-beam array antenna.

5.3.1 Minimize the reflection and coupling scattering coefficients of the antennas

In the following, the question is investigated whether it is possible to reduce the mutual coupling by just increasing the element spacing (within the practical limits of the array) as well as optimizing the chassis size.

For this purpose, it is considered that S is the distance between each antenna and the chassis edge and $x_1 = x_2 = x$ in Fig 5.17. This leads to:

$$S = \frac{x - \sqrt{2}d}{2} \quad (5.8)$$

The chassis length x , now is a dependable variable with monopole distance d .

Variable S is also considered to vary as:

$$S \geq 0.1\text{cm} \quad (5.9)$$

Then the dependable variable x can be varied as:

$$x \geq 0.2\text{cm} + \sqrt{2}d \quad (5.10)$$

The following cost function is only considered for the optimization problem at the monopole center frequency of $f_c=2.27$ GHz in this step:

$$J(x, H, L, D, d) = \text{magnitude}(S_{11}) + \text{magnitude}(S_{21}) + \text{magnitude}(S_{31}) \quad (5.11)$$

where S_{11} is the reflection coefficient of each antenna on a chassis and S_{21} and S_{31} are the transmission S-parameters of neighboring and diagonally opposite antennas respectively.

Because the array separation is the most important factor in mutual coupling between antennas and due to the effect of the chassis on the mutual coupling as seen before, the upper range for the element distance d in equation (4.8) is increased to 0.57λ (far above the compromise corridor in Fig 4.1). Equations (4.11) and (4.12) as well as the following conditions are considered as constraints of our new optimization problem.

$$0.252 \leq d / \lambda \leq 0.57 \quad (5.12)$$

$$0.001 \leq H / \lambda \leq 0.05 \quad (5.13)$$

$$0.4 \leq x / \lambda \leq 1 \quad (5.14)$$

Table 5.4 shows the optimal values of the parameters after optimizing the cost function (5.11) under conditions (4.11), (4-12), (5.10) and (5-12)-(5-14) using the EMPIRE simulator at 2.27 GHz and using the direct search method.

Parameter	d^{op}	L^{op}	D^{op}	x^{op}	H^{op}
Value	0.486λ	0.251λ	0.008λ	0.80λ	0.01λ

Table 5.4 Optimized variables, obtained by optimizing the cost function (5.11) at 2.27 GHz

Using these optimized parameters, the simulated reflection coefficient S_{11} of each monopole antenna at $f_c=2.27$ GHz is shown in Fig 5.21. Simulated transmission S-parameters of the MFSAA using the optimized variables in Table 5.4 are shown in Fig 5.22.

To decrease the coupling between the antennas, the optimization algorithm has increased the antenna separation and the value of $d^{op} = 0.486\lambda$ (64 mm) has been found. This leads to much lower coupling compared to closer spacing case (compare S_{21} of Fig 5.22 to Fig 5.15).

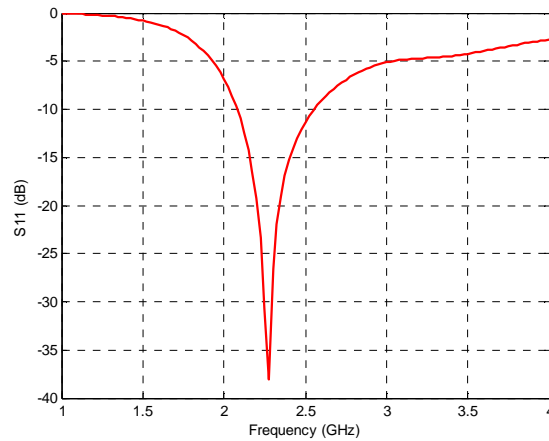


Fig. 5.21 S-parameter S_{11} of the MFSAA mounted on a chassis, using the optimal parameters in Table 5.4

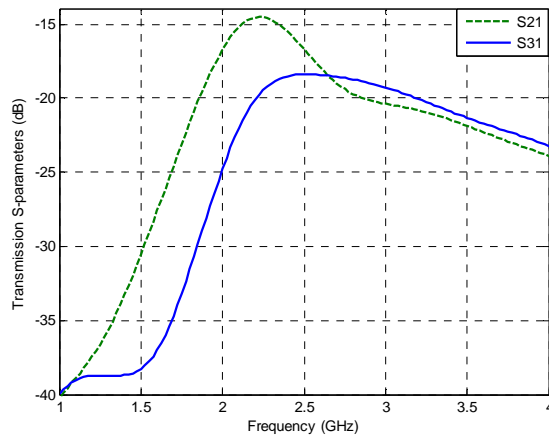


Fig. 5.22 Transmission S-parameters of the MFSAA mounted on a chassis, using the optimal parameters in Table 5.4

The radiation pattern (azimuthal plane, $\theta = 90^\circ$) of this MFSAA, using the optimized parameters in Table 5.4, can be simulated as shown below at 2.27 GHz.

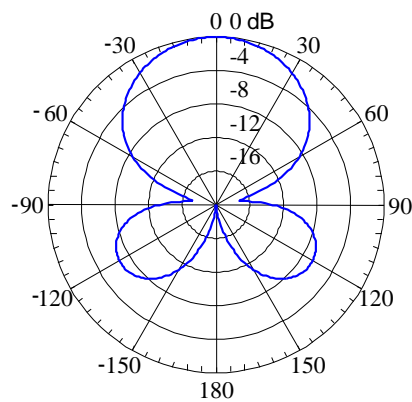


Fig. 5.23 Azimuth radiation pattern ($\theta = 90^\circ$) for the MFSAA on a chassis, using the optimal parameters in Table 5.4 and simulated at 2.27 GHz

The radiation pattern in Fig 5.23 is completely symmetrical. A deep null is created in the radiation pattern and undistorted yet relatively high side lobes can be seen for this pattern.

Any realization of this MFSAA will introduce deviations in the geometrical dimensions (e.g., the wire diameter D may not be available) which may change the optimal values in Table 5.4. Therefore, finding the optimum tolerance region of each parameter in Table 5.4 may help us to realize the MFSAA using parameters close to the optimized values while keeping close to the optimum performance.

5.3.2 Optimum Tolerance Region

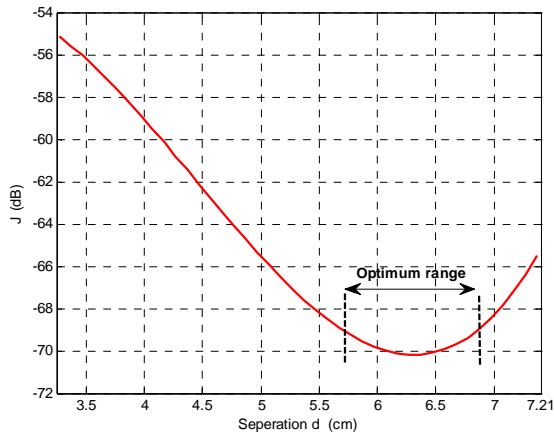
To simulate the optimum tolerance ranges of x , H , L , D and d , the cost function (5.11) is considered to have the optimal values in Table 5.4. By varying each parameter in its range (see equations (4.11), (4.12), (5.10) – (5.12)) the value of the cost function varies as shown in Fig 5.24.

The optimal value of the cost function (5.11) using the optimal values in Table 5.4 is calculated as -70.1dB. The optimum range of each parameter is defined between -70.1 dB and -69dB. Fig 5.24 (b) shows that the chassis thickness H has the widest optimum range (least critical) while the separation d and monopole length L have the smallest tolerance.

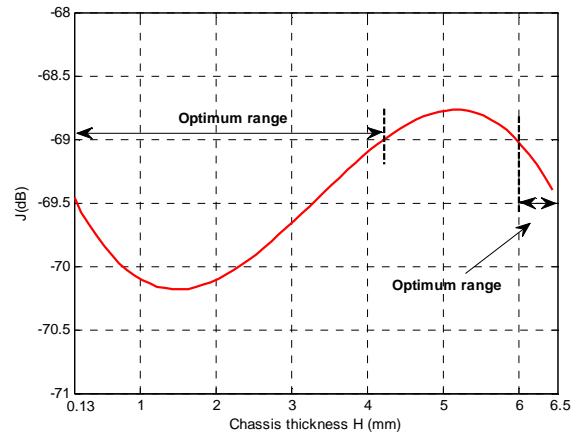
Table 5.5 shows the parameters which are close to the optimized values in Table 5.4 and are in the optimum tolerance range (see Fig 5.24) and which are selected due to practical limitations to fabricate the MFSAA on a chassis.

Parameter	d	L	D	x	H
Value	60mm	32mm	0.9 mm	100mm	1.1mm

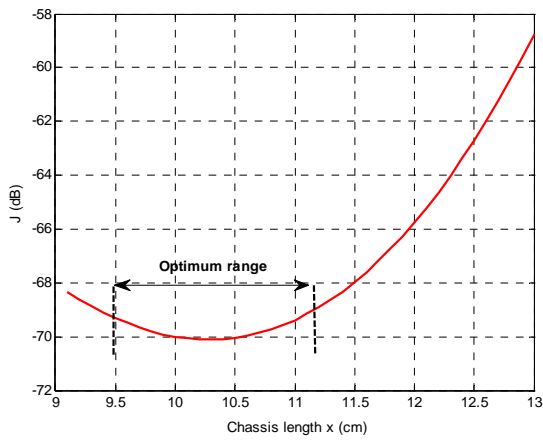
Table 5.5 Parameters close to the optimized values in Table 5.4 chosen to fabricate the MFSAA on a chassis



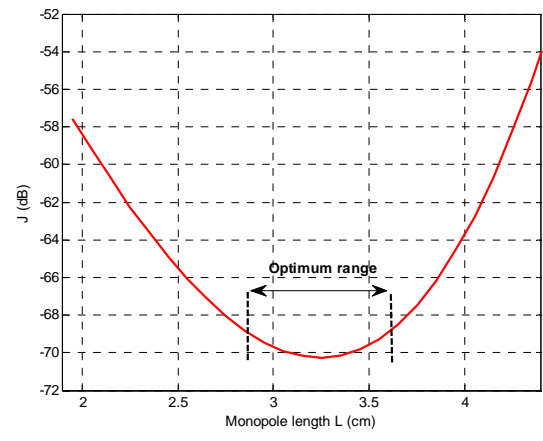
(a)



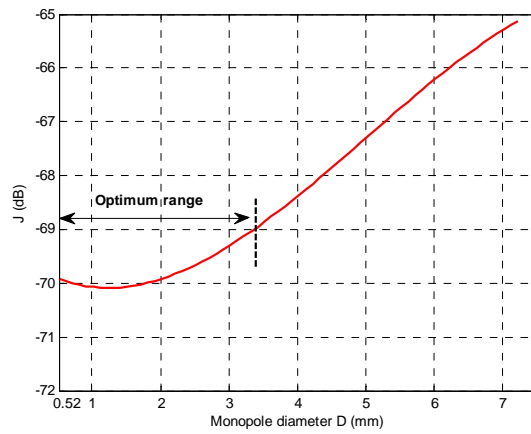
(b)



(c)



(d)



(e)

Fig. 5.24 Optimum tolerance ranges of x , H , L , D and d

5.3.3 Realization of the MFSAA

To check the results obtained in section 5.3.1, the MFSAA on a finite ground plane is fabricated using the parameters shown in Table 5.5 and is measured around $f_c=2.27\text{GHz}$. See Fig 5.25.



Fig. 5.25 Realization of the MFSAA on a chassis using the parameters in Table 5.5

The simulated and measured S-parameters for this MFSAA are shown in Fig 5.26.

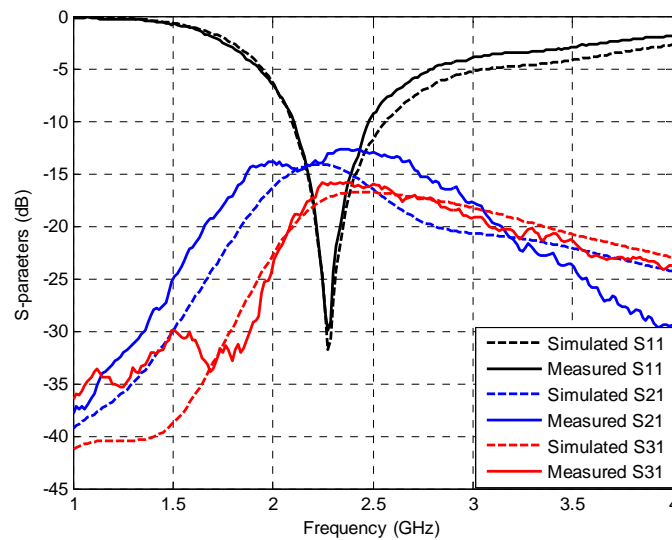


Fig. 5.26 Simulated and Measured S-parameters for the MFSAA on a chassis with parameters in Table 5.5

In Fig 5.26, S_{11} is the reflection S-parameter of each antenna, S_{21} is the transmission S-parameter between neighboring antennas and S_{31} is the transmission S-parameter between diagonally opposite antennas.

Fig 5.26 shows a good agreement between the simulation and measured results at and around the center frequency of $f_c = 2.27$ GHz.

Both S_{21} and S_{31} still exhibit high coupling, the value of S_{21} in simulation is -14 dB whereas in experiment the result is -13.1 dB and S_{31} has a value of -17.6 dB in simulation and -16 dB in experiment.

The difference between the simulated S_{21} and S_{31} in this figure (obtained by the parameters which are close to the optimal parameters) and Fig 5.22 (obtained by the optimal results) is less than 1.5dB and this demonstrates that to reduce the coupling between antennas much better, e.g. below -20 dB, it is not sufficient only to optimize the antenna and chassis parameters. For this purpose, a Decoupling and Matching Network (DMN) is also necessary for the MFSAA on a chassis, which will be presented in section 5.3.5.

With respect to the chassis mode effect, Fig 5.26 shows the same artifact in all three plotted S-parameters above the monopole resonance frequency f_c : S_{11} is lower and S_{21} and S_{31} are higher than in an array on infinite ground plane which can be attributed to coupling with the 2nd and/or 3rd chassis mode at 3.35 GHz.

5.3.4 Realization of the feed network

To measure the far-field radiation pattern for the MFSAA on a chassis, depicted in Fig 5.25, a feed network is needed to generate the excitation phases of 90° , 180° , 90° and 0° with a uniform amplitude for the source voltages of the first, second, third and fourth antenna, as explained in equation (2.38).

Fig 5.27 shows the layout of this network of three cascaded 90° hybrid couplers [69].

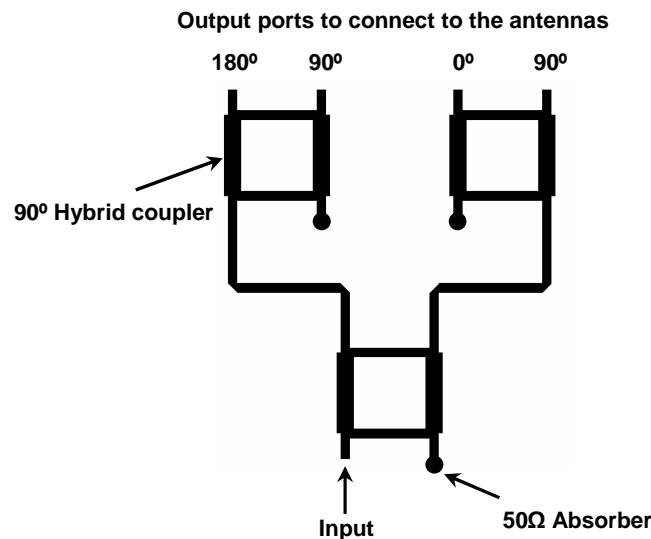


Fig. 5.27 Feed network for the MFSAA

The network was designed for RO3010 substrate with a relative permittivity of 10.2 and a thickness of 1.28 mm using the ADS simulator with its Schematic and Momentum simulation modes. Fig 5.28 shows the schematic design of the hybrid coupler in ADS simulator.

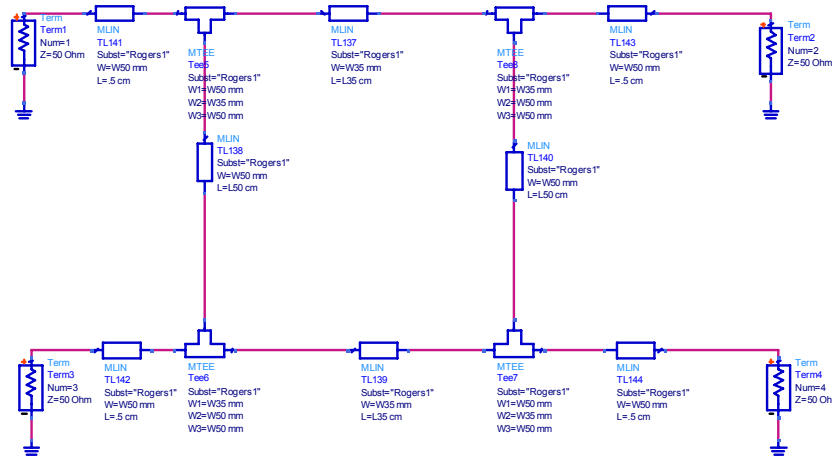


Fig 5.28 Schematic design of Hybrid coupler in ADS simulator

Fig 5.29 shows the simulated S-parameters (ADS Momentum simulation) of the hybrid coupler optimized for 2.27 GHz.

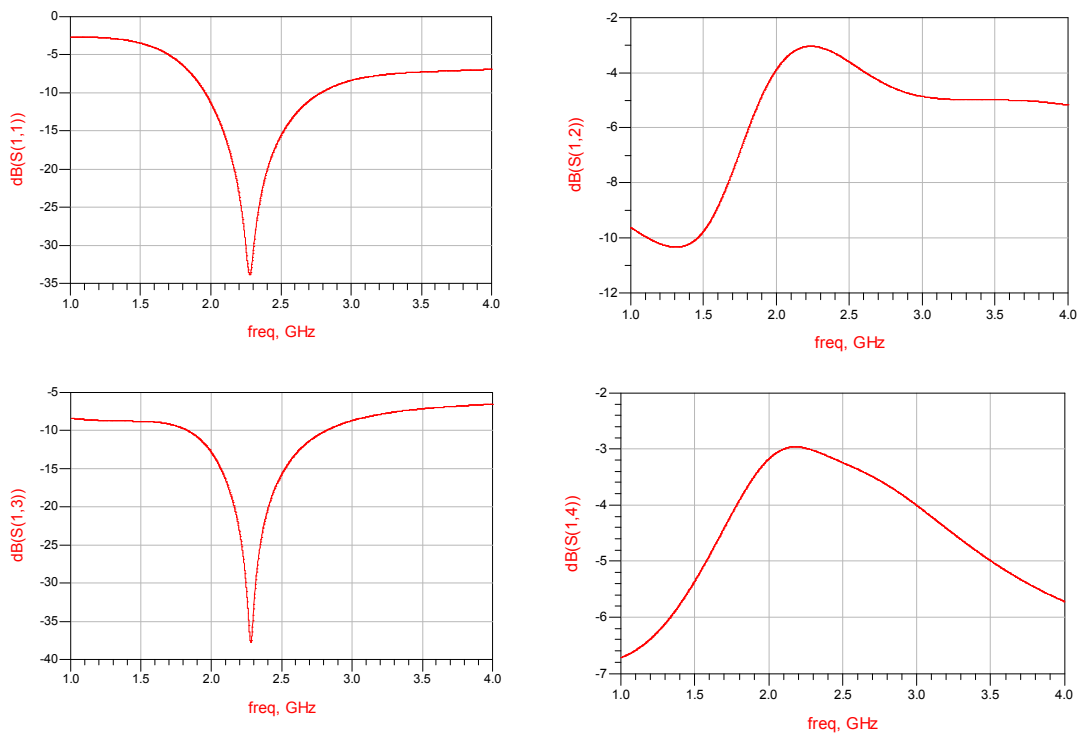


Fig. 5.29 Simulated S-parameters of the hybrid coupler

A phase error of 0.6° between the output ports and an insertion loss of 0.1dB has been found in Momentum simulation for this hybrid coupler.

After designing the hybrid coupler, the network shown in Fig 5.27 was fabricated on a RO3010 substrate as shown below.

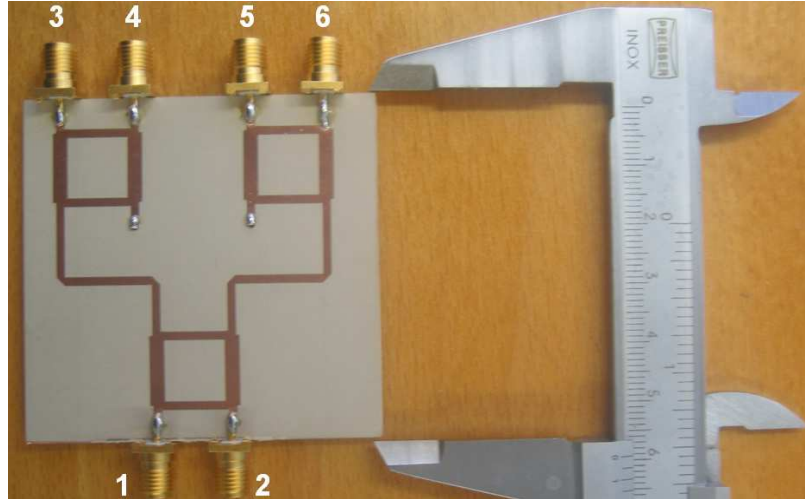


Fig. 5.30 Realization of the feed network

The following S_{11} and S_{21} measurements show acceptable reflection and isolation of this network at the frequency of $f_c = 2.27\text{GHz}$.

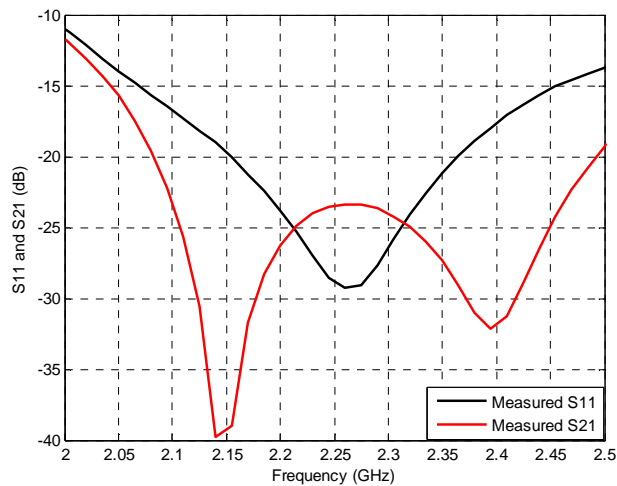


Fig. 5.31 Measured S_{11} (dB) and S_{21} (dB) for the network, shown in Fig 5.30

The transmissions S-parameters of the network have been measured as shown in Fig 5.32.

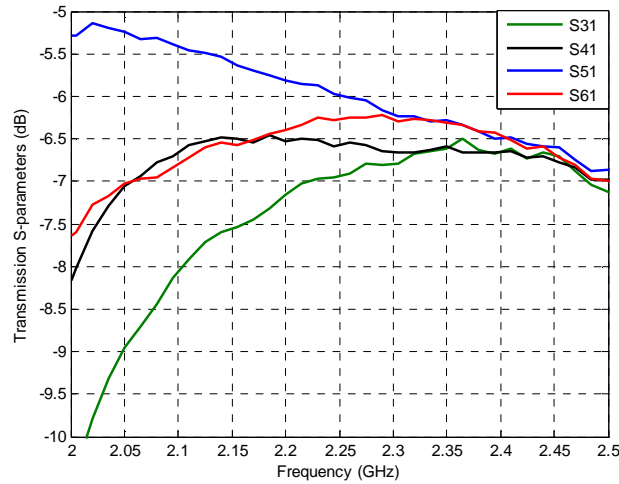


Fig. 5.32 Measured transmission S-parameters (amplitude) for the matrix network, shown in Fig 5.30

An average insertion loss of 0.46 dB is found for this network at $f_c = 2.27\text{GHz}$. Fig 5.33 shows the phases of the transmissions S-parameters of this network. Phase errors of $+2.2^\circ$, 0° , -3.98° and -3° are found for the first, second, third and fourth output ports of the network respectively at $f_c = 2.27\text{GHz}$ which can be assumed small enough in order not to deteriorate the radiation pattern of the MFSAA considerably.

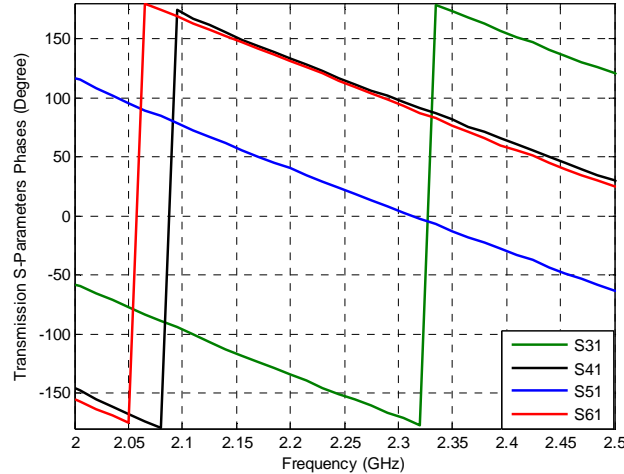


Fig. 5.33 Measured transmission S-parameters (degree) for the matrix network, shown in Fig. 5.30

After connection of the network to the MFSAA, shown in Fig 5.25, the far-field radiation pattern was measured in our anechoic chamber as shown in fig 5.34.

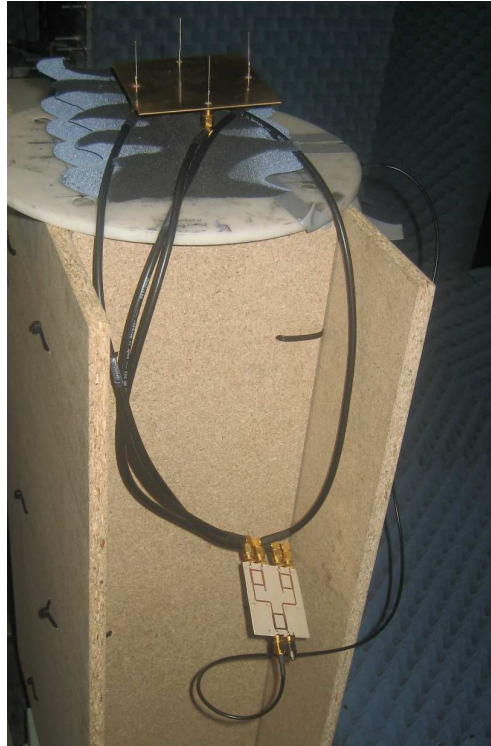


Fig. 5.34 Output ports of the network connected to the MFSAA to measure the far-field radiation pattern

Fig 5.35 shows the simulated and measured far-field azimuth radiation patterns ($\theta=90^\circ$) for the MFSAA with parameters in Table 5.5

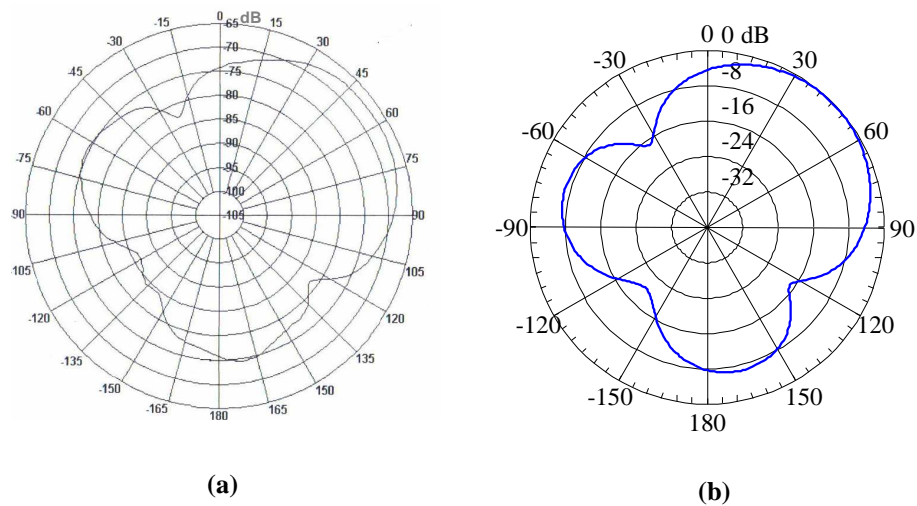


Fig. 5.35 Azimuth radiation pattern ($\theta = 90^\circ$) for the MFSAA, shown in Fig 5.25 at 2.27 GHz with parameters in Table 5.5. (a): measured results, (b): simulated result

A comparison between the simulated and measured radiation pattern above, shows that the calculated and measured results are in good agreement.

The F/B ratio is measured at a level of 6.5dB in Fig 5.35 (a), where the simulation result for the F/B ratio of the MFSAA shows a level of 7dB.

Comparing the radiation patterns in Fig 5.35 (obtained by the parameters which are close to the optimal parameters) and the radiation pattern in Fig 5.23 (obtained by the optimal results) shows no considerable difference between them. This supports the applicability of the optimum ranges which have been found for the parameters shown in Fig 5.24.

As explained before and by looking at the values of S_{21} and S_{31} for the MFSAA on a chassis, to reduce the coupling between antennas, a Decoupling and Matching Network (DMN) is necessary for the MFSAA on a chassis. In the next section a DMN will be designed and used for the MFSAA on a chassis.

5.3.5 Design of a Decoupling and Matching Network (DMN)-idealized

In [70] and [71], a method has been introduced to design an RF decoupling and matching network (DMN) between three-monopole antenna ports and the receiver channels. For that purpose, three ideal monopoles have been considered on an infinite ground plane with lumped reactances between them in order to create a DMN. Based on the \mathbf{Y} matrix of the array without DMN and with DMN, equations have been derived to allow the values of the lumped elements to be calculated. Finally three monopole antennas are realized on a chassis with DMN.

In the following, this approach is extended to the MFSAA in order to design a DMN. In this step, the MFSAA is assumed on an infinite ground plane and the DMN is assumed to be a network of concentrated reactances without consideration of transmission line effects in a practical realization; hence, this design is termed “idealized”.

The optimum network elements are derived using an optimization procedure rather than by analytical methods.

For this purpose, consider the four monopole antennas on an infinite ground plane, as depicted in Fig 2.11(a). To accomplish the RF decoupling and matching network, six lumped capacitors / inductors are connected between adjacent antenna ports as shown in Fig 5.36. It is necessary to use a cyclic symmetric network and to accept certain limitations in the achievable performance from this condition because we are interested in matching / decoupling for all four beam directions of the MFSAA multi-beam antenna which require the complex excitation of the antenna elements to be cyclicly interchangeable without any change in the antenna properties (apart from beam direction).

The decoupling network consists of the components jB_1 (Capacitance C_1 or inductance L_1) between neighbouring antennas and jB_2 (Capacitance C_2 or inductance L_2) between diagonally opposite antennas [72] which leads to four possible combinations of L_1/C_1 and L_2/C_2 components (termed option 1- 4 in simulations below).

Avoiding the crossing of two transmission lines between opposite antennas, a cross-coupler (0dB coupler) [73], as a cascade of two hybrid couplers (with slight modifications on line widths), was assumed between the antenna ports.

Initially ignoring transmission line and cross-coupler effects, the admittance matrix in equation (5.15) describes the DMN.

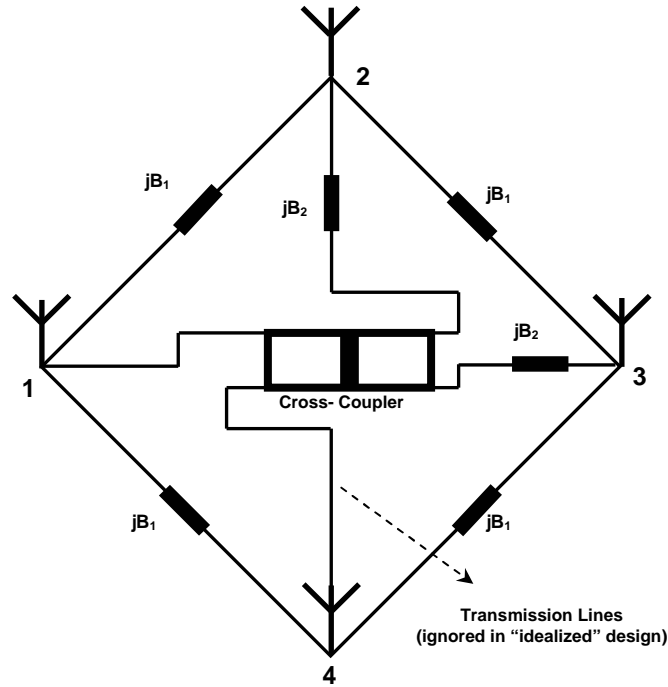


Fig. 5.36 DMN using a cross-coupler for the MFSAA

$$\mathbf{Y} = \begin{bmatrix} 2jB_1 + jB_2 & -jB_1 & -jB_2 & -jB_1 \\ -jB_1 & 2jB_1 + jB_2 & -jB_1 & -jB_2 \\ -jB_2 & -jB_1 & 2jB_1 + jB_2 & -jB_1 \\ -jB_1 & -jB_2 & -jB_1 & 2jB_1 + jB_2 \end{bmatrix} \quad (5.15)$$

The decoupled array admittance matrix \mathbf{Y}^D , then can be expressed in terms of the admittance matrix \mathbf{Y} above and the impedance matrix \mathbf{Z} of the MFSAA without DMN, as below:

$$\mathbf{Y}^D = \begin{bmatrix} Y_{11}^D & Y_{12}^D & Y_{13}^D & Y_{12}^D \\ Y_{12}^D & Y_{11}^D & Y_{12}^D & Y_{13}^D \\ Y_{13}^D & Y_{12}^D & Y_{11}^D & Y_{12}^D \\ Y_{12}^D & Y_{13}^D & Y_{12}^D & Y_{11}^D \end{bmatrix} = \mathbf{Z}^{-1} + \mathbf{Y} \quad (5.16)$$

For decoupling the array, the mutual admittances of the decoupled system (Y_{12}^D and Y_{13}^D) should be zero. Solutions for B_1 and B_2 can be obtained by minimizing the following cost function (real and imaginary parts):

$$J(B_1, B_2, d, L, D) = \text{magnitude}(Y_{12}^D) + \text{magnitude}(Y_{13}^D) \quad (5.17)$$

d is the separation, L is the length of each antenna and D is the diameter of each antenna (Note that impedance matrix \mathbf{Z} is a function of d , L and D as described in sections 2.2.3 and 2.3.1 for self and mutual impedances).

Considering the cost function above with equations (5.12), (4.11), (4.12) and the conditions for all states of B_1 and B_2 in Table 5.6 (at $f_c = 2.27\text{GHz}$), the GA optimizer with generations of 30 individuals each, crossover rate = 0.8 and mutation rate = 0.028 is used to minimize the cost function J in equation (5.17) in MATLAB.

Option	Element B_1	Element B_2	Conditions	
1	Capacitor	Capacitor	$0.0157 \leq B_1 \leq 0.157$	$0.0157 \leq B_2 \leq 0.157$
2	Inductor	Inductor	$-0.013 \leq B_1 \leq -0.0066$	$-0.013 \leq B_2 \leq -0.0066$
3	Capacitor	Inductor	$0.0157 \leq B_1 \leq 0.157$	$-0.013 \leq B_2 \leq -0.0066$
4	Inductor	Capacitor	$-0.013 \leq B_1 \leq -0.0066$	$0.0157 \leq B_2 \leq 0.157$

Table 5.6 Options for choosing B_1 , B_2 and conditions to optimize the cost function (5.17)

Note that all conditions in Table 5.6 are chosen in order to accomplish a range for capacitors and inductors that can be easily realized for $f = 2.27\text{GHz}$. It is also possible to increase the chosen ranges in Table 5.6, if no practical optimal results can be found.

Table 5.7 shows the optimal values of the parameters after optimization as well as the values of Y_{12}^D and Y_{13}^D .

Option	B_1^{op} / S	B_2^{op} / S	d^{op} / λ	L^{op} / λ	D^{op} / λ	Y_{12}^D / S	Y_{13}^D / S
1	0.031	0.022	0.465	0.257	0.046	2.09 - 2.47j	3.22 - 6.61j
2	-0.0071	-0.0098	0.432	0.278	0.009	9.13 + 8.67j	12.32 + 6.17j
3	0.086	-0.011	0.515	0.169	0.003	7.23 - 8.34j	8.12 - 13.82j
4	-0.007	0.092	0.557	0.202	0.006	7.55 + 9.15j	10.12 - 11.42j

Table 5.7 Optimized variables as well as the mutual coupling admittances of the MFSAA with DMN-idealized

S (siemens) or Ω^{-1} is the unit of both B and Y . As Table 5.7 shows, the optimal values for the first option can be selected as the optimal values for lumped elements in DMN. This leads to utilize four 2.17pF capacitors between neighboring monopole antennas and two 1.54 pF capacitors between diagonally opposite monopole antennas ($f_c = 2.27\text{GHz}$).

It can be noted that the DMN reduces the resultant coupling between monopoles but a perfect decoupling seems impossible. This may be due to the limitation from the cyclic symmetric network topology but this was not investigated further.

5.3.6 Design of a DMN-realistic effects

More complete modeling is realized by assuming finite ground plane, transmission lines between antenna terminals and cross-coupler ports including gaps for integration of lumped element susceptances and assuming the cross-coupler, according to the schematic of Fig 5.36.

The concept is to design the complete DMN including the cross-coupler and transmission lines with reactive components as a microstrip circuit in ADS/Momentum and export the geometry file of the microstrip structure on a substrate to the EMPIRE simulator where it is combined with the geometry of the MFSAA.

Consequently, the electro-magnetic field solution from the EMPIRE simulator is based on a complete and realistic model of the antenna. Field distributions and network parameters from this approach can be assumed to be more realistic than results from a combination of EM-field simulation for the monopole array alone with imported network characterization of the DMN since the radiation effects of the network are also included.

In the first step, a cross-coupler, shown in Fig 5.36 was designed. The cross-coupler, also known as 0dB coupler, is an efficient means of crossing two transmission lines with a minimal coupling between them. Fig 5.37 shows a planar implementation of a cross-coupler, made as a cascade of two hybrid couplers.

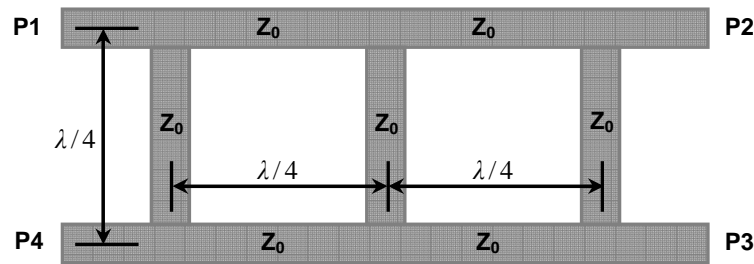


Fig. 5.37 The cross-coupler or 0 dB coupler [73]

The following S-matrix describes this device:

$$\mathbf{S} = \begin{bmatrix} 0 & 0 & j & 0 \\ 0 & 0 & 0 & j \\ j & 0 & 0 & 0 \\ 0 & j & 0 & 0 \end{bmatrix} \quad (5.18)$$

The coupler was modeled and optimized in ADS for a frequency of $f = 2.27\text{GHz}$ and on RO3010 substrate (relative permittivity of 10.2 and a thickness of 1.28 mm). The schematic is shown in Fig 5.38.

The ADS Momentum simulation results in Fig 5.39 show the accuracy of the simulated cross-coupler design.

As can be seen from Fig 5.39, the cross-over coefficient S_{31} is close to 1 (-0.15dB) and the undesired coupling is very low, with S_{12} and S_{14} around -40dB.

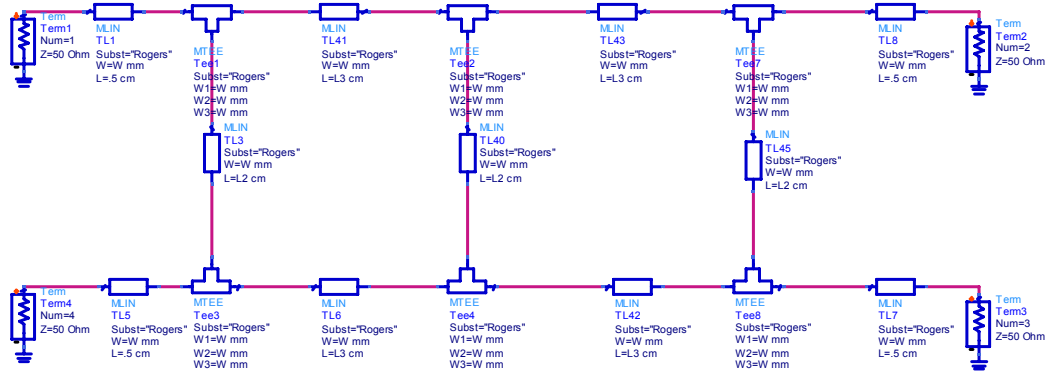


Fig. 5.38 The cross-coupler in ADS simulator (schematic) optimized for $f_c = 2.27\text{GHz}$

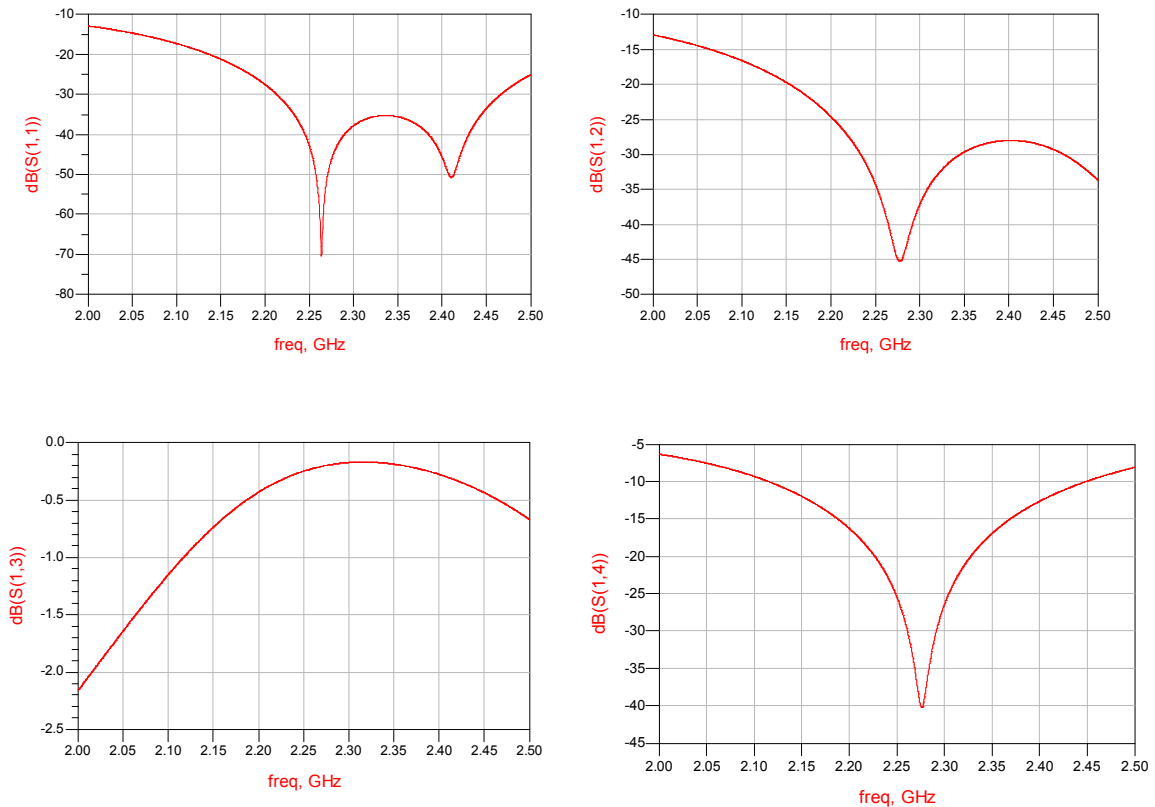


Fig. 5.39 Simulated S-parameters of the cross-coupler, shown in Fig. 5.37

Using the cross-coupler design as above, the complete DMN was created by adding connecting microstrip lines (50Ω lines) between coupler ports and antenna feed points (considering the optimized variables of d and x in Table 5.4), while leaving the values of C_1/L_1 lumped elements between neighboring antennas and C_2/L_2 elements between diagonally opposite antennas as variables for the optimization process.

Contrary to the realization of Fig 5.25, external antenna ports are now created by 50Ω transmission lines leading to the edges of the substrate/chassis where SMA-connectors can be edge mounted, see Fig 5.40. It is also seen that the DMN is not fully symmetric due to the connection of the cross coupler by two different lengths and due to the placement of reactances C_2/L_2 at different distances from antenna elements, see the following figure.

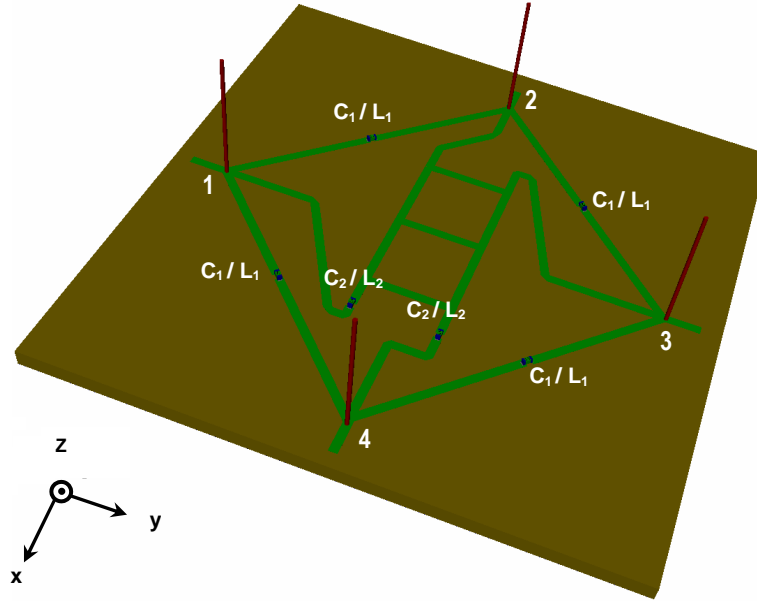


Fig. 5.40 MFSAA with DMN using a cross-coupler for the MFSAA mounted on a chassis (model in EMPIRE simulator)

In the consequent optimization, we aim to find optimum values for the coupling susceptances which achieve the minimum scattering coefficients, while keeping the geometry of the chassis, monopole antennas as given in Table 5.6, and of the DMN unchanged.

Note that the geometry of DMN in Fig 5.40 is based on keeping connecting network on RO3010 substrate as simple as possible. As explained in the “Conclusions and Future Works” chapter, it is also possible to optimize the geometry of DMN by keeping the length and width of the microstrip lines as variables and find the optimum geometry of the transmission lines.

The following cost function is considered for the optimization problem:

$$J(C_1/L_1, C_2/L_2) = \left(\sum_{i=1}^4 \sum_{j=1}^4 \text{magnitude}(S_{ij}) \right) \quad (5.19)$$

where S_{ii} are the reflection coefficients of each antenna and S_{ij} are the transmission S-parameters of neighboring and diagonally opposite antennas.

Table 5.8 shows the optimal values of the capacitors/inductors after optimizing the cost function (5.19).

Option	Between neighboring antennas	Between diagonally opposite antennas
1	$C_1^{op} = 1.5 pF$	$C_2^{op} = 2.5 pF$
2	$L_1^{op} = 5nH$	$L_2^{op} = 8nH$
3	$C_1^{op} = 5.8 pF$	$L_2^{op} = 5nH$
4	$L_1^{op} = 6.3nH$	$C_2^{op} = 3.6 pF$

Table 5.8 Optimized variables as of the MFSAA, depicted in Fig 5.40

The following table shows the reflection coefficients of each monopole antenna, obtained for each option in Table 5.8 at 2.27GHz. The slight asymmetry in the DMN layout mentioned above, results in differences in the scattering parameters, yet at low level.

Option	S ₁₁	S ₂₂	S ₃₃	S ₄₄
1	-25dB	-37dB	-36dB	-45dB
2	-20dB	-18dB	-17dB	-23dB
3	-18dB	-26dB	-19dB	-18dB
4	-15dB	-18dB	-23dB	-20dB

Table 5.9 Reflection S-parameters for the MFSAA, depicted in Fig 5.40 for each option

And the following table shows the transmission S-parameters of the MFSAA, obtained for each option in Table 5.8 at 2.27GHz.

Option	S ₁₂	S ₁₃	S ₁₄	S ₂₃	S ₂₄	S ₃₄
1	-31dB	-35dB	-29dB	-30dB	-36dB	-32dB
2	-26dB	-25dB	-29dB	-25dB	-25dB	-22dB
3	-20dB	-14dB	-19dB	-19dB	-16dB	-17dB
4	-25dB	-17dB	-28dB	-23dB	-18dB	-27dB

Table 5.10 Transmission S-parameters for the MFSAA, depicted in Fig 5.40 for each option

As these tables show, if we select the capacitors between both the neighboring antennas and between diagonally opposite antennas, the coupling between antennas can be compensated considerably with low reflection coefficients of antennas.

Results of optimization show that the chosen topology of the DMN is well suited to decouple the elements of the chosen antenna configuration. Modifications of the layout of the network (e.g., the length of transmission lines could be varied) may improve the matching and decoupling performance further, but this was not investigated. However, in the next step, antenna parameters plus the variables of the DMN are combined in one “Full degree optimization” in order to further improve the solution.

5.3.7 Full degree optimization

The full degree optimization assumes that all parameters of the MFSAA on a finite ground plane except from the edge distance $S = 0.8\text{cm}$ may be varied as well as the coupling elements values of the DMN, with the principal topology of the DMN fixed as shown in Fig 5.40. In order to keep the time consumption for this large optimization problem in practical limits, the behavior of the antenna system was first mapped to a neural network model.

5.3.7.1 Neural Network model for antenna plus DMN

The antenna design now is assumed with the monopole length and diameter allowed to vary, the chassis length and thickness allowed to vary and assuming a DMN as shown in Fig 5.40 suitably connected between the monopole feed points and allowing the concentrated element capacitors/inductors to vary. The only fixed parameters of the antenna system are the monopole edge separation $S = 0.8\text{cm}$ (see Fig 5.17), as used earlier, and the design of the cross-coupler. All variables can vary according to equations (4.11), (4.12), (5.13), (5.14) and Table 5.6. Note that the monopole distance d is a dependable variable with the chassis length as explained in equation (5.8) and the cross-coupler is designed to remain fixed, even when choosing the minimum value of d in equation (5.12).

For the neural network structure, 10 low-level neural modules B_i , 10 knowledge hubs A_i and 2 Multilayer Perceptron (MLP) for high-level neural module C are considered. Six variables: Antenna length L , Antenna diameter D , Chassis length x ($x_1 = x_2 = x$ in Fig 5.17), Chassis height H , neighbouring capacitance/inductance C_1/L_1 and opposite capacitance/inductance C_2/L_2 have been considered as the input vector \mathbf{X} to our model and the output vector \mathbf{Y} is considered to be the decoupled impedance matrix \mathbf{Z}^D , consisting of the self impedance of each monopole antenna as well as the mutual impedances between all antennas with integrated DMN as in Fig 5.40.

Fig 5.41 shows the structure of this neural network. The output and input of the neural network can be expressed as:

$$\mathbf{Z}^D = \begin{pmatrix} Z_{11}^D & Z_{12}^D & Z_{13}^D & Z_{14}^D \\ Z_{12}^D & Z_{22}^D & Z_{23}^D & Z_{24}^D \\ Z_{13}^D & Z_{23}^D & Z_{33}^D & Z_{34}^D \\ Z_{14}^D & Z_{24}^D & Z_{34}^D & Z_{44}^D \end{pmatrix} = f(L, D, x, H, C_1/L_1, C_2/L_2) \quad (5.20)$$

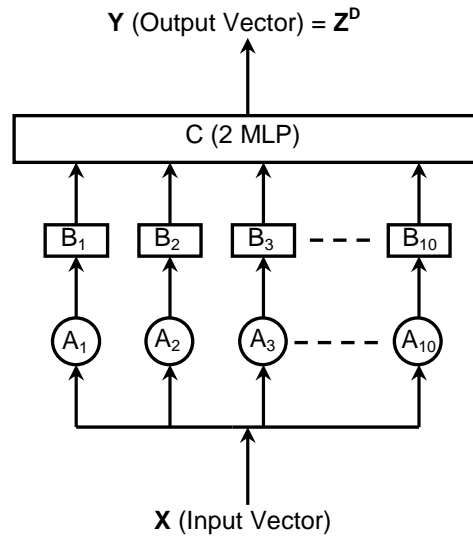


Fig. 5.41 Neural Network structure for antenna with integrated DMN

Based on results calculated using the EM field simulator, 150 random samples have been recorded to both train and test the neural network. 125 data have been used for training the model and 25 data for testing the accuracy of model.

The number of hidden layers and nodes in neural network is then optimized using the method explained in section 3.2.2.

The neural network structure is designed in MATLAB and the variation of “Average Testing Error” for 25 testing data during the training process (with 125 samples) is calculated. Fig 5.42 shows the accuracy of this neural network structure.

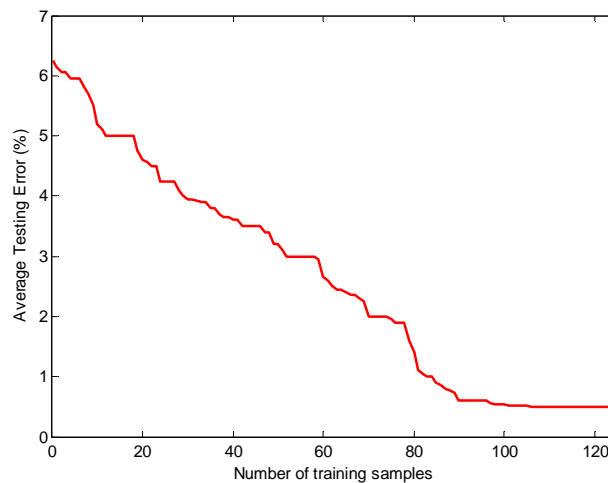


Fig. 5.42 Neural network model accuracy

This figure shows that with training data more than 106, the error remains approximately at 0.5%. This low average error on test data shows that no more training data have to be used to train the network.

Finally, this neural network model is implemented in our optimization problem.

5.3.7.2 Optimization Problem

In this step, the antenna system with integrated DMN is considered as optimization problem. The variables are the same as used in our neural network model, namely antenna length L , antenna diameter D , separation d , chassis dimension x , chassis height H , neighbouring capacitance/inductance C_1/L_1 and opposite capacitance/inductance C_2/L_2 . The monopole edge separation $S = 0.8\text{cm}$ (see Fig 5.17) is assumed fix. Although the monopole distance d is a dependable variable as it scales with the chassis length x (see equation (5.8)), d is still mentioned as a variable in the list of variables of the optimization problem below.

Equations (4.11), (4.12), (5.8), (5.12), (5.13), (5.14) and Table 5.6 are considered as constraints for the optimization problem. The source impedance of the feed network Z_0 is also fixed to 50Ω and the source voltages V_{io} ($i = 1, \dots, 4$) are chosen as equation (2.38).

Now, the excitations I_i ($i = 1, \dots, 4$) at the input terminals of each antenna can be expressed as a function of Z_0 , V_{io} and the impedance matrix \mathbf{Z}^D from the outputs of the neural network model in equation (5.20). Note that the impedance matrix \mathbf{Z}^D includes the effects of the chassis and full DMN to the MFSAA.

The following cost function is considered in our optimization problem:

$$J(L, D, x, d, H, L_1 / C_1, L_2 / C_2) = \frac{\sum_{i=1}^3 W_i J_i^n + W_7 J_7^n}{\sum_{i=4}^6 W_i J_i^n} \quad (5.21)$$

After normalizing each criterion, taken from equations (4.1), (4.2), (4.4), (4.5), (4.6) and (4.7), J_i^n ($i = 1, \dots, 6$) is the normalized value of each criterion, varying between 0 and 1, as described in section 4.2. J_7 is chosen to minimize the load mismatch and the residual mutual coupling and is expressed as below.

$$J_7(L, D, x, d, H, C_1 / L_1, C_2 / L_2) = \sum_{m=1}^4 \sum_{k=1}^4 \text{magnitude}(Z_0 - Z_{kk}^{*D}) + \text{magnitude}(Z_{km}^D) \quad (5.22)$$

J_7^n , the normalized value of J_7 can be obtained by dividing the equation (5.22) by the maximum value of J_7 . In this equation Z_{kk}^{*D} are the complex conjugates of diagonal elements of the matrix \mathbf{Z}^D in equation (5.20) and Z_{km}^D are the off-diagonal elements of \mathbf{Z}^D . The weighting coefficients in equations (4.23) and (4.24) are applied to the cost function (5.21).

Consequently, the cost function (5.21) was minimized using a GA optimizer with generation of 35 individuals each, $P_{\text{Crossover}} = 0.75$ and $P_{\text{Mutation}} = 0.04$ in MATLAB.

Table 5.11 shows the optimization results for the decoupled and matched MFSAA on a chassis.

Parameter	d^{op}	L^{op}	D^{op}	x^{op}	H^{op}	C_1^{op} / L_1^{op}	C_2^{op} / L_2^{op}
Value	0.485λ	0.246λ	0.0091λ	0.81λ	0.02λ	$2.3pF$	$4.8pF$

Table 5.11 Optimized variables for the MFSAA on a chassis with integrated DMN at 2.27GHz

By comparing the results in Table 5.11 and the results in Table 5.4, it can be seen that the antenna system parameters have a small variation in both tables. The optimized antenna length is decreased while the antenna diameter is increased in the full degree optimization procedure. As can be seen from both tables, the chassis dimensions remain almost constant.

On the other hand, the values of capacitors in Table 5.11 are different from the values of capacitors in Table 5.8 (option 1).

Note that for the DMN, again two capacitors have been selected by the optimizer. Considering these optimal values, the impedance matrix \mathbf{Z}^D of the antenna system can be expressed as below.

$$\mathbf{Z}^D = \begin{bmatrix} 54.8 - 5.3j & 4.5 - 6.3j & 9.3 - 4.1j & 4.1 - 9.1j \\ 4.5 - 6.3j & 53.1 + 1.2j & 8.2 - 5.7j & 14.2 - 10.4j \\ 9.3 - 4.1j & 8.2 - 5.7j & 59.6 - 10.2j & 7.3 - 2j \\ 4.1 - 9.1j & 14.2 - 10.4j & 7.3 - 2j & 50.9 - 15.7j \end{bmatrix} \Omega \quad (5.23)$$

As this matrix shows, the self impedance has been better matched to the 50Ω characteristic impedance of the network.

The relative magnitude of the mutual impedances has been reduced in comparison to the equation (4.25). Now, the excitation I_i can be expressed as follows:

$$\begin{bmatrix} I_1 \\ I_2 \\ I_3 \\ I_4 \end{bmatrix} = \begin{bmatrix} 0.75 \angle 90^\circ \\ 1 \angle 175.4^\circ \\ 0.65 \angle 92.6^\circ \\ 0.91 \angle -6.5^\circ \end{bmatrix} \text{ A} \quad (5.24)$$

The 1st and 3rd elements have different excitations and this leads to asymmetric radiation patterns. The 2nd and the 4th antennas have also -4.6° and -6.5° differences in phase with respect to the antennas in the first approximation model in section 4.2 respectively and show different currents magnitudes (also relative to I_1 and I_3). This shows that the overall optimization leads to a DMN which provides a compromise between perfect decoupling of elements (which would lead to the current I_i to be equal in magnitude and have the same phases as the source voltages) and all other goals (costs).

Fig 5.43 shows the azimuth radiation pattern at the elevation beam peak $\theta = 58^\circ$ of the antenna system corresponding to the values in Table 5.11.

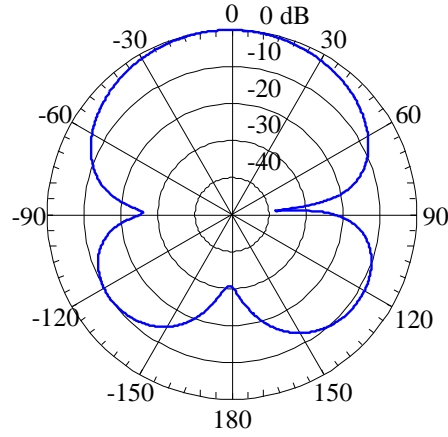


Fig. 5.43 Azimuth radiation pattern ($\theta=58^\circ$) of the antenna system using the optimized parameters in Table 5.11 and simulated at 2.27GHz

As expected, a slightly asymmetric radiation pattern can be seen in this figure. Table 5.12 shows the values of the envelope correlation (ρ), normalized second criterion J_2^n (fit to the secant-squared elevation pattern), beam crossover (BC) level, (F/B) ratio, maximum directivity (D_0), radiation efficiency η_r , mismatch efficiency η_M and maximum absolute gain G_{0abs} , using the optimized parameters in Table 5.11.

Parameter	ρ	J_2^n	BC	F/B	D_0	η_r	η_M	G_{0abs}
Value	0.39	0.24	2.75 dB	8.1 dB	8.72 dB	78%	99%	7.6 dB

Table 5.12 Values of the antenna system using the optimized parameters in Table 5.11

The high values of the mismatch efficiency and gain are due to minimizing the load mismatch. Both values improved comparing with the optimized values in Table 4.5. Note that, by changing the values of the weighting coefficients in equations (4.23) and (4.24) the results in both Tables 5.11 and 5.12 can be changed to be matched to the priorities, defined in the optimization problem.

5.3.7.3 Optimization Problem and symmetric radiation pattern

As can be seen from Fig 5.43, the radiation pattern of the antenna system is asymmetric. To obtain a symmetric radiation pattern, the following constraints are also considered in our optimization problem to achieve amplitude excitations for the 1st and 3rd antennas which are both close to 1A and have only little phase difference:

$$|I_1|, |I_3| \geq 0.9 \text{ A} \quad (5.25)$$

$$(|I_1| - |I_3|) \leq 0.05 \text{ A} \quad (5.26)$$

$$0^\circ \leq \Delta\phi_{I_1, I_3} \leq 10^\circ \quad (5.27)$$

where $\Delta\phi_{I_1, I_3}$ is the phase difference between the excitations I_1 and I_3 .

With these additional conditions, the cost function (5.21) was minimized using the GA optimizer, used before and Table 5.13 shows the optimization results for the decoupled and matched MFSAA on a chassis with symmetric radiation pattern.

Parameter	d^{op}	L^{op}	D^{op}	x^{op}	H^{op}	C_1^{op} / L_1^{op}	C_2^{op} / L_2^{op}
Value	0.457λ	0.218λ	0.025λ	0.77λ	0.02λ	$1.8pF$	$3.1pF$

Table 5.13 Optimized variables results for the decoupled and matched MFSAA on a chassis with symmetric radiation pattern

As this table shows, the uniform antenna length L , separation d and the values of capacitors are decreased in comparison to the Table 5.11, where all other parameters have only small variations.

Considering these optimal values, the impedance matrix \mathbf{Z}^D of the antenna system is expressed as:

$$\mathbf{Z}^D = \begin{bmatrix} 63-9.2j & 1.5-1.3j & 2.3-6.8j & 6.3-12.1j \\ 1.5-1.3j & 71-7.3j & 10-3.2j & 16+13j \\ 2.3-6.8j & 10-3.2j & 60-0.2j & 8-2.5j \\ 6.3-12.1j & 16+13j & 8-2.5j & 57-3.1j \end{bmatrix} \Omega \quad (5.30)$$

As this matrix shows, the self impedance match (to 50Ω characteristic impedance) is degraded and most of the mutual impedances have been improved due to the effects of the new constraints on the optimization procedure.

The excitation I_i is found as:

$$\begin{bmatrix} I_1 \\ I_2 \\ I_3 \\ I_4 \end{bmatrix} = \begin{bmatrix} 0.94\angle 90^\circ \\ 1\angle 184.9^\circ \\ 0.91\angle 82^\circ \\ 0.94\angle -6.5^\circ \end{bmatrix} \text{ A} \quad (5.31)$$

The currents I_1 and I_3 are now more similar which should lead to a more symmetric pattern. Fig 5.44 shows the azimuth radiation pattern at the elevation beam peak $\theta = 58^\circ$ of the antenna system corresponding to the values in Table 5.13: A symmetric pattern with slight asymmetry in the lobe shape and in the level of the back lobes can be seen.

In the antenna designs up to this step, the level of the back lobes has been increased in comparison to the symmetric pattern of the ideal MFSAA on an infinite ground plane in Fig 4.2, mainly due to the large antenna separation d . Note that the excitation I_i has also notable influence on the level of the back lobes (front-to-back ratio). In section 5.3.9, by increasing the weighting coefficient of ‘‘F/B ratio’’ criterion, the optimization process will aim to decrease the level of the back lobes to better suit practical applications.

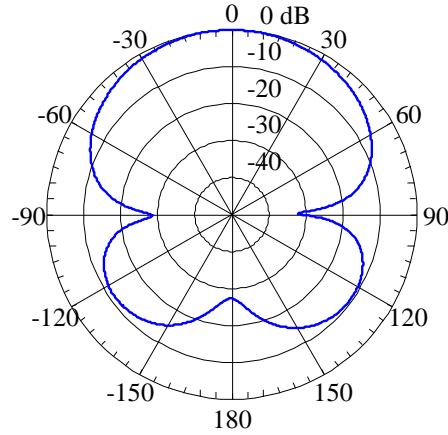


Fig. 5.44 Azimuth radiation pattern ($\theta=58^\circ$) of the antenna system using the optimized parameters in Table 5.13 and simulated at 2.27GHz

Table 5.14 shows the values of the envelope correlation (ρ), normalized second criterion J_2^n (fit to the secant-squared elevation pattern), beam crossover (BC) level, (F/B) ratio, maximum directivity (D_0), radiation efficiency η_r , mismatch efficiency η_M and maximum absolute gain G_{0abs} , using the optimized parameters in Table 5.13.

Parameter	ρ	J_2^n	BC	F/B	D_0	η_r	η_M	G_{0abs}
Value	0.44	0.28	2.68 dB	10.5 dB	8.4 dB	70%	97%	6.7 dB

Table 5.14 Values of the antenna system using the optimized parameters in Table 5.13

The values of mismatch efficiency, directivity and absolute gain in table 5.14 are decreased considerably in comparison to the optimal values in Table 5.12. This shows that to obtain a symmetric radiation pattern a degradation of the values of the optimized parameters has to be accepted.

To realize this MFSAA and, as described in section 5.3.2, finding the optimum tolerance range of each parameter in Table 5.13 can help us to realize the MFSAA using parameters close to the optimized values.

5.3.7.4 Optimum Tolerance Region

To find the optimum tolerance ranges of L , D , x , H , C_1 and C_2 , the cost function (5.21) is considered to have the optimal values in Table 5.13.

By varying each parameter in its allowed range (see equations (4.11), (4.12), (5.8), (5.12)- (5.14) and Table 5.6 (option 1)) the value of the cost function varies as shown in Fig 5.45 at the frequency of 2.27GHz.

The optimal (lowest) value of the cost function (5.21) using the optimal values in Table 5.13 is calculated as 0.15 and the optimum range of each parameter is defined between 0.15 and 0.25.

Fig 5.45 (d) shows that the chassis thickness H has the widest optimum range while the monopole length L has the smallest range (most critical).

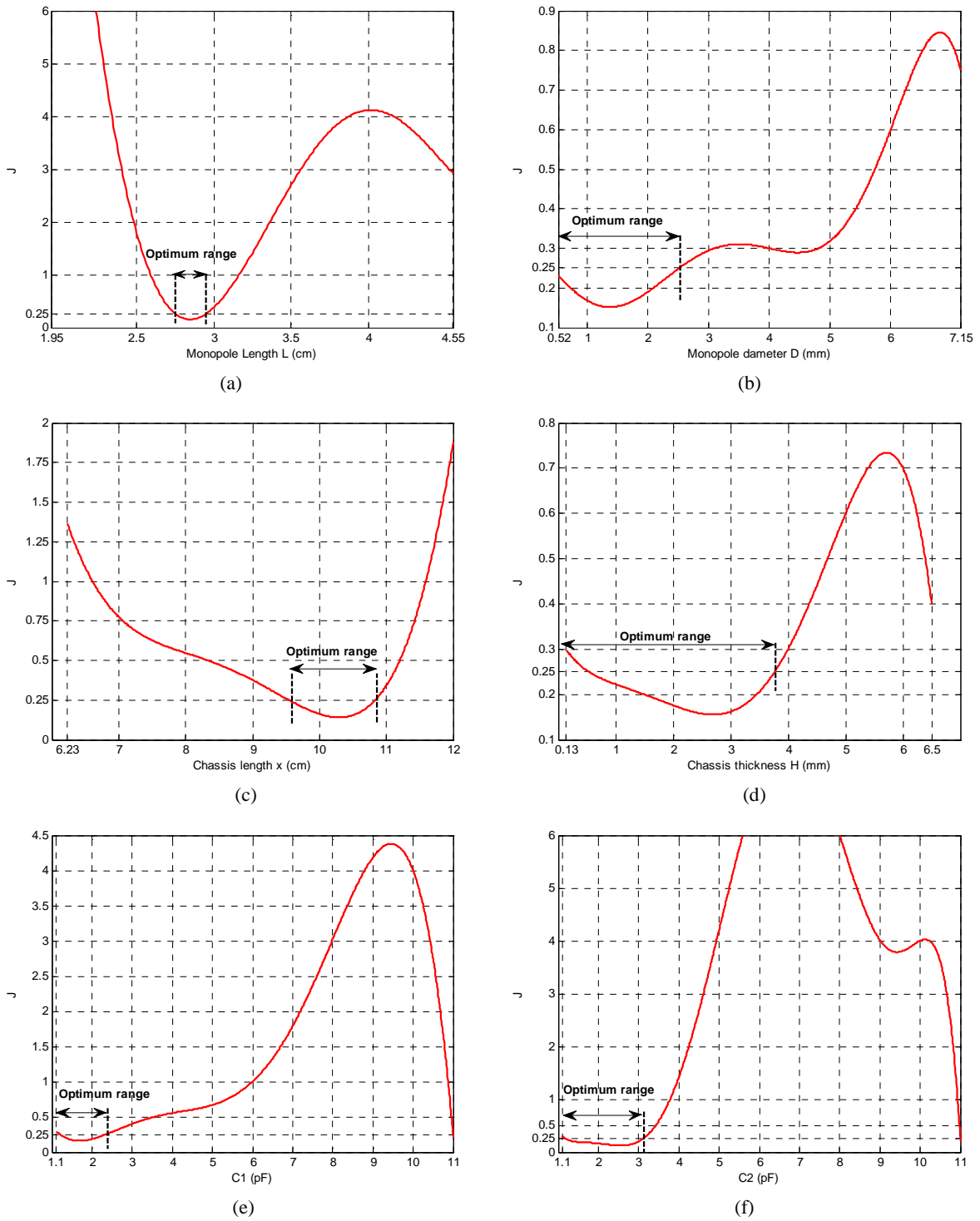


Fig. 5.45 Optimum tolerance ranges of L , D , x , H , C_1 and C_2

Note that since the separation d is a dependable variable of chassis length x , by considering equation (5.12) as the constraint for d and while $S = 0.8$ cm, the chassis length x varies between 6.23cm and 12cm (see equation (5.8)) as can be seen in Fig 5.45(c). Now, by considering both the optimum range of x from Fig 5.45(c) (between 9.55cm and 10.84cm) and equation (5.8), the optimum range of d can be calculated as:

$$5.62\text{cm} \leq d^{op-range} \leq 6.53\text{cm} \quad (5.32)$$

Table 5.15 shows the parameters which are close to the optimized values in Table 5.13 and equation (5.32) and are in the optimum tolerance range (see Fig 5.45), and which are selected due to practical limitations to fabricate the MFSAA on a chassis.

Parameter	d	L	D	x	H	C_1	C_2
Value	58mm	29mm	0.9 mm	98mm	1.1mm	1.5 pF	3.3 pF

Table 5.15 Parameters close to the optimized values in Table 5.13 chosen to fabricate the MFSAA with DMN on a chassis

Next, a realization of this MFSAA with DMN is presented and the results as well as the radiation patterns are compared with the simulation results.

5.3.8 Realization of the optimized MFSAA decoupled and matched

A realization of the MFSAA on a chassis utilizing a DMN using the parameters shown in Table 5.15 is fabricated and is measured at around 2.27 GHz. See Fig 5.46.

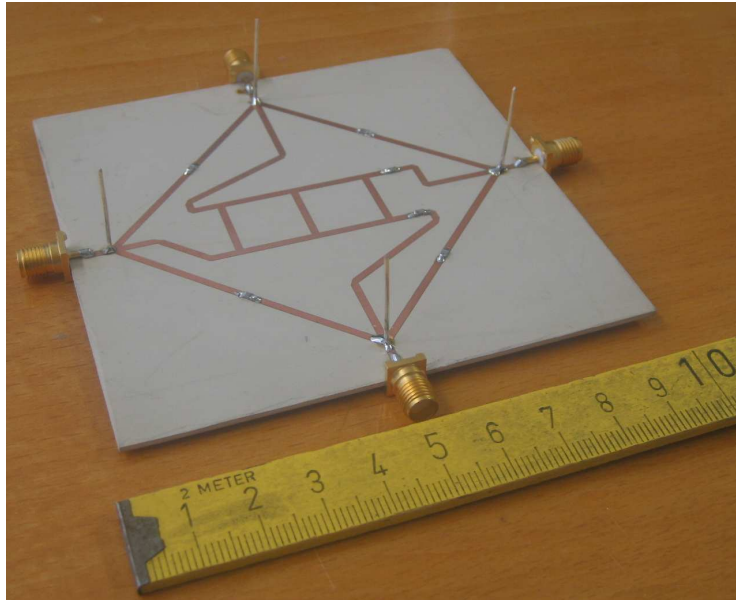


Fig. 5.46 Realization of the MFSAA with DMN using a cross-coupler, with the parameters in Table 5.15

The simulated (using EMPIRE simulator) and measured reflection coefficients S_{11} , S_{22} , S_{33} and S_{44} are shown in Fig 5.47 and the simulated and measured transmission S-parameters are shown in Fig 5.48.

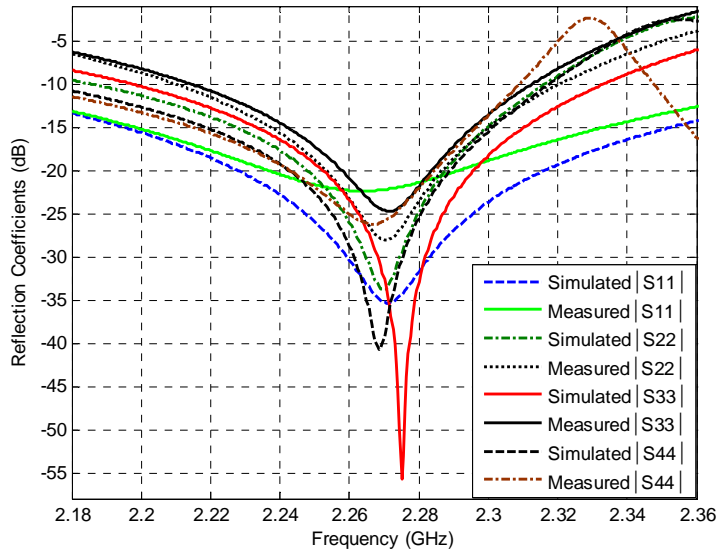


Fig. 5.47 Simulated (Empire simulator) and measured reflection coefficients S_{11} , S_{22} , S_{33} and S_{44} of the MFSAA in Fig 5.46

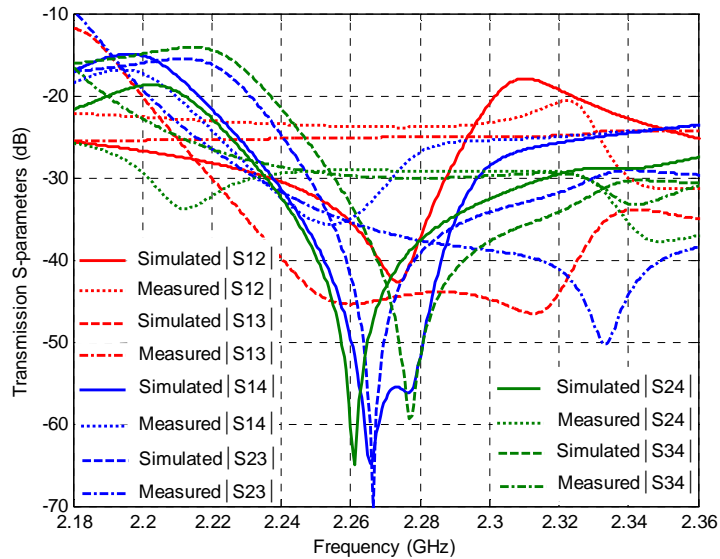


Fig. 5.48 Simulated (Empire simulator) and measured transmission S-parameters of the MFSAA in Fig 5.46

Both figures show a small shift in resonance frequency in simulation results due to using non-optimized parameters close to the optimized values (parameters in Table 5.15).

All measured S-parameters in both figures are in a range below -20 dB which satisfies the motivation to design a DMN for our MFSAA, as indicated in section 5.3.3.

The feed network, shown in Fig 5.30, is now connected to MFSAA with DMN, shown in Fig 5.46 to measure the far-field radiation pattern in our anechoic chamber in the same way as shown in Fig 5.34. The following figure shows the simulated and measured far-field azimuth radiation patterns ($\theta=90^\circ$).

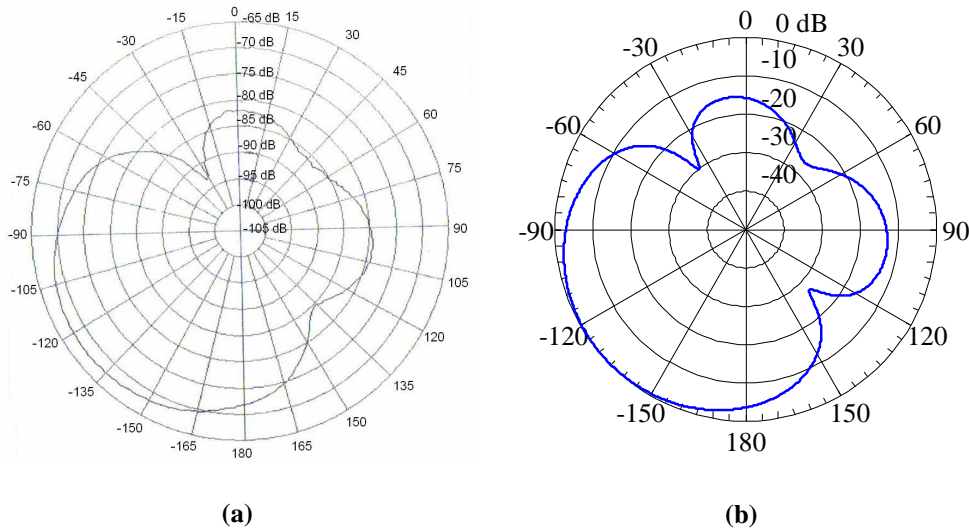


Fig. 5.49 Azimuth radiation pattern ($\theta = 90^\circ$) for the MFSAA with DMN, shown in Fig 5.46 at 2.27 GHz with parameters in Table 5.15. (a): measured results, (b): simulated result

A comparison between the simulated and measured radiation pattern above, shows that the calculated and measured results are in good agreement. The F/B ratio is measured at a level of 11.6 dB in Fig 5.50 (a), where the simulation result for the F/B ratio of the MFSAA shows a level of 12.5dB.

Comparing the front-to-back ratio for the MFSAA with DMN obtained by the parameters which are close to the optimal parameters and obtained by the optimal results in Fig 5.44, shows a better value for the front-to-back ratio for the pattern obtained by the parameters close to the optimized parameters which is due to decreasing the separation d from 59.4 mm to 58 mm.

Such high level of back lobes which leads to a low front-to-back ratio is not suitable in practical applications. Below it is shown how by changing the weighting coefficients of our optimization problem, our priorities are changed to be matched to practical applications.

5.3.9 Changing the weighting coefficients of the optimization problem

Fig 5.44 shows the pattern obtained from the full degree optimization method. This MFSAA design is not suitable for practical applications due to very high level of back lobes.

To improve the front-to-back ratio, it is possible to change the weighting coefficients in equations (4.23) and (4.24) aimed to choose a high value for W_4 (the weighting coefficient of “F/B ratio” criterion). The following weighting coefficients ($\sum W_i = 6$) are now considered in our global optimization problem.

$$W_i = 0.45 \quad i = 1,2,3,5,6,7 \quad (5.33)$$

$$W_4 = 3.3 \quad (5.34)$$

Using these new weighting coefficients, the cost function (5.21) was minimized using equations (4.11), (4.12), (5.8), (5.12), (5.13), (5.14), (5.25), (5.26), (5.27) and Table 5.6 as constraints and the GA optimizer, used before. Note that the cross-coupler is designed to remain fixed, even by choosing the minimum value of d in equation (5.12). Table 5.16 shows the optimization results for the decoupled and matched MFSAA on a chassis with a high weighting coefficient for “F/B ratio” criterion.

Parameter	d^{op}	L^{op}	D^{op}	x^{op}	H^{op}	C_1^{op} / L_1^{op}	C_2^{op} / L_2^{op}
Value	0.262λ	0.252λ	0.034λ	0.79λ	0.035λ	$4.2pF$	$6.7pF$

Table 5.16 Optimized variables for the decoupled and matched MFSAA on a chassis with high value of weighting coefficient for “F/B ratio” criterion

As this table shows, the separation d is decreased considerably and the values of decoupling capacitors between both the neighboring antennas and between diagonally opposite antennas are increased in comparison to the Table 5.13. This can be assumed to be the result of higher mutual coupling at shorter element spacing d .

The uniform length of monopole antennas is also found approximately to be equal to a quarter-wave monopole. All other parameters have only small variations. Considering the optimal values in this table, the impedance matrix \mathbf{Z}^D of the antenna system is expressed by equation (5.35).

$$\mathbf{Z}^D = \begin{bmatrix} 38.5 - 15.1j & 3.2 - 12.1j & 7.1 + 11.3j & 15.2 - 16.7j \\ 3.2 - 12.1j & 78 - 15.2j & 3.2 - 16.4j & 26.7 - 10.1j \\ 7.1 + 11.3j & 3.2 - 16.4j & 37.1 - 4.3j & 14.3 - 16.1j \\ 15.2 - 16.7j & 26.7 - 10.1j & 14.3 - 16.1j & 72 - 11.3j \end{bmatrix} \Omega \quad (5.35)$$

As this matrix shows, the self impedance match (to 50Ω characteristic impedance) is degraded and mutual impedances are increased which is due to reducing the weighting coefficients of the 7th criterion in equation (5.22). The excitation I_i is found as expressed in equation (5.36).

$$\begin{bmatrix} I_1 \\ I_2 \\ I_3 \\ I_4 \end{bmatrix} = \begin{bmatrix} 0.92 \angle 90^\circ \\ 1 \angle 178.6^\circ \\ 0.91 \angle 81.6^\circ \\ 0.74 \angle -19.3^\circ \end{bmatrix} \text{ A} \quad (5.36)$$

The currents I_1 and I_3 have the amplitudes close to 1A and are similar due to inducing conditions (5.25)-(5.27) in our optimization problem.

Fig 5.50 shows the azimuth radiation pattern at the elevation beam peak $\theta = 63^\circ$ of the antenna system corresponding to the values in Table 5.16: A symmetric pattern with slight asymmetry in the lobe shape and in the level of the back lobes can be seen.

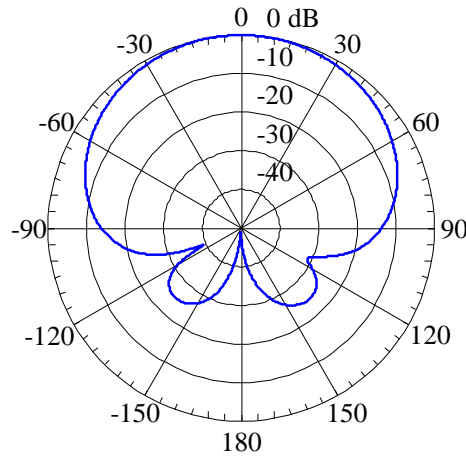


Fig. 5.50 Azimuth radiation pattern ($\theta=63^\circ$) of the antenna system using the optimized parameters in Table 5.16 and simulated at 2.27GHz

The level of the back lobes now is greatly decreased in comparison to the patterns in Fig (5.44) and Fig (5.49).

Table 5.17 shows the values of the envelope correlation (ρ), normalized second criterion J_2^n (fit to the secant-squared elevation pattern), beam crossover (BC) level, (F/B) ratio, maximum directivity (D_0), radiation efficiency η_r , mismatch efficiency η_M and maximum absolute gain G_{0abs} , using the optimized parameters in Table 5.16.

Parameter	ρ	J_2^n	BC	F/B	D_0	η_r	η_M	G_{0abs}
Value	0.53	0.39	2.48 dB	25 dB	6.1 dB	68%	94%	4.2 dB

Table 5.17 Values of the antenna system using the optimized parameters in Table 5.16

(F/B) ratio is the only parameter which is improved in comparison to the optimal values in Table 5.14. This shows that to obtain low level back lobes in the radiation pattern a degradation of all other values has to be accepted. In particular, since this goal can only be achieved with using small element spacing, the beam width has to increase and directivity and gain have to decay.

CHAPTER 6 Conclusions and Future Works

The optimization problem for the Monopole Four Square Array Antenna on a finite ground plane (chassis) using phased excitation has been considered in this thesis.

First, by considering the MFSAA on an infinite ground plane, the optimization problem was defined and the variables were optimized using a Genetic Algorithm method as a global optimizer. Three types of approximation models have been considered for the MFSAA. The performance improvement was achieved by optimizing the geometry and electrical parameters of the MFSAA as well as the feed network parameters.

Next, the MFSAA has been considered on a finite ground plane (chassis). Feed point impedance and mutual coupling of monopole array elements on a chassis have been found to depend critically on the ground plane size and the position of antenna elements. This is due to the excitation of the current modes of the chassis (chassis modes or characteristic modes), which act like additional radiator elements parasitically coupled to the array elements.

The theory of characteristic modes was introduced and the effect of the excitation of chassis modes has been discussed in this thesis. An Artificial Neural Network (ANN) was designed to model the chassis modes by calculating the eigenvalues of a chassis with arbitrary dimensions.

The performance optimization of the MFSAA on a chassis has been defined and optimization has been performed. In order to tackle the remaining problem of mutual coupling, a decoupling and matching network (DMN) for the MFSAA mounted on a chassis was designed and realized to minimize the combined coupling between the antennas and also between chassis and antennas.

Finally, a full degree optimization problem was defined and another Neural Network model, based on extensive EM-field simulations, as well as the Genetic algorithm optimizer was used in the optimization procedure. To check the simulation results, the MFSAA with DMN on a finite ground plane was fabricated and parameters were measured.

Viability of the optimization method was tested by introducing new requirements in every step and a final test was made by requiring the full degree optimization to yield a design for an antenna that provides high F/B ratio as a prime requirement (highest weight).

The simulation time for each optimization was between 8-12 hours. The optimization time depends mainly on choosing the fundamental (initial) parameters of the optimization method.

For future work, the geometry of the DMN, used in this thesis can also be minimized by keeping the length and width of the microstrip lines as variables and find the optimum geometry of the transmission lines.

Further, as shown in [5, 6], the chassis can be interpreted as an antenna structure which can support resonant current distributions, similar to a shorted wire dipole antenna. On the other hand the behavior of both dipole and monopole antennas can be described by an equivalent RLC-circuit model (e.g. [6, 74]).

Now, the theory of characteristic modes of the chassis can be employed to design a network model for the MFSAA mounted on a chassis which represents the monopole and the chassis-modes as resonant circuits which are coupled. Such a network (matrix) representation could help in understanding the various coupling processes and explain the contributions to the array radiation patterns.

References

- [1] K. Solbach, C.T. Famide, “Mutual Coupling and Chassis-Mode Coupling in Small Phased Array on Small Ground Plane”, EUCAP 2007, Edinburgh, Scotland
- [2] R. F. Harrington and J. R. Mautz, “Theory of Characteristic Modes for Conducting Bodies,” IEEE Trans. Antennas Propagation, Vol. ap-19, pp. 622-628, September 1971
- [3] R.J. Garbacz, R.H. Turpin, “A Generalized expansion for Radiated and Scattered Field”, “IEEE Transaction on Antennas & Propagation, Vol. ap-19, pp. 348-358, May 1971
- [4] M. Cabebo et al, “The Theory of Characteristic Modes Revised: A Contribution to the Design of Antennas for Modern Applications”, IEEE Antennas and propagation Magazine, Vol. 49, Nr. 5, Oct 2007
- [5] U. Bulus, K. Solbach, “Modeling of the Monopole Interaction with a small Chassis”, EUCAP 2009, Berlin, Germany
- [6] U. Bulus, C.T. Famdie, K. Solbach. “Equivalent-circuit modeling of the chassis radiator, The German Microwave Conference GeMiC 2009, Munich, Germany
- [7] W.L. Stutzman, G.A Thiele. *Antenna Theory and Design*, 2nd Edition, Wiley, New York, 1998
- [8] M. M. Weiner, *Monopole Antennas*, CRC Press, USA, 2003
- [9] C.A. Balanis, *Antenna Theory: Analysis and Design*, 3rd Edition, John Wiley and Sons, 2005
- [10] Guan, N, H. Furuya, D. Delaune, and K. Ito, “Radiation efficiency of monopole antenna made of a transparent conductive”, Proc. 2007 IEEE AP-S Int. Symp, Hawaii, USA, Jun. 2007
- [11] K. Solbach, S. Angenendt, “Four-square array for multi-beam applications using novel matrix feed”, EuMC2007, Munich, Germany
- [12] Y. T. Lo et al, “Optimization of directivity and signal to noise ratio of an arbitrary antenna array,” Proc. IEEE, Vol. 54, pp. 1033-1045, August 1966
- [13] O. Einarsson, “Optimization of planar arrays,” IEEE Trans. Antennas Propagation, vol. AP-27, Nr. 1, pp. 86–92, Jan. 1979
- [14] D. A. McNamara, “Excitations providing maximum directivity for difference arrays of discrete elements,” Electron. Lett., vol. 23, Nr. 15, pp. 780–781, Jul. 1987
- [15] R.G. Vaughan and J. Bach Andersen, “Antenna Diversity in Mobile Communications”, IEEE Trans. Veh. Tech., vol. 36, 1987, pp 149-172

-
- [16] W. C. Jake, *Microwave Mobile Communications*, New York: IEEE Press, 1994
- [17] M. Krairiksh, "A Flat Four-Beam Compact Phased Array Antenna", IEEE Microwave and wireless components letters, Vol. 12, Nr. 5, MAY 2002, pp.184-186
- [18] T. J. Cho et al, "Front-to-Back Ratio Improvement of a Microstrip Patch antenna by Ground Plane Edge Shaping", Antennas and Propagation Society International Symposium (APSURSI), 2010 IEEE
- [19] H.M. Lee et al, "Front-to-Back Ratio Improvement of a Microstrip Patch Antenna using an Isolated Soft Surface Structure", Microwave Conference, 2009. EuMC 2009, Rome, Italy
- [20] H. Nakano, "Improvement in Front-to-Back Ratio of a Bifilar Backfire Helix by a Flared Open End", IEEE Transaction on Antennas and propagation, Vol. 41, pp. 1591-1595, Nov. 1993
- [21] W. White, "Pattern limitations in multiple-beam antennas", IEEE Transaction on Antennas and propagation, Vol. 10, pp. 430-436, July 1962
- [22] J. D. Kraus, R. J. Marhefka, *Antennas for All Applications*, 3rd Edition, Mc Graw Hill, 2002
- [23] R. Ronald, *Optimization in operations research*, Prentice Hall, 1997
- [24] A.Govan, Introduction to optimization, North Carolina State University, SAMSI NDHS, Undergraduate workshop, 2006
- [25] E, Hall, Optimization with the Genetic Algorithm/Direct Search Toolbox, Research Computing Support Center, University of Virginia
- [26] R. Hooke et al, "Direct search solution of numerical and statistical problems", Journal of the Association for Computing Machinery, 8 (1961), pp. 212-229
- [27] M. Bartholomew–Biggs, *Nonlinear Optimization with Engineering Applications*, chapter 5, Springer Science, 2008
- [28] D.E. Goldberg, *Genetic Algorithms in Search, Optimization, and Machine Learning*, Addison-Wesley Publishing Company, Inc., 1989
- [29] K. F. Man, K. S. Tang, and S. Kwong, *Genetic Algorithms: concepts and designs*, Berlin: Springer, 1999
- [30] *Genetic Algorithm Toolbox*, user's guide for use in MATLAB[®]
- [31] Y.H. Lee, et al, "Genetic algorithm using real parameters for array antenna design optimization", High Frequency Postgraduate Student Colloquium, 1999, Leeds, UK, pp. 8-13
-

- [32] E. Michielssen, J. M. Sajer, S. Ranjithan, and R. Mittra, "Design of lightweight, broad-band microwave absorbers using genetic algorithms", *IEEE Trans. Microwave Theory Tech.*, vol. 41, pp. 1024-1030, June/July 1993
- [33] R. L. Haupt, "Thinned arrays using genetic algorithms", *IEEE Trans. Antennas Propagation*, vol. 42, pp. 993-999, July 1994
- [34] R. L. Haupt, "Comparison between genetic and gradient-based optimization algorithms for solving electromagnetics problems", *IEEE Trans. Mag.*, vol. 31, pp. 1932-1935, May 1995
- [35] D. Marcano, F. Duran, and D. Chang, "Synthesis of multiple beam linear antenna arrays using genetic algorithms", in *IEEE Antennas Propagat. Soc. Int. Symp. Proc.*, Newport Beach, CA, June 1995, vol. 2, pp. 938-941
- [36] A. Boag, E. Michielssen, and R. Mittra, "Design of electrically loaded wire antennas using genetic algorithms", *IEEE Trans. Antennas Propagat.*, vol. 44, pp. 687-695, May 1996
- [37] D. S. Linden, E. E. Altshuler, "Automating wire antenna design using genetic algorithms", *Microwave J.*, vol. 39, no. 3, pp. 74-86, Mar. 1996
- [38] K. Gurney, *An Introduction to Neural Networks*, Routledge, 1997
- [39] Ch. Stergiou, What is a neural network?, http://www.doc.ic.ac.uk/~nd/surprise_96/journal/vol1/cs11/article1.html
- [40] Ch. Stergiou, Neural Networks, the Human Brain and Learning, http://www.doc.ic.ac.uk/~nd/surprise_96/journal/vol2/cs11/article2.html
- [41] J. Heaton, *Introduction to Neural Networks with Java*, Mary McKinnis, 2005
- [42] Y. LeCun, J. S. Denker, and S. A. Solla, "Optimal brain damage," *Advances in Neural Information Processing Systems*, vol. 2, pp. 598-605, San Mateo, CA: Morgan Kaufmann, 1990
- [43] B. Hassabi, D. G. Stork, "Second order derivatives for network pruning: optimal brain surgeon," *Advances in Neural Information Processing Systems*, vol. 5, pp. 164-171, 1993
- [44] S. B. Chung, "A New Pruning Algorithm for Structural Optimization of Neural Networks", Masters Thesis, Department of Electrical Engineering, KAIST, Taejon, Korea, 1998
- [45] S. Xiao, et al, "Wideband Mobile Antenna Design Based on Artificial Neural Network Models", *International Journal of RF and Microwave Computer-Aided Engineering*, vol 13, Issue 4, MAY 2003, pp. 316-320
-

-
- [46] E. R. Brinholo, et al, "Determination of Resonant Frequencies of Triangular and Rectangular Microstrip Antennas, Using Artificial Neural Networks", Progress In Electromagnetics Research Symposium 2005, Hangzhou, China, August 22-26 , pp. 579-582
- [47] N. Türker, et al, "Artificial Neural Networks Applied to the Design of Microstrip Antennas", Microwave Review, June 2006, pp. 10-14
- [48] P. Šmíd, Z. Raida, "Application of Neural Networks: Enhancing Efficiency of Microwave Design", Microwave Review, June 2006. pp. 2-9
- [49] D. K. Neog, et al, "Design of Wideband Microstrip Antenna and the use of Artificial Neural Networks in Parameter Calculation", IEEE Antennas and Propagation Magazine, vol. 47, No.3, June 2005, pp.60-65
- [50] A. Patnaik, et al, "Applications of Neural Networks in Wireless Communication", IEEE Antennas and Propagation Magazine, vol. 46, No. 3, June 2004, pp. 130-137
- [51] A. Patnaik, et al, "An Artificial Neural Network Model for Effective Dielectric Constant of Microstrip Line", IEEE Transactions on Antennas and Propagation, vol. 45, No. 11, November 1997, pp. 1697
- [52] R. K. Mishra, A. Patnaik, "Neural Network-Based CAD Model for the Design of Square Patch Antennas", IEEE Transactions on Antennas and Propagation, vol. 46, No. 12, December 1998, pp. 1890-1891
- [53] R. K. Mishra, A. Patnaik, "Nerospectral Computation for Complex Resonant Frequency of Microstrip Resonators", IEEE Microwave and Guided Wave Letters, vol. 9, No. 9, September 1999, pp 351-353
- [54] A. Patnaik, R. K. Mishra, "ANN Techniques in Microwave Engineering", IEEE Microwave Magazine, March 2003, pp. 55-60
- [55] Q.J. Zhang, K.C. Gupta, *Neural Networks for RF and Microwave Design*, Artech House, Inc, 2000
- [56] R.C. Hansen, *Phased Array Antennas*. Wiley, New York, 1998
- [57] P. Yazdanbakhsh, K. Solbach, "Performance Optimization of Monopole Four-Square Array Antenna using the method of Genetic Algorithm ", EUCAP 2007, Edinburgh
- [58] R. F. Harrington, J. R. Mautz, "Computation of Characteristic Modes for Conducting Bodies", IEEE Transactions on Antennas and Propagation, AP-19, September 1971, pp. 629-639
- [59] M. C. Fabrés, "Systematic Design of Antennas Using the Theory of Characteristic Modes", Ph.D. dissertation, February 2007, Universidad Politécnic de Valencia
-

-
- [60] R. F. Harrington, *Field computation by Moment Methods*, New York, MacMillan, 1968
- [61] Z. Bai, et al, *Templates for the Solution of Algebraic Eigenvalue Problems, A Practical Guide*, Philadelphia, SIAM (Society for Industrial and Applied Mathematics), 2000
- [62] C.T. Famdie, Private Communication-Table of Chassis Mode Eigenvalues, 2007
- [63] C.T. Famdie, "Small Antennas Radiation Performance Optimization in Mobile Communications", Doctoral dissertation, October 2007, Universität Duisburg-Essen
- [64] D. Manteuffel, "Analyse und Synthese von integrierten Antennen für Mobiltelefone unter besonderer Berücksichtigung des Benutzereinflusses", Doctoral dissertation, 2002, Universität Duisburg-Essen
- [65] D. Manteuffel, et al, "Design considerations for integrated mobile phone antennas", ICAP-International Conference on Antennas and Propagation, pp. 252-256, Manchester, 2001
- [66] Sh. M. Ali, H. Gu, "Chassis Wavemode Effects on Hearing Aid Compatibility at 900 MHz", Antennas and Propagation Society International Symposium (APSURSI), 2010 IEEE, Toronto, Canada
- [67] D. Manteuffel, "MIMO antenna design challenges," LAPC 2009, UK, Nov. 2009, pp. 50-56
- [68] R. Martens, D. Manteuffel, "Element Correlation of MIMO antennas on small terminals", EUCAP 2010, Barcelona, April 2010
- [69] D. M. Pozar, *Microwave engineering*, Wiley, 3rd ed., New York, 2005
- [70] X. Wang, "Kompakte Mehrtorantennen für die adaptive Keulenformung", Doctoral dissertation, May 2004, Bergischen Universität Wuppertal
- [71] H.J Chaloupka, et al "A Superdirective 3- Element Array for Adaptive Beamforming", Microwave and optical Technology Letters, vol. 36, No. 6, March 2003
- [72] P. Yazdanbakhsh, K. Solbach, "Optimization of monopole four-square array antenna using a decoupling network and a neural network to model ground plane effects", EUCAP 2009, Berlin, March 2009
- [73] J.S Neron, G.Y Delisle, "Microstrip EHF Butler Matrix Design and Realization", ETRI Journal, vol: 27, No. 6, December 2005
- [74] P. Yazdanbakhsh, K. Solbach, "A Circuit Model of Monopole Four-Square Array Antenna on a Finite Ground Plane Including Mutual Coupling Effects", EUCAP 2010, Barcelona, April 2010
-

Appendix Computation of Eigenvectors and Eigenvalues

A. Definition of eigenvectors and eigenvalues

An $N \times N$ matrix \mathbf{A} is said to have an eigenvector x and corresponding eigenvalue λ if:

$$\mathbf{A}\mathbf{x} = \lambda\mathbf{x} \quad (\text{A.1})$$

The zero vector is not considered to be an eigenvector at all. On the other hand the equation (A.1) can hold only if:

$$\det|\mathbf{A} - \lambda\mathbf{I}| = 0 \quad (\text{A.2})$$

which if expanded out, is an N^{th} degree polynomial in λ whose roots are the eigenvalues. This proves that there are always N (not necessarily distinct) eigenvalues. Equal eigenvalues coming from multiple roots are called degenerate.

B. Different types of matrices and its associated eigenvalues

Matrix \mathbf{A} is called symmetric if it is equal to its transpose:

$$\mathbf{A} = \mathbf{A}^T \quad (\text{A.3})$$

It is called Hermitian or self-adjoint if it equals the complex-conjugate of its transpose (its Hermitian conjugate denoted by \dagger):

$$\mathbf{A} = \mathbf{A}^\dagger \quad (\text{A.4})$$

It is termed orthogonal if its transpose equals its inverse:

$$\mathbf{A}^T \cdot \mathbf{A} = \mathbf{A} \cdot \mathbf{A}^T = \mathbf{I} \quad (\text{A.5})$$

and is unitary if its Hermitian conjugate equals its inverse.

A matrix is called normal if it commutes with its Hermitian conjugate:

$$\mathbf{A}^\dagger \cdot \mathbf{A} = \mathbf{A} \cdot \mathbf{A}^\dagger \quad (\text{A.6})$$

For real matrices, Hermitian means the same as symmetric and unitary means the same as orthogonal.

The eigenvalues of a Hermitian matrix are all real. In particular, the eigenvalues of a real symmetric matrix are all real.

Contrariwise, the eigenvalues of a real non-symmetric matrix may include real values, but may also include pairs of complex conjugate values. Finally, eigenvalues of a complex matrix that is not Hermitian will in general be complex.

On the other hand, the eigenvectors of a normal matrix with non-degenerate eigenvalues are complete and orthogonal, spanning the N -dimensional vector space. For a normal matrix with degenerate eigenvalues, we have the additional freedom of replacing eigenvectors corresponding to degenerate eigenvalues by linear combinations of themselves.

When a matrix is not normal, in general, we can not find any orthogonal set of eigenvectors, nor even any pairs of eigenvectors that are orthogonal. While the N non-orthogonal eigenvectors will “usually” span the N -dimensional vector space, they do not always do so. That is, the eigenvectors are not always complete. These matrices that do not have eigenvalue decomposition are said to be defective or non-diagonalizable.

For defective matrices “Schur decomposition” can be used instead of eigenvalues decomposition. Using “Schur decomposition” a defective matrix \mathbf{A} can be expressed as:

$$\mathbf{A} = \mathbf{U} \cdot \mathbf{S} \cdot \mathbf{U}^T \quad (\text{A.7})$$

where the columns of \mathbf{U} provide a basis with much better numerical properties than a set of eigenvectors.

C. Generalized eigenvalue problems

From equation (5.1), the eigenvectors and eigenvalues of a body can be obtained by solving the following eigenvalue problem:

$$X(\mathbf{J}_n) = \lambda_n R(\mathbf{J}_n) \quad (\text{A.8})$$

This kind of problem is called generalized eigenvalue problem, and presents the general form

$$\mathbf{A} \cdot \mathbf{x} = \lambda \mathbf{B} \cdot \mathbf{x} \quad (\text{A.9})$$

Often \mathbf{A} and \mathbf{B} are symmetric, and \mathbf{B} is positive definite. In this case, the generalized eigenvalues of \mathbf{A} and \mathbf{B} can be computed using the Cholesky factorization.

Cholesky factorization expresses the symmetric matrix \mathbf{B} as the product of a triangular matrix and its transpose:

$$\mathbf{B} = \mathbf{L} \cdot \mathbf{L}^T \quad (\text{A.10})$$

where \mathbf{L} is an upper triangular matrix.

However, not all symmetric matrices can be factored in this way. The matrices that have a Cholesky factorization are said to be positive definite. This implies that all the diagonal elements of \mathbf{B} are positive and that the off-diagonal elements are not too large.

If \mathbf{B} is non-singular the problem can be solved by reducing it to an equivalent standard eigenvalue problem:

$$(\mathbf{B}^{-1} \cdot \mathbf{A}) \cdot \mathbf{x} = \lambda \mathbf{x} \quad (\text{A.11})$$

If \mathbf{B} is a singular matrix, the generalized eigenvalue problem can not be directly transformed into a standard eigenvalue problem, so an alternative algorithm called *QZ* factorization is necessary. *QZ* factorization is also valid for non-symmetric (non-Hermitian) \mathbf{A} and \mathbf{B} matrices.

In order to solve the generalized eigenvalue problem in (A.8), it can be reduced to its standard eigenvalue problem:

$$(\mathbf{R}^{-1} \cdot \mathbf{X}) \cdot \mathbf{J}_n = \lambda_n \mathbf{J}_n \quad (\text{A.12})$$

This can be done because \mathbf{R} and \mathbf{X} matrices correspond with the real and imaginary parts of the generalized impedance matrix of the antenna \mathbf{Z} .

D. Computation of Characteristic Modes using MATLAB

The eigenvalues and eigenvectors of any antenna can be obtained in quite a straight forward way, by solving (A.8) with Matlab's command *eig*:

$$[J, D] = \text{eig}(X, R) \quad (\text{A.13})$$

where D is the canonical form of $(\mathbf{B}^{-1}\mathbf{A})$, that is, a diagonal matrix with the eigenvalues on the main diagonal, and J is a matrix whose columns are the eigenvectors.

MATLAB uses LAPACK routines to compute eigenvalues and eigenvectors, so it selects the most suitable decomposition algorithm depending on the mathematical properties of matrices R and X .

Note Matlab's command *eig* returns the eigenvectors and eigenvalues, only if R and X are square matrices. If the dimension of these matrices is $M \times M$, MATLAB will return M eigenvectors and M associated eigenvalues.

If it will be possible to find the \mathbf{Z} matrix of a body, then the equation (A.13) can be used to find the eigenvalues of the modes for the body.

In MATLAB it is possible to consider edge cells with RWG (Rao-Wilton-Glisson) vector basis function for a body (e.g. chassis). See Fig A.1

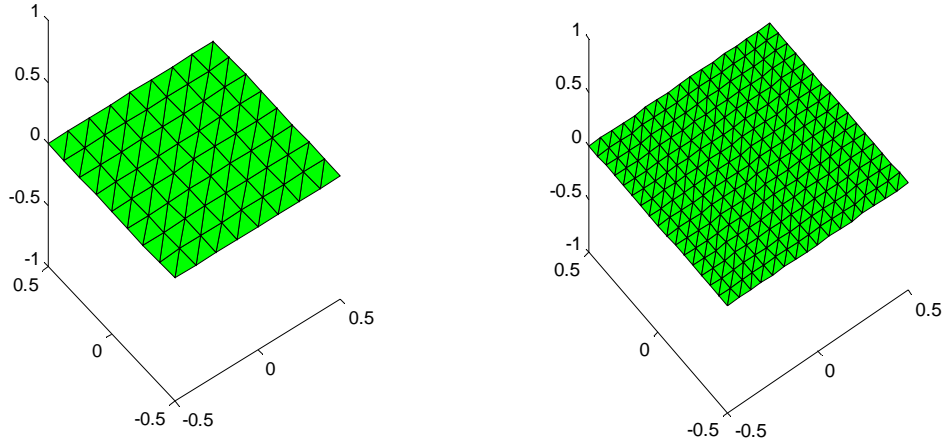


Fig. A.1 Two ground planes with different number of edge elements

The size of the \mathbf{Z} matrix, with components X and R in equation (A.13), for a body is equal to the number of edge elements. If the number of edge elements increases, the number of modes, found by MATLAB also increases.

The edge element can be also shown as below:

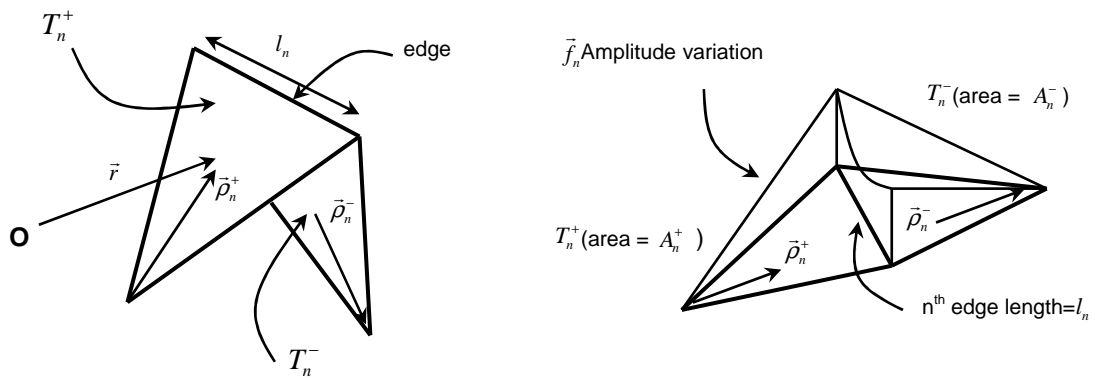


Fig. A.2 Edge element

The RWG vector basis function associated with n^{th} edge is defined as:

$$f_n(\vec{r}) = \begin{cases} (l_n/2A_n^+) \vec{\rho}_n^+, & \vec{r} \text{ in } \vec{T}_n^+ \\ (l_n/2A_n^-) \vec{\rho}_n^-, & \vec{r} \text{ in } \vec{T}_n^- \\ 0, & \text{otherwise} \end{cases} \quad (\text{A.14})$$

The Impedance Matrix can be also defined as:

$$Z_{mn} = l_m [j\omega(A_{mn}^+ \vec{\rho}_m^+ / 2 + A_{mn}^- \vec{\rho}_m^- / 2 + \Phi_{mn}^- - \Phi_{mn}^+)] \quad (\text{A.15})$$

where:

- m and n correspond to two edge elements
- l_m is the edge length of element m
- A is the magnetic vector potential:

$$A_{mn}^{\pm} = \frac{\mu}{4\pi} \left[\frac{l_n}{2A_n^+} \int_{T_n^+} \rho_n^+(r') g_m^{\pm}(r') ds' + \frac{l_n}{2A_n^-} \int_{T_n^-} \rho_n^-(r') g_m^{\pm}(r') ds' \right] \quad (\text{A.16})$$

- Φ is the scalar potential:

$$\Phi_{mn}^{\pm} = -\frac{1}{4\pi j \omega \epsilon} \left[\frac{l_n}{A_n^+} \int_{T_n^+} g_m^{\pm}(r') ds' - \frac{l_n}{A_n^-} \int_{T_n^-} g_m^{\pm}(r') ds' \right] \quad (\text{A.17})$$

where:

$$g_m^{\pm}(r') = \frac{e^{-jk|r-r'|}}{|r-r'|} \quad (\text{A.18})$$

Example1) Consider the 4cm \times 6cm chassis. MATLAB program is used to find the eigenvalues of the chassis modes:

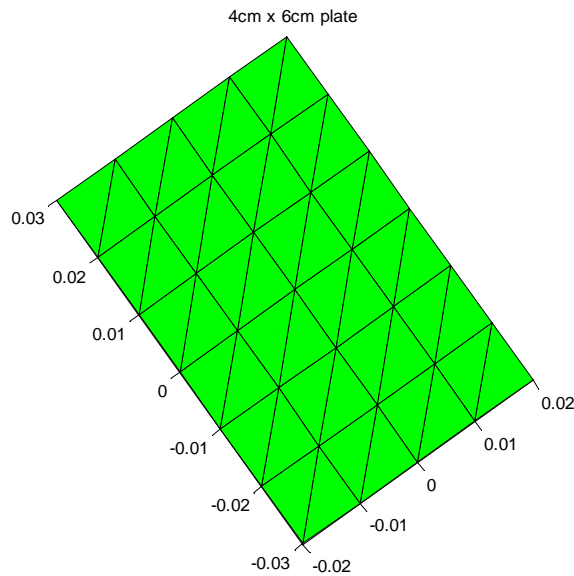


Fig. A.3 4cm \times 6cm chassis with 62 edge elements

- The impedance matrix Z of this chassis with the size of 62×62 is obtained from available an M-file program in MATLAB for each frequency
- Another M-file program in MATLAB has been written to solve the eigenvalues using equation (A.13)

- The eigenvectors $\vec{J}_n = [\vec{J}_1 \quad \vec{J}_2 \quad \dots \quad \vec{J}_{62}]$ have been found

- The eigenvalues $\lambda_n = \begin{bmatrix} \lambda_1 & 0 & \dots & 0 \\ 0 & \lambda_2 & 0 & \vdots \\ \vdots & 0 & \ddots & 0 \\ 0 & 0 & \dots & \lambda_{62} \end{bmatrix}$ are also obtained

- The number of edge elements (The size of impedance matrix) has to be optimized, due to:

Obtain real matrices of \vec{J}_n and λ_n (Complex eigenvalues and eigenvectors can be achieved from ill-conditioned Z matrices)

- Problem: We have 62 modes but which modes have to be selected?
- Selecting the first 6 modes due to their resonances:

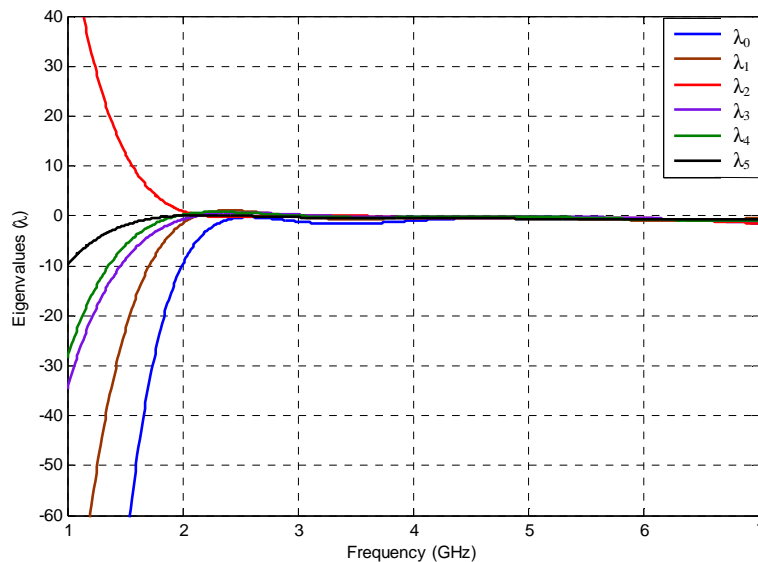


Fig. A.4 Eigenvalues of the first six chassis modes of the $4\text{cm} \times 6\text{cm}$ chassis with 62 edge elements

Example2) Consider the 10cm×10cm chassis. MATLAB program is used to find the eigenvalues of the chassis modes:

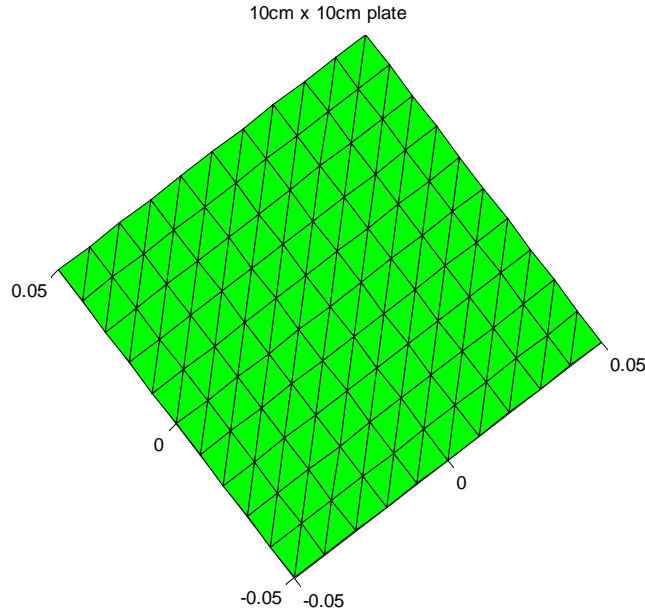


Fig. A.5 10cm × 10cm chassis with 280 edge elements

- If the $[\vec{J}_{28} \ \vec{J}_{52} \ \vec{J}_{91} \ \vec{J}_{114} \ \vec{J}_{174} \ \vec{J}_{206} \ \vec{J}_{232} \ \vec{J}_{261}]_{280 \times 8}$ modes are selected and the corresponding $\lambda = [\lambda_0 \ \lambda_1 \ \lambda_2 \ \lambda_3 \ \lambda_4 \ \lambda_5 \ \lambda_6 \ \lambda_7]$ are calculated for each frequency, then the following results can be obtained:

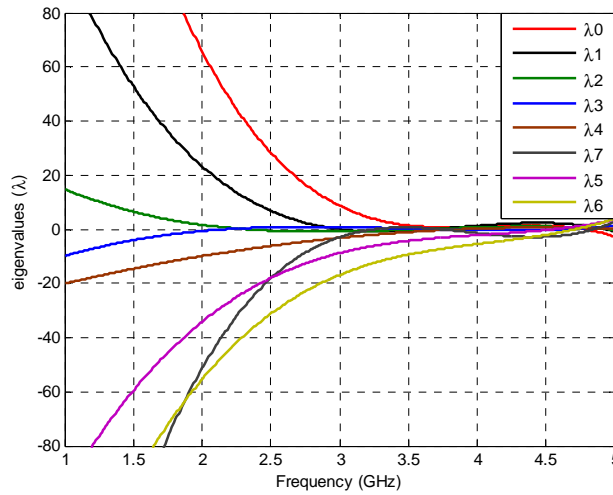


Fig. A.6 Eigenvalues of the first eight chassis modes of the 10cm × 10cm chassis with 280 elements

The information presented in this appendix (a) to (c) has been extracted from reference [59] and appendix (d) is based on own MATLAB codes.

